THE EFFECT OF PLASTIC DEFORMATION ON A SERIES OF THIN MAGNETIC FILMS

THESIS

Presented to the Graduate Council of
Texas State University-San Marcos
in Partial Fulfillment
of the Requirements

for the Degree

Master of SCIENCE

by

Amanda F. Gregory, B.S.

San Marcos, Texas
December 2010

THE EFFECTS OF PLASTIC DEFORMATION ON A SERIES OF

THIN MAGNETIC FILMS

Committee Members Approved:

_____

Dr. Ir. Geerts, Chair

_____

Dr. David Donnelly

_____

Dr. Jitendra Tate

_____

Dr. Martin Sablik

Approved:

_____

J. Michael Willoughby
Dean of the Graduate College

FAIR USE AND AUTHOR'S PERMISSION STATEMENT

Fair Use

Duplication Permission

For dad - I know you're proud of me.

ACKNOWLEDGEMENTS

I'd like to extend a very special thank you to all the professors and classmates I have had the pleasure of being inspired by over the course of my academic career – I cannot thank all of you enough for being such an enormous source of support. Specifically, I would like to thank the following people:

Dr. Ir. Wilhemus J. Geerts: *Who offered me so many incredible research opportunities.*

Dr. Martin Sablik: *Who always had faith in my abilities, whether I deserved it or not.*

Dr. Anup Bandyopadhyay: *Who patiently assisted me with all equipment related issues.*

This manuscript was submitted on October 27, 2010.

TABLE OF CONTENTS

Page

PART II. SAMPLE CHARACTERIZATION

PART III: RESULTS AND CONCLUSIONS

LIST OF TABLES

Table **Page**

LIST OF FIGURES

Figure **Page**

ABSTRACT

THE EFFECTS OF PLASTIC DEFORMATION ON A SERIES OF THIN MAGNETIC FILMS

by

Amanda F. Gregory, B.S.

Texas State University-San Marcos

December 2010

SUPERVISING PROFESSOR: WILHELMUS J. GEERTS

Thin magnetic films of FeSi and NiFe were grown on super-elastic Nitinol using dual ion beam and magnetron sputtering techniques, then submitted to varying degrees of lateral strain to induce plastic deformation in the thin magnetic film by (1) bending over a cylinder of fixed radius and (2) straining the sample laterally using an Instron 5566 materials tester. The magnetic properties were measured after each straining session via VSM using a sample holder developed for these experiments, which would allow the characterization. The quantity of plastic deformation introduced into the film was documented via optical microscopy. After films had been submitted to a maximal

amount of strain, the overall adhesion of the film was tested using a Scotch tape approach.

No effect of plastic deformation was observed by optical microscopy for the samples deformed by bending over a cylindrical object, and none of the thin films would detach from the Nitinol substrates when up to 4% strain was applied using this technique. The plastic deformation in the samples stretched by the Instron 5566 materials tester appeared to be inhomogeneous.

Two types of plastic deformation were observed by optical microscopy on the samples stretched in the Instron. In the magnetron sputtered samples, cracks were introduced perpendicular to the strain direction at strains above 1 %, resulting in some of the thin film detaching from the Nitinol substrate. The DIBS FeSi-0.5% samples did not detach from the substrates upon straining up to 5%. After the larger strain cycles, small blisters over less than 1% of the film were observed by optical microscopy. The VSM measurements revealed at strains above 1% the magnetic properties of each sample changed permanently, indicating magneto-plastic effects. The magnetic hysteresis curves measured on the DIBS samples suggests that the magneto-plastic deformation is not homogeneous in those films, and that the areas of the thin film exposed to large strains have very different magnetic properties from the original, unstrained films.

Although several possible effects have been identified to explain the observed magneto-plastic properties, no conclusive theory has yet been developed to explain the observed magneto-plastic properties. Portions of the content related in this thesis was presented or published at the Fall meetings of the TSAPS, [1, 2, 3] at the 2007 Texas State honor's conference, [4] at the 2008-MMM conference, [5] and in IEEE Trans. on Magn. [6]

CHAPTER I: INTRODUCTION

Thin magnetic films are an important component in many different types of devices. Such films are likely to undergo both elastic and plastic deformation during the manufacturing process and over the lifetime of their use. In order to understand failure modes and lifetime issues of these magnetic thin film devices, it is vital to know how the magnetic properties of the films behave after being somehow deformed.

Although a lot of research has been performed regarding the magneto-elastic properties of thin films, [7, 8] the magneto-plastic properties of thin films have hardly been investigated, in large part because of the difficulties in producing and controlling plastic deformation in the films.[9] Itoh investigated the domain pattern around point and line defects in 1μm thick permalloy films on copper wires [10] and 1 μm thick permalloy wires, [11] and he found that domain walls would pin on these structures. Lupulescu et al. [12] studied the effect of magneto-plastic deformation on magnetic anisotropy for 100 nm thick nickel samples deposited on 1 mm thick copper wires. More recently Shinoura et al investigated the stress distribution in the core of a magnetic thin film head and concluded that it originates from plastic or creep deformation. [13]

In this thesis the magneto-plastic properties of thin ferromagnetic films on super-elastic Nitinol sheet metal are studied. To the knowledge of the experimenters, this is the first report on the magnetic properties of thin films sputtered on Nitinol sheet metal. The

objective of this study was to develop a general procedure for determining the magneto-plastic properties of thin ferromagnetic samples.

PART I:

SAMPLE CREATION

CHAPTER II: SAMPLE SUBSTRATES

Careful substrate preparation is vital to achieving reliable and useable results. This chapter will describe the substrate material chosen for this series of experiments in detail, including its dimensions, the methods by which substrates were prepared for deposition, and their placement in each sputtering system.

Substrate Material

Nitinol sheet metal is an intermetallic compound composed of nickel and titanium whose peculiar elastic and shape-memory properties were discovered by the Naval Ordnance Laboratory in 1962. Intermetallic compounds are known to exhibit solid state phase transformations in which the crystal structure of the material changes geometric shape under certain conditions. These different phases are referred to as "Martensite" (low-temperature or high stress) and "Austenite" (high-temperature or low stress).[14]

Nitinol is generally composed of roughly equal portions of nickel and titanium, ranging anywhere from approximately 55 to 56 weight percent (which is 50 to 51 atomic percent) of nickel. The ratio of nickel to titanium in the alloy determines the temperature at which the material undergoes its Austenite-Martensite and Martensite-Austenite phase changes.[14] Nitinol was chosen as a substrate material primarily for its super-elastic properties at room temperature.

At low temperatures Nitinol is in a complex, monoclinic Martensitic phase. In this phase the material is easily deformed via an elastic deformation process known as twinning, during which the atomic planes rearrange themselves without causing any permanent deformation. When Martensitic Nitinol is deformed, it holds the shape it has been deformed to, and can be subjected to a larger amount of stress before failure or plastic deformation than most other metals and alloys.[14, 15]

Above a certain temperature however, Nitinol transforms into an inter-penetrating simple cubic Austenitic phase. This phase exists only in a certain temperature range, though the actual temperature at which transformation from Martensite to Austenite occurs is determined by the relative amounts of nickel and titanium in the material. When sufficient stress is applied, Austenite transforms into Martensite. This stress-induced Martensitic phase is unstable above the transition temperature, and as the applied stress is removed it reverts back to the Austenitic phase, leaving little or no permanent deformation in the material.[15] As these experiments were performed at room temperature with super-elastic Nitinol sheet metal, the transition temperature for the substrates must be well below room temperature.

The (stress-induced) transformation of Nitinol from Austenite to Martensite takes place via the nucleation of transformation sites in areas of sufficiently large stress. As Austenitic Nitinol is strained, areas of high stress (such as the locations where the material is clamped for testing) begin to transform to Martensite, and result in an inhomogeneous strain in the material.[15] This effect has been observed in wires as well as in sheet metal Nitinol, and because of this the elasticity in Nitinol is often referred to as pseudo-elasticity. From careful observation of the straining process, it appears that the

strain-rate is directly proportional to the number of transformation sites, as well as the rate at which these domains of stress-induced Martensite propagate through the material. When the strain-rate is high the number of transformation sites increases, crisscrossing each other and appearing to widen as the net strain continues to increase. Slower strain-rates result in a vastly decreased number of transformation sites in the material. In cases of very slow strain-rates (such as those used in these experiments), only one or two transformation areas or fronts are formed. In much of this research, these sites of stress-induced Martensite are referred to as "transformation fronts," because they appear to maintain their shape and orientation as they move through the material.

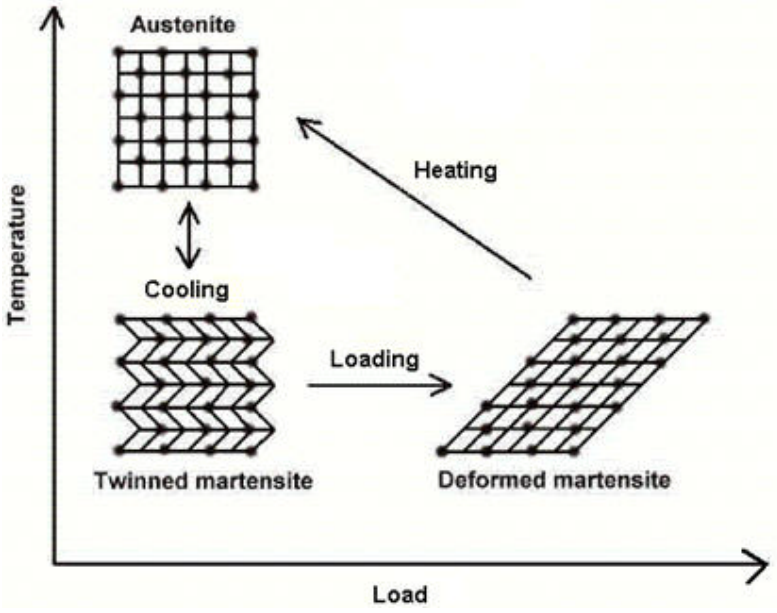

Figure 2.1: Nitinol Phases – Temperature Vs. Load

http://nonferrous.keytometals.com/images/Articles/Fig207_3.jpg

Cleaning the Substrates

Prior to film deposition all of the substrate materials were thoroughly cleaned using ultrasonic methods. Careful preparation of the samples is important in order to ensure the samples will not be sources of contamination within the vacuum system, which would make the ultimate pressure of the system more difficult to reach and negatively affect the composition of the deposited films.

Each of the sample substrates was cleaned ultrasonically for 5 minutes in an acetone bath, then removed and rinsed with isopropyl alcohol. After the alcohol rinsing, the substrate material was submerged in an isopropyl alcohol bath and ultrasonically cleaned for an additional 5 minutes. Upon removal of the substrate material from the isopropyl alcohol, compressed pure nitrogen gas was used to dry each substrate. Samples were stored in individual cases lined with Kimberly-Clark brand low lint Kimwipes to keep them as clean as possible between cleaning and film deposition.

CHAPTER III: VACUUM SYSTEMS

The purpose of this section is to describe the conditions and methods by which high vacuum was reached in order to make deposition of a thin metallic film on the substrates possible. In a vacuum system, the substrates are isolated from the surrounding environment as stray particles are pulled from the chamber using a series of different pumps. At higher vacuum (or lower pressure), there are fewer stray particles in the area surrounding the substrate, and with fewer stray particles available to contaminate the film, the desired atoms and molecules can be placed on the substrate surfaces. The following chapter describes how excess molecules are evacuated from the vacuum chamber, and focuses primarily upon the different types of vacuum pumps that are used and how they function in different pressure ranges.[16]

Roughing the Chamber

At atmospheric pressure, the vacuum chamber is crowded with a sea of single atoms and molecules, all of which are constantly in motion and colliding. At this pressure, the atoms are crowded together and the average distance any particular molecule might travel before colliding with another (its "mean free path") is very short - on the order of several micrometers. Collisions between atoms are so frequent that this particle-particle interaction is the dominant factor that determines their speed and trajectory. In other words, in this high pressure state the molecule-molecule collisions

are the main factor contributing to the motional behavior of the particles within the chamber. The motion of the molecules in this state is predictable, much like macroscopic fluid flow, and is commonly referred to as "viscous flow."

When evacuation of the vacuum chamber begins it is teeming with atoms, and in order to remove this sea of unwanted particles from the environment immediately surrounding the substrates, these excess particles must be swept away using a pump capable of functioning under molecular flow conditions. This process is referred to as "roughing" the chamber, as a roughing pump will remove *roughly* 99.999% of the atoms from the vacuum chamber, bringing it into the 10^{-3} torr pressure range. Mechanical roughing pumps remove excess particles from the chamber by compressing them and then venting them out of the vacuum system. Although there are several different types of mechanical pumps that can be used to rough the vacuum chamber, a rotary vane oil-sealed mechanical pump was used with the DIBS system.

The rotary vane oil-sealed mechanical pump utilizes the predictable viscous flow behavior of the molecules within to sweep them from the crowded chamber and is illustrated in Figure 3.1. Rotary vane pumps are robust, reliable, and relatively inexpensive, which makes them an ideal pump for projects such as this. As implied by the name, the vacuum seal of such a pump is formed by oil. While this oil seal works well at high pressures when the atoms in the chamber are undergoing viscous flow, at lower pressures the oil that forms the seal in such a pump will begin to flow back into the chamber and contaminate the vacuum system. In order to reduce the amount of back-streamed oil that gets into the chamber, an oil filter/condenser may be placed between the pump and the vacuum chamber. As the pressure in the chamber drops however, the

amount of oil back-streaming into the system will increase, and for this reason a rotary vane oil-sealed mechanical pump should only be used in circumstances where the pressure is relatively high. Because of oil back-streaming at low pressures, a mechanical pump alone cannot bring the vacuum chamber to a low enough pressure to perform satisfactory vapor deposition without the assistance of another, high-vacuum pump.

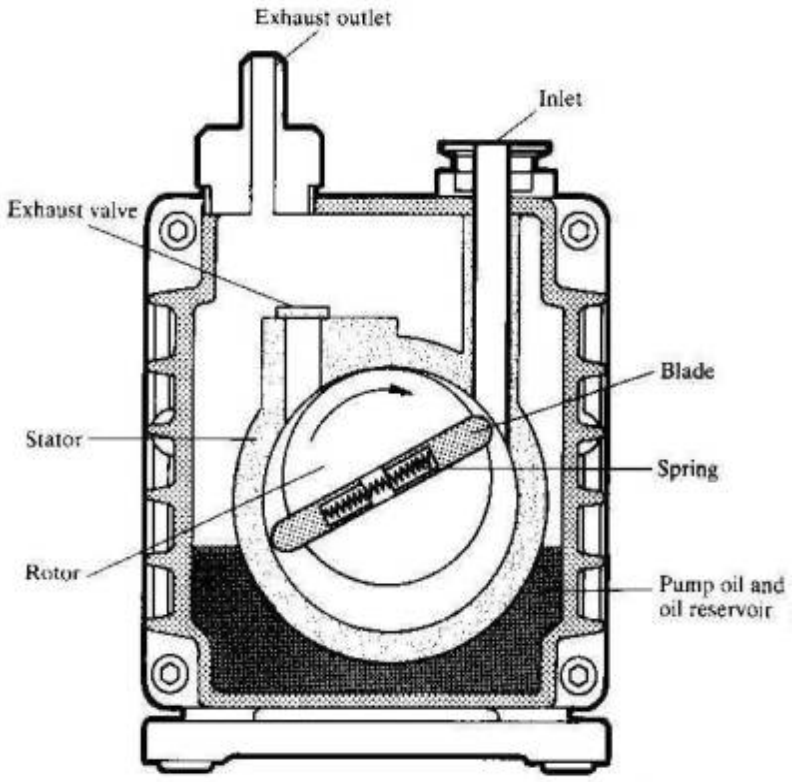

Figure 3.1: Rotary Vane Oil-Sealed Mechanical Pump

Image from: http://www.etafilm.com.tw/images/Rotarypump.jpg

Reaching High Vacuum

In order to reach lower pressure (or higher vacuum), mechanical pumps are normally used in combination with high vacuum pumps.[16] A mechanical pump is

normally attached to the outlet of a high vacuum pump so that it can compress the gas ejected by the high vacuum pump and then expel it from the system completely. When a mechanical pump is set up to pump on the outlet of a high vacuum pump, it is referred to as a “backing pump,” since it *backs up* the pumping of a high vacuum pump. When a mechanical pump is used in this manner, much lower pressures may be reached in the system and the amount of oil that could potentially back-stream into the system is minimized. Although a vacuum system utilizing a mechanical pump alone can reach pressures as low as a few millitorr, when a mechanical pump is used in conjunction with a high vacuum pump the system can reach much lower pressures.

The pressure in the system drops because there are fewer and fewer molecules populating it. As the mechanical pump evacuates the system, the number of free molecules drops dramatically until there is almost no molecule-molecule interaction. When there are so few molecules in the vacuum chamber, their mean free path is much longer (on the order of meters), which means they are much more likely to collide with the walls of the chamber - or the blades of a pump - than with each other. At this pressure the gas inside the vacuum chamber is undergoing what is called "molecular flow," since molecule-molecule interactions no longer dominate the motional behavior of the molecules inside the chamber.

There are a number of different types of high vacuum pumps that can be used to reach low pressures in a vacuum system. In the DIBS system a turbomolecular pump and a cryopump were used to reach high vacuum. The way that high vacuum pumps function is quite different from the way a mechanical pump functions, because they are designed to operate under molecular flow conditions. Because the mean free path of molecules

within the chamber is very long at low pressure - much greater than the dimensions of the vacuum chamber – high vacuum pumps have larger openings so that they can pump more efficiently in the molecular flow regime.

When a moving surface comes into contact with a molecule that is in motion, it changes the momentum of the molecule slightly. A turbomolecular pump is made of a series of angled blades - some that spin (rotors), and some that are stationary (stators) - which collectively direct the molecules from the chamber into the pump. The rotors of a turbomolecular pump spin extremely fast - on the order of 9 to 90 thousand revolutions per minute. Each rotor blade imparts a portion of its momentum to the molecules it comes into contact with, which speeds them up and changes their direction, driving them deeper into the pump where they accumulate until they are at a high enough pressure to be pumped away by the mechanical backing pump. [16]

Turbomolecular pumps are fairly robust. They can be operated at pressures as high as 10^{-2} torr, and may reach an ultimate pressure of below 5×10^{-10} torr. However, if a turbomolecular pump is operated under viscous flow conditions it may be badly damaged. Recall that, under viscous flow conditions, the molecules inside the vacuum chamber are crowded together and constantly colliding. Under these conditions, the push of molecules on the blades of the rotors of a turbo pump can cause them to bend, potentially far enough to come into contact with the stators inside the pump. Because the rotors of a turbomolecular pump spin so rapidly an accidental collision with the stationary stators would warp the blades of the rotor, and the sudden change in the speed of the stator would cause the bearings within the pump to knock together and chip, or "dimple." Bearings may also be damaged when a turbomolecular pumps is improperly

shut down, such as a shutdown caused by a power failure. Dimpled bearings will cause the turbomolecular pump to function less smoothly, and the slight variation in the turning of the rotors will ultimately reduce the efficiency at which the pump is able to evacuate molecules from the vacuum chamber. [16]

Figure 3.2: Turbomolecular Pump

http://en.wikipedia.org/wiki/File:Cut_through_turbomolecular_pump.jpg

A cryosorption pump works differently than a turbomolecular pump, as it cools the gas remaining in the vacuum chamber until it freezes or can be stored inside the body of the pump. Cryosorption pumps can work down to pressures on the order of 10^{-9} torr and lower. Although a cryosorption pump may be used at atmospheric pressure, it is

inefficient in this range as it is trying to cool and condense numerous, highly energetic atoms. A cryosorption pump is made up of two main parts: the main pump and a gaseous helium compressor. In the compressor, gaseous helium is compressed and cooled before moving into the main pump's second stage or "cold head." Within the main pump are the first and second stage cryoarrays, which make up the cold head, and are the surfaces that are cooled by the expansion of the helium gas. The expansion of the helium cools the cryoarrays, bringing the temperature of the first and second stages to approximately 70 K and 12 K respectively. [16]

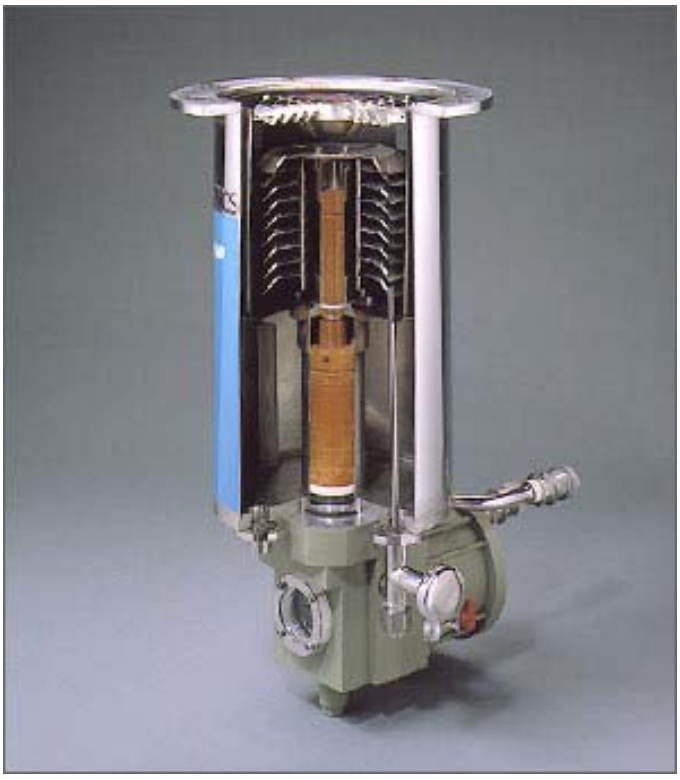

Figure 3.3: Cryosorption Pump

http://medivactech.com/images/cryotorr_6.jpg

A cryopump draws atoms from the chamber in two different ways. The first and second stage cryoarrays are extremely cold, so cold that *most* gases will condense to solids at this low temperature in a process called "cryocondensation." Certain light gases such as hydrogen and helium will not condense even at this temperature, so in order to extract these atoms from the chamber a porous material (usually activated charcoal) is attached to the second stage (coldest) cryoarray. Atoms that are not condensed via cryocondensation become trapped in the maze-like surface of the cold, porous material. In this process called "cryosorption," atoms slowly lose energy as they bounce around in the porous material until they have lost enough energy to condense on the inner surface of the material. [16]

Vacuum System Troubles

A high-vacuum state is difficult to maintain, as the familiar adage "nature abhors a vacuum" suggests. The world around us is filled with vibrating atoms and molecules, which are all moving around and colliding with each other. These free atoms and molecules naturally strive to fill all the space available to them, making it especially difficult to keep them out of a given volume. To keep atoms out of the vacuum chamber once they have been extracted, the vacuum chamber must be tightly sealed to keep it isolated from the outside environment. Any type of leak can negatively impact the quality of the vacuum, but a "virtual leak" is common and difficult to locate – but fairly easy to prevent.

Virtual leaks can stem from trapped pockets of air or contaminants inside the vacuum chamber. When a contaminant is present inside the vacuum chamber – for

example, the oil and dirt from a fingerprint – it expands tremendously under low pressure in a process called sublimation. In other words, the atoms and molecules that make up the contaminant expand and spread out to bounce around inside the chamber, which increases the pressure of the system. Virtual leaks that stem from contamination within the chamber can be avoided by placing only clean items into the system and by wearing gloves to avoid accidentally leaving contaminants inside the system. [16]

The second type of virtual leak results from a pocket of trapped gas somewhere inside the system that has a very narrow path of escape. Any opening in the vacuum system large enough for an atom or molecule to squeeze through (for instance, the space between the threads of a screw) can trap residual gas molecules, and can thus be a source of increasing pressure inside the system. Although there may be a relatively small amount of gas trapped in the pocket, because the path the gas molecules must travel to be removed from the system is very narrow, it is often very difficult, time consuming, or even impossible to fully draw these particles from the system. [16]

Depending on the quality of vacuum necessary to perform an experiment, a virtual leak may or may not be a concern. However, because of the nature of virtual leaks, they are constant sources of increasing pressure inside the system, and for experiments that require ultra-high vacuum conditions a virtual leak could prevent the system from reaching or maintaining a sufficiently high vacuum. There is little that can be done about gas trapped in tiny pockets within the system, short of meticulously designing the system to minimize these spaces.

Vacuum Gauges

Determining the pressure inside the vacuum chamber requires numerous different gauges that are designed to function in different pressure ranges. The following section will describe how the different gauges in our system determine the pressure in the vacuum chamber, as well as their respective pressure ranges. Tables 3.1 a and b summarize the gauges used in the DIBS and the magnetron sputtering systems respectively, and includes their useable pressure ranges. The location of the valves, pumps, and gauges for the DIBS system are shown in Figure 3.10.

Table 3.1: Vacuum Gauges Used in DIBS and Magnetron

DIBS	
Gauge Name	**Approximate Pressure Range (atm)**
Bourdon	10^{-1} - 10^{4}
Thermocouple	10^{-3} – 1
Capacitance Manometer	10^{-5} – 10^{4}
Ionization	10^{-10}-10^{-1}

(a.)

Magnetron	
Gauge Name	**Approximate Pressure Range (atm)**
Convection	10^{-4} – 1
Crystal Oscillator	10^{-9} – 760
Ionization	10^{-10}-10^{-1}

(b.)

The Bourdon gauge is a rugged gauge that measures pressures at or near atmosphere. This gauge measures the relative pressure between the chamber and the outside environment. Figure 3.4 shows a cross-section of the bourdon gauge. A thin tube

is curved into an arc, with one end attached to a reading needle and the other connected to the chamber. As pressure in the chamber drops, the curved tube responds by changing its shape and moving the needle, much like sucking on a plastic straw with the other end covered will cause the straw to collapse. Since it measures the relative difference between the pressure inside and outside the chamber, the Bourdon gauge lacks a great amount of accuracy, because the pressure outside the chamber is constantly changing. The DIBS system uses a Bourdon Gauge for measuring the pressure while roughing the chamber.

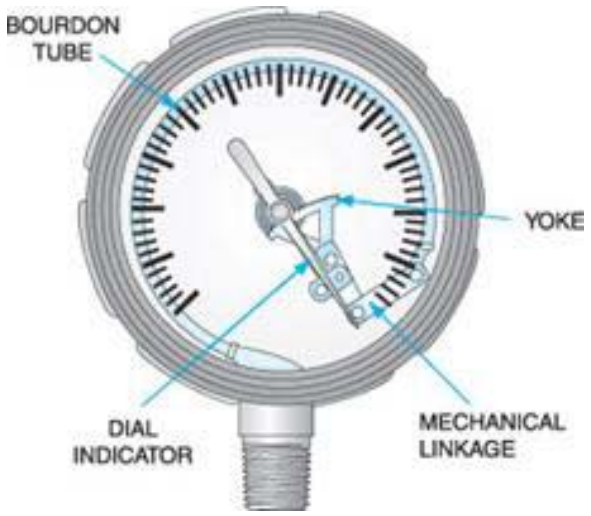

Figure 3.4: Bourdon Gauge

http://www.lesker.com/newweb/Gauges/gauges_technicalnotes_1.cfm

The thermocouple gauge measures the amount of heat conducted away from a hot filament by the gas in the chamber. It is much more accurate than the Bourdon gauge, because it does not measure a relative pressure that is dependent on the fluctuating pressure outside the vacuum chamber, and is instead exposed only to the environment inside the vacuum system. At high pressures, when there are a large number of atoms and molecules present, the heat of the filament is conducted away by the atoms that collide with it, causing the filament to have a lower temperature. At lower pressures there are fewer atoms and molecules that collide with the filament, and without these collisions to conduct heat away from it, the filament has a higher temperature. In pressure ranges around 1 millitorr, the heat loss of the filament happens primarily through radiation, which is constant at this pressure and causes the thermocouple gauge to read zero. Additionally, the thermocouple gauge has a fairly slow response time, as the filament must heat up and then measure how rapidly heat is conducted away from it. There are two thermocouple gauges in use with the DIBS system.

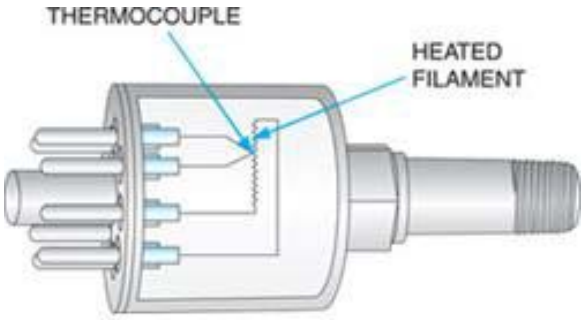

Figure 3.5: Thermocouple Gauge

http://www.lesker.com/newweb/Gauges/gauges_technicalnotes_1.cfm

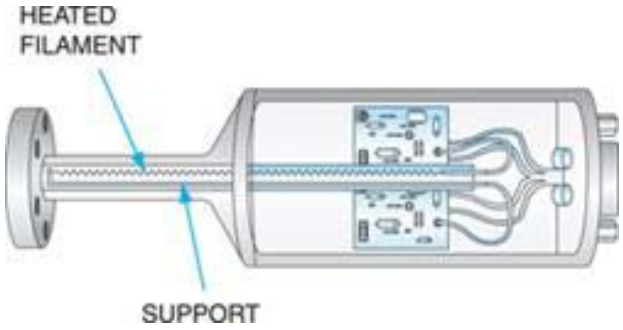

Figure 3.6: Pirani Gauge

http://www.lesker.com/newweb/Gauges/gauges_technicalnotes_1.cfm

The convection gauge is an enhanced form of a simpler gauge called the Pirani gauge, which is in turn similar to the thermocouple gauge. Like the thermocouple gauge, the convection gauge measures how the temperature change in a hot filament varies with the pressure inside the system. Unlike the thermocouple gauge, however, the convection gauge measures how the resistance in the hot filament changes as the temperature changes. The higher the filament's temperature, the greater its resistance, and a change in resistance creates a voltage difference within a balanced circuit. The imbalance between the resistance through the heated filament and a compensator with a constant temperature and pressure (and therefore a constant resistance) creates a voltage difference in the circuit, which causes a current to flow and change the reading on the gauge's meter. The convection gauge has a faster response time than the thermocouple, but is often more expensive because of its complexity. A convection gauge is used on the main chamber in the magnetron sputtering system.

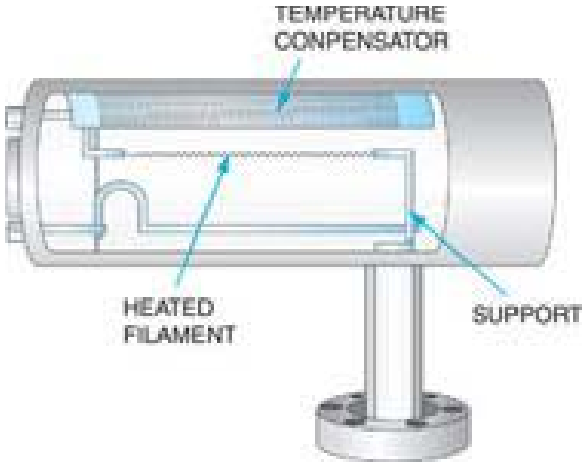

Figure 3.7: Convection Gauge

http://www.lesker.com/newweb/Gauges/gauges_technicalnotes_1.cfm

A capacitance manometer is a gauge somewhat similar to the Bourdon gauge, in that it measures the relative pressure between the inside and the outside of the vacuum chamber. However, instead of using the pressure difference inside and outside the vacuum chamber to physically move a needle as the Bourdon gauge does, a capacitance manometer uses the relative pressure difference to deflect a flexible metal diaphragm. A cross section of this gauge is depicted in Figure 3.8. One side of the diaphragm is exposed to the pressure inside the chamber, and the other side is sealed and contains an electrode assembly. When the pressure inside the chamber changes, the diaphragm is deflected and there is a change in capacitance between the electrodes and the diaphragm. This change in capacitance is converted into a pressure reading. The benefits of this gauge are its fast response time and its accuracy. A Baratron capacitance manometer is used with the DIBS system.

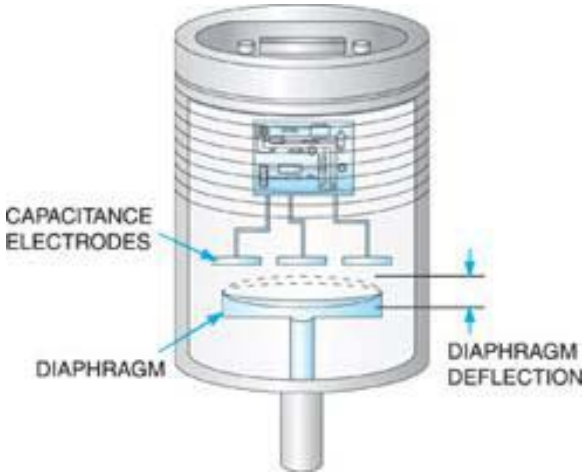

Figure 3.8: Capacitance Manometer

http://www.lesker.com/newweb/Gauges/gauges_technicalnotes_1.cfm

A Televac crystal oscillator gauge is used on the load lock chamber of the magnetron sputtering system. In this type of gauge, a crystal oscillates at a specific frequency. The friction between gas molecules and the surface of the quartz crystal cause a resistance to the oscillation of the crystal, which in turn determines the electrical impedance present. As the pressure changes, so does the oscillation frequency in the crystal, which is then converted into a pressure value. [17]

Ionization gauges are used in a number of different high vacuum and ultra-high vacuum systems, because they are capable of measuring very low pressure ranges. This gauge operates by charging molecules and then "counting" the free electrons they absorb to become neutral again. The ionization gauge consists of a hot filament, a positively charged grid, and a positively charged collector. The hot filament emits electrons which are attracted to the positively charged, loosely-wound grid. However, because of the grid

is so loosely-wound, these electrons pass by it many times, which allows them to come into contact with and ionize gas molecules. These positively charged gas molecules are attracted to the negatively charged collector, which creates a positive ion current. The pressure reading of the gauge is derived from the sensitivity of the gauge and the ratio of the positive ion current to the negative electron emission current. Ionization gauges were used to measure the pressure in main chamber of both the DIBS and the magnetron sputtering systems.

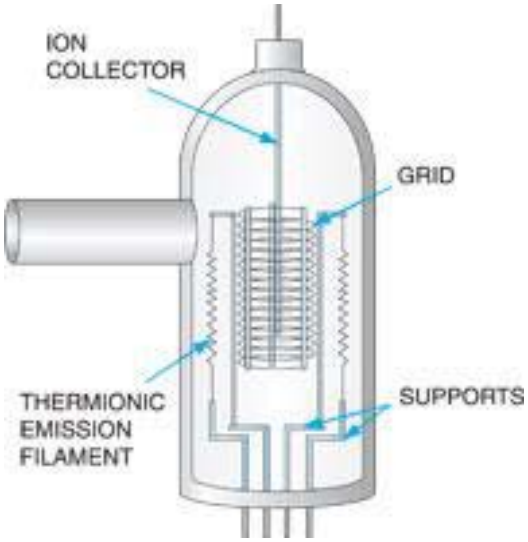

Figure 3.9: Ion Gauge – Hot Filament

http://www.lesker.com/newweb/Gauges/gauges_technicalnotes_1.cfm

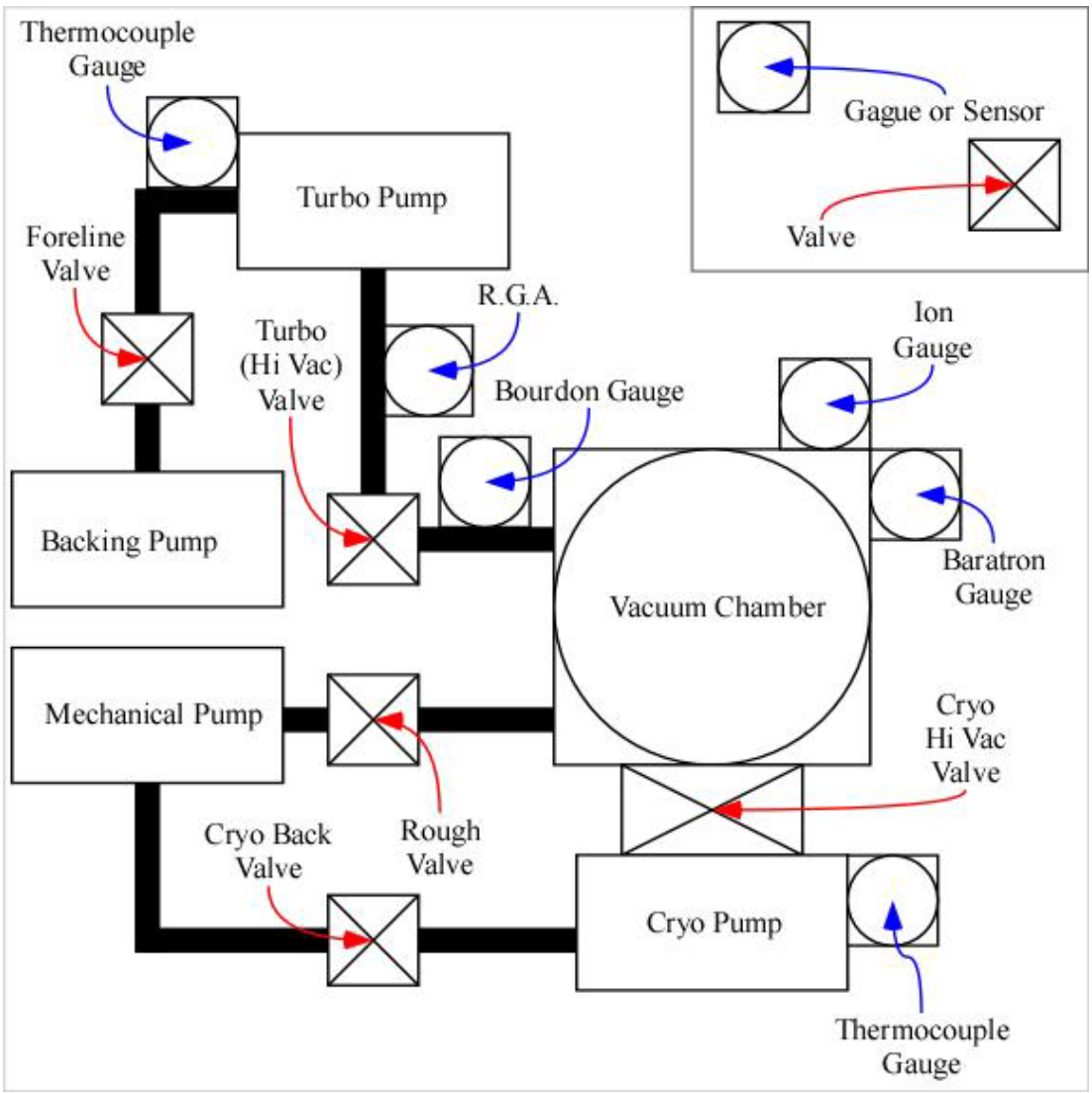

Figure 3.10: The DIBS System

CHAPTER IV: DEPOSITION METHOD

The following section will detail the methods by which thin films were deposited upon the substrate materials. Two different methods were used for deposition: Dual Ion Beam Sputtering (or DIBS), and Magnetron sputtering.

Placement in the Chamber

Since two different deposition methods were employed for film growth, the way the substrate materials were secured to the substrate holder in each system was slightly different. The sample holders for both pieces of deposition equipment are flat, circular disks with clips attached to their edges by hex bolts. In both systems the Nitinol sheet metal was the first material placed on the substrate holder platform, with the glass and silicon disks placed on top of it. Because silicon and glass (especially at this thickness!) are quite brittle, tightening the substrate clips was done with extreme care so that the pressure would not cause the glass or silicon to crack or break during deposition. Although the substrate clips cover a small area of the glass and silicon disks during deposition, this covered area is small enough (approximately 9% of the total surface area), that it can be ignored.

The sample holder in the DIBS system uses four short clips to secure the substrates to it, two of which were repositioned so the minimal angular separation between them was roughly 45° and the maximum angular separation was approximately 135° (see Figure 4.1a, not to scale). This allowed the substrate materials to be fastened

securely to the holder so that the empty space between them was minimized. The silicon and glass samples were placed directly on the surface of the Nitinol substrate, where they acted as a mask and caused the film deposited on the Nitinol substrate to have a curved shape at its edges as shown in Figure 4.1b. The glass and silicon substrates were clipped so that they remained flush with the surface of the Nitinol, which was in turn flush with the surface of the sample holder.

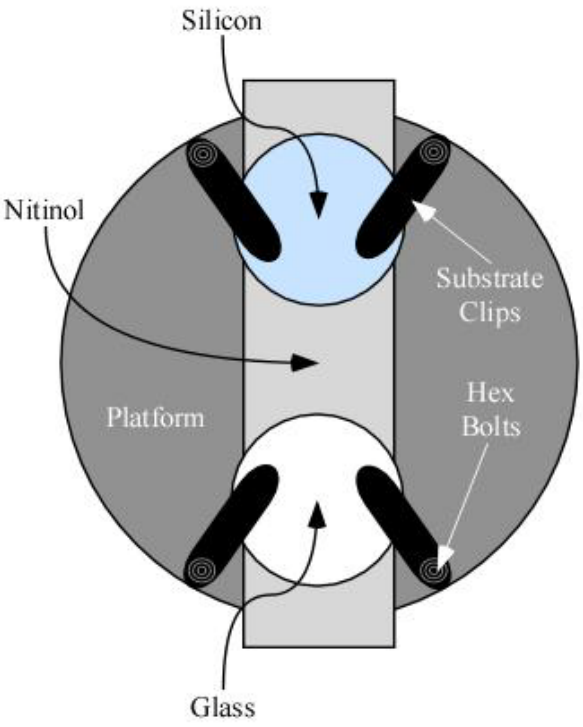

Figure 4.1a: DIBS Sample Orientation

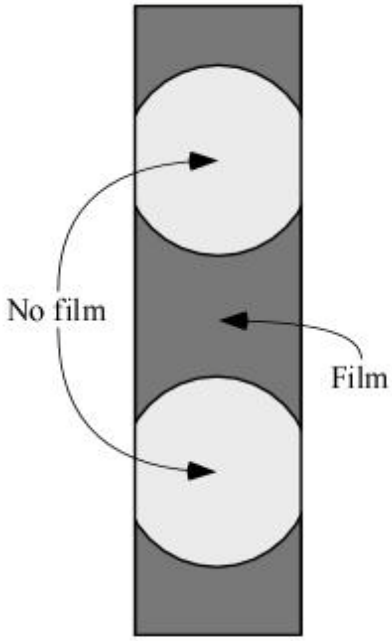

Figure 4.1b: Expected Film Cover on Nitinol Substrate - DIBS

The sample holder in the magnetron sputtering apparatus is slightly different from the one in the DIBS, in that it has only two substrate clips. For deposition in this equipment, a glass microscope slide was cut in half and placed on the surface of the Nitinol substrate to serve as a mask, and the glass and silicon samples were positioned on

top of the microscope slide pieces. Creating a rectangular-shaped film on the Nitinol substrate serves multiple purposes. First, it allows a simplified calculation of the surface area of the film, which is necessary to to determine film thickness (as mentioned in Appendix A). Next a rectangular film ensures that all of the magnetic sample material is located in the most sensitive position within the VSM apparatus (for more on this, see "Thickness Variation" in the following chapter). Finally, this clearly defined rectangular film allows optical microscope photographs of the same areas to be taken without ambiguity.

When substrate materials were placed on the magnetron's holder, the clips caused the samples to tilt slightly, instead of remaining flush against each other and the sample holder. This slight tilt introduced a small amount of space between the substrate materials. Although the glass and silicon substrates were flush with the microscope slide mask, the microscope slide mask was not flush with the Nitinol substrate. Every effort was made to get the mask flush with the substrate, but there is some chance that film material extended past the intended film border. Figure 4.2 shows how the mask failed to remain completely flush with the Nitinol substrate and Figure 4.3 illustrates how the substrate materials were placed on the sample holder for magnetron sputtering.

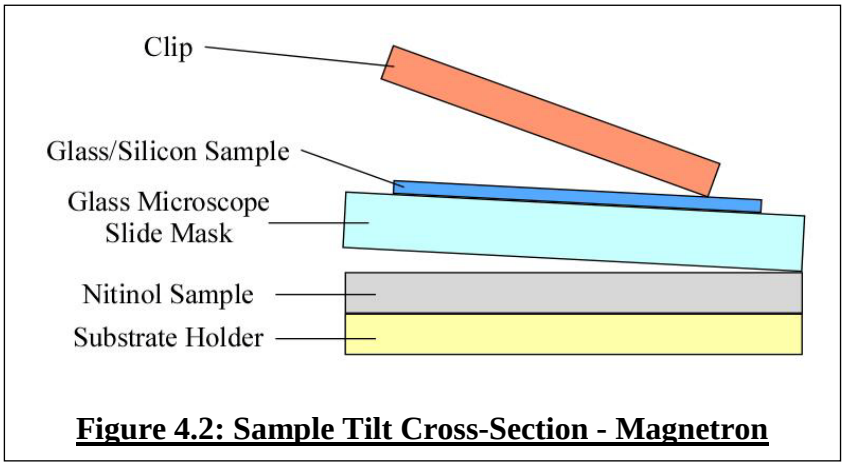

Figure 4.2: Sample Tilt Cross-Section - Magnetron

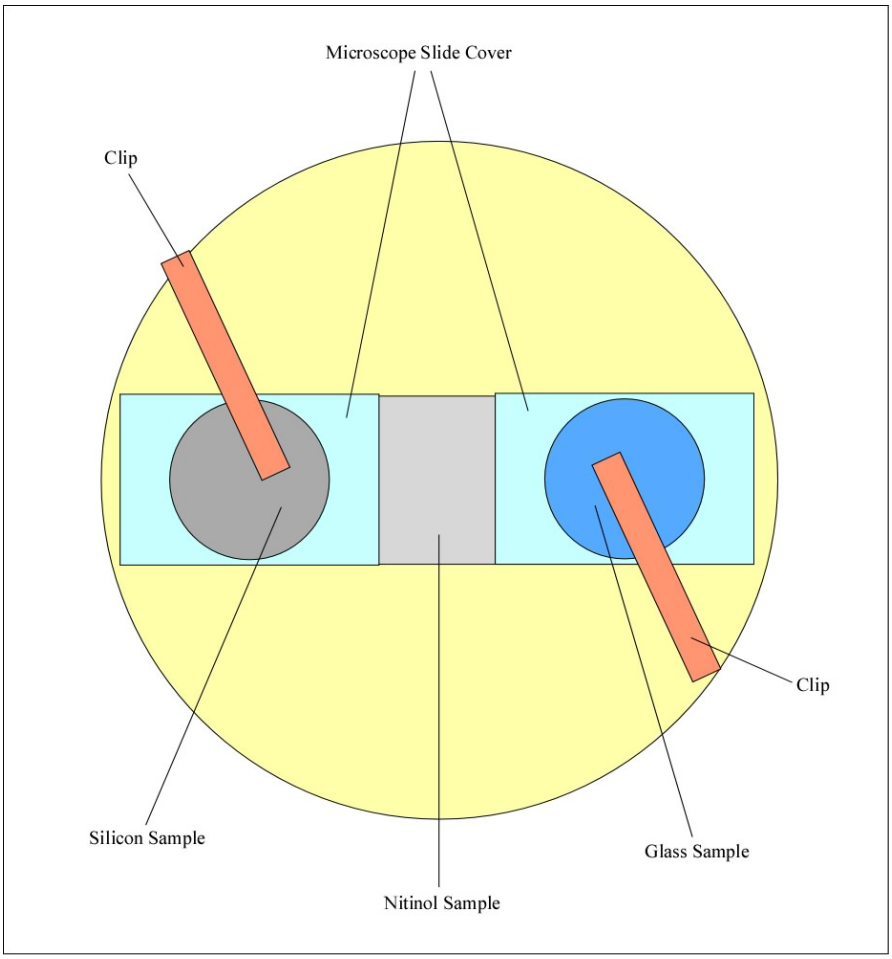

Figure 4.3: Magnetron Sample Orientation

Principles of Sputtering

The films deposited for characterization should be homogeneous and very pure, so they must be formed in an environment free of oxygen and other reactive atoms or molecules. The method chosen to grow the thin films used in these experiments is a special form of physical vapor deposition called sputtering. Two different sputtering methods were used to create these samples: dual ion beam sputtering system (or DIBS),

and magnetron sputtering. Although these deposition methods utilized are very similar, they are not entirely identical. In the pages that follow, the principles of DIBS and magnetron sputtering will be explained in some detail.

Both techniques require a sufficiently high vacuum in order to allow the sputtered atoms to reach the surface of the substrate material without being deflected by or reacting with stray atoms. Additionally, the target material should be pre-sputtered before deposition in order to detach any contaminants from the surface of the target. The sample holders are equipped with a shield that can be extended during pre-sputtering to keep these undesirable contaminant atoms from attaching to the surface of the substrates. In both systems, the sample holders have a mechanism that allows them to rotate at a constant rate during deposition so that the films deposited have a more uniform thickness.

The DIBS used for these experiments was manufactured by Commonwealth Scientific Corporation. This system functions by essentially "splashing" atoms onto the surface of the substrate via momentum transfer. A beam of argon ions is created by an ion gun (RF50) by allowing RF electromagnetic waves to interact with neutral argon atoms inside the gun, which creates a plasma of relatively low temperature (1 eV) argon ions and free electrons. [18]

The argon ions are extracted from the sheath layer in the plasma by two grids: a screen grid that is in direct contact with the plasma, and an accelerator grid that is separated from the screen grid by a couple of millimeters.[19, 20, 21] Both grids are typically made of molybdenum, and are carefully aligned with each other. The screen grid is usually kept at 800 volts, and this voltage determines the potential of the ion beam.

Ionized atoms move through the holes in the screen grid and are accelerated towards the negatively biased accelerator grid (typically kept at a voltage of approximately 100 volts). Because the holes in both grids are aligned with each other, the low energy ions that pass through the holes in the screen grid will pass unobstructed through the holes in the accelerator grid after they have been accelerated. Aligning the screen and accelerator grid is extremely important, as otherwise the accelerated ions will sputter the material in the accelerator grid instead of the material in the target.

The current caused by the electric potential applied across the screen and accelerator grids is not linear but given by Child-Langmuir's law [22] and resembles that of a vacuum diode. As ions are moving through the holes in the screen grid, positive space charges build up near the screen grid and slow down further positive charge injection until they are removed by the negative potential on the acceleration grid. The I-V relation is given by the following formula:

$$I = \frac{4}{9}\frac{\varepsilon_o A}{d^2}\sqrt{\frac{2e}{m_e}}V_o^{3/2}$$

Where ε_o is the dielectric constant of vacuum, A is the cross sectional area of the ion beam, d is the distance between the plates, e is the elementary charge, m_e is the mass of the electron, I is the ion beam current between the two screens, and V_o is the electric potential between the two grids. From equation above, it is clear that the smaller the distance between the grids the larger the beam current will be. Although the ion current may also be increased by increasing the voltage between the grids, the energy of the individual ions in the beam will also increase which is undesirable in certain situations.

Immediately outside the acceleration grid the positive argon ion beam is neutralized by free electrons generated by a heated “neutralizer filament” made of tungsten. By neutralizing the ion beam, charging effects in the target material can be avoided, which allows insulating materials to be sputtered. The RF50 ion gun used in the DIBS apparatus does not contain a deceleration grid, but as the target and the neutralizer filament are quite close to ground, the ions are believed to decelerate slightly after passing through the acceleration grid. A schematic diagram of the ion gun is shown in the Figure below.

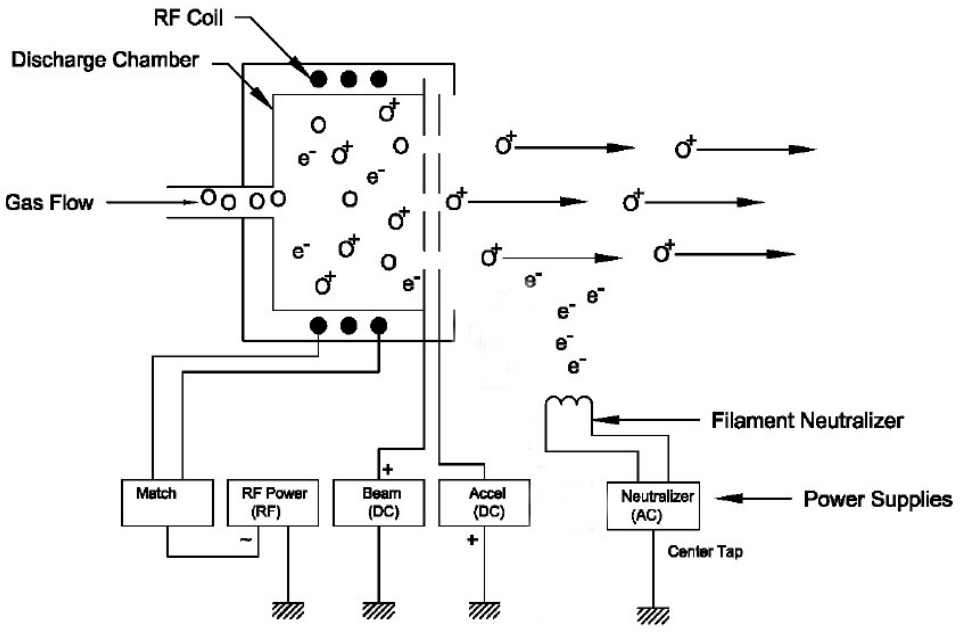

Figure 4.4: Schematic Diagram of RF Ion Gun [19]

In the DIBS system used for these experiments, argon gas passes through a port into a quartz discharge tube. Within this tube RF electromagnetic waves are generated by the RF coil and ionize the plasma. Because the sample is never exposed to the plasma

using this sputtering technique (after all, the plasma is confined within the ion gun), deposition can be performed at low temperatures. The argon atoms bombard the target surface and eject target atoms by momentum transfer. These ejected particles travel in a straight-line until they come into contact with other atoms - such as those of a substrate material placed in their vicinity.

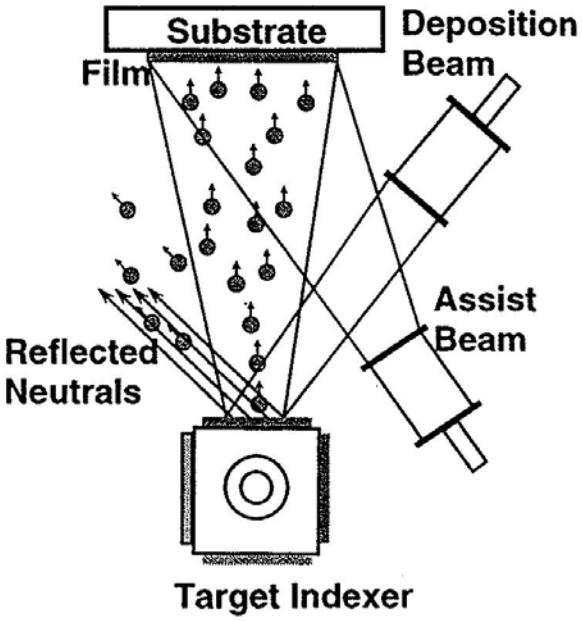

Figure 4.5: DIBS Sputtering Diagram [23]

One of the drawbacks of the DIBS method is that it is relatively slow, so thicker films take longer to deposit. During sputtering, the temperature of the ion gun increases dramatically, even when a water cooling system is used. Sustained high temperatures may damage the components of the ion gun, so in order to avoid this deposition time was limited to 20 minute sessions. This time constraint limited the overall thickness of the

iron films to approximately 300 nm. Thicker films could be deposited over multiple 20 minute sessions, to allow the system to cool down between uses.

The DIBS technique has several advantages over standard magnetron and RF sputtering systems. Because the plasma is only exposed to the discharge tube (which can be baked out at high temperatures), DIBS deposition is potentially much cleaner than other sputtering methods. Additionally, the process window associated with DIBS deposition is much larger than that of magnetron and RF sputtering techniques, meaning that a wide range of sputtering pressures, ion energies, and ion densities will facilitate film growth. Since DIBS deposition may be performed at lower pressures than other sputtering techniques, the number of impurities introduced into the sputtered films is significantly reduced. Also, the substrates are not exposed to plasma, deposition takes place at lower temperatures. Finally, the high kinetic energy of the atom beam (anywhere between 3 and 10 eV) may lead to improved adhesion of film to the substrate materials.[18]

The magnetron sputtering system works under the same basic principle as the DIBS, in that inert atoms are ionized and fired at a target of desired film material in order to knock the atoms out of the target and onto the substrate material. In magnetron sputtering, however, the plasma is created *between* the target and the substrate material, which exposes the samples directly to the plasma.[24, 25] Because the substrate materials are directly exposed to the plasma, the free electrons, and the other negatively charged ions within the plasma, magnetron sputtering is less suitable for coatings on temperature sensitive substrates. Another key difference between magnetron sputtering and other techniques is that the free electrons near the target material are corralled by magnets,

which both reduces their ability to bombard the substrate, and vastly increases their probability of ionizing argon atoms.

The magnetron sputtering system used in these experiments also uses a confocal arrangement of target materials all aimed at a common location which, combined with the rotation of the substrate holder during deposition, results in a film thickness variation of less than 2%. Additionally, this particular magnetron sputtering system has a smaller vacuum chamber (called a load lock) that is separate from the main vacuum chamber. The main chamber can remain at high vacuum while the smaller chamber is brought up to atmospheric pressure and the substrate materials are secured on the sample holder. After samples have been loaded, the smaller chamber can be sealed and brought down to a pressure comparable to that of the main chamber so that the sample holder may be inserted into the main chamber. Placing the substrate material into a volume at low enough pressure is vastly expedited with the use of a load lock mechanism.

The Residual Gas Analyzer

The residual gas analyzer, or RGA, is used to monitor the types of gasses present in the vacuum chamber. The RGA works by ionizing a sample of gas then measuring the different masses of these ions. The RGA measures the composition of the gas in the chamber every few seconds so that the composition of the gasses inside the chamber can be monitored during deposition. The RGA may also be used in concert with a helium source to detect leaks in the vacuum system, as the RGA will measure a sudden increase in helium ion pressure when helium gas is passed over the leak location.

The RGA "counts" the number of ions of a given mass using a set of 4 cylindrical rods with different AC and DC voltages of varying frequencies called an RF quadrupole. For a given frequency, only certain ions with a specific charge to mass ratio can pass between the cylindrical rods and reach the ion collector. The RGA plots the quantity of each molecule or atom present (or the pressure of each respective species) according to its unique mass-to-charge ratio (or the atomic weight of the element detected). On the DIBS system used for these experiments, the RGA is mounted between the turbo pump and the high vacuum valve. [26]

Deposition Parameters

The samples were sputtered in two separate deposition systems, and under the conditions detailed in Table 4.1. For DIBS deposition, the ratio of acceleration to beam current indicates the quality of grid focusing – when this ratio is less than 10%, the grid focus is of good quality. Although the DIBS does not measure the emission current of the neutralizer filament, the current through the tungsten neutralizing filament is controlled, and was kept at 5-6 amperes for the duration of the sputtering sessions. The neutralizer emission current should be larger than the beam current in order to minimize space and surface charging of the target material.

Under optimal circumstances, the DIBS system sputters the same amount of material per unit time; a drop off in deposition rate indicates a decline in the system's functionality. The deposition rate of the magnetron sputtering system varies according to the material being sputtered, however. In magnetron sputtering the production of argon ions is enhanced by magnetic fields, and the strength of the magnetic field outside

the plasma depends on the properties of the target material, including its magnetic moment and the direction of its easy axis. Because the magnetron makes use of magnetic fields to move the plasma and the sputtered target atoms, the atomic weight of the target material becomes a factor in the deposition rate.

Table 4.1: Deposition Parameters

Sample Name	**121007**	**121809**	**062410**	**070810**
Deposition Technique	DIBS	DIBS	Magnetron	Magnetron
Base Pressure (Torr)	-	-	5.9×10^{-8}	7.0×10^{-8}
Argon Flow (sccm)	-	15	23	23
Pre-sputter (minute:	-	2:00	2:00	2:00
Seed Layer – Ti				
Thickness (nm)	23	-	5.4	5.4
Time (minute: second)	-	0:20	2:46	2:46
Power (Watt)	-	216	100	100
Pressure (Torr)	1.2×10^{-4} *	1.2×10^{-4} *	1.5×10^{-3}	1.5×10^{-3}
Film Layer				
Composition	FeSi at.	FeSi at.	NiFe at.	FeSi at. 3%
Thickness (nm)	320**	120	900	120
Time (minute: second)	-	20:00	13:38	21:26
Power (Watt)	-	216	200	200
Pressure (Torr)	1.2×10^{-4} *	1.2×10^{-4} *	1.5×10^{-3}	1.5×10^{-3}
Cap Layer – Ti				
Expected Thickness	15	-	5.4	5.4
Time (minute: second)	-	0:20	2:46	2:46
Power (Watt)	-	216	100	100
Pressure (Torr)	1.2×10^{-4} *	1.2×10^{-4} *	1.5×10^{-3}	1.5×10^{-3}

* This is a typical value, this parameter was not recorded during deposition.

** This value estimated from data on our poster presentation “The Effect of Plastic Deformation on the Magnetic Properties of Thin Iron and Permalloy Films” in 2007.

Difficulties Encountered

There are numerous components that work in concert to make the DIBS function – from water cooling lines to electrical cables and beyond – so this section will only cover the difficulties that were specifically encountered during this project. Detecting an issue with the system is often as difficult a task as repairing the problem, as the series of difficulties encountered over the course of this research project exemplifies.

The neutralizing filament erodes in the same way that atoms are ejected from the target material. Over time, incident ions of the plasma beam eject atoms from the surface of the neutralizing filament until it has been so eroded that it snaps and must be replaced. In addition to this failure mode, the filament will also wear down from oxidation effects caused by its high temperature and oxygen molecules present in the vacuum system. Although replacing the filament is relatively simple, the process of removing the ion gun from the system is somewhat lengthy and delicate – anything but the most careful of handling may damage or contaminate the source tube in which the plasma is generated.

The DIBS uses a system of tubes that direct chilled water around and through various parts of the apparatus to keep them from overheating while it is in use. While creating the samples for these experiments, one of the chilled water tubes cracked and began leaking. Because the DIBS system uses a significant amount of electricity to run the ion source and the vacuum pumps, a water leak is very hazardous to both the equipment and to the experimenters. In order to fix the line, the plastic tubing must be cut past the cracked portion, then fit it with an appropriate sized Swagelock tube fitting and reattached to the system.

Although the original intention was to create a complete series of film thicknesses, during sample creation the DIBS system began to fail. The system failure was discovered after a lengthy sputtering session – that should have deposited a relatively "thick" thin film – resulted in semi-transparent films on the glass wafer substrate, which indicated that the deposition rate was far less than expected.

In order to determine if the argon beam was bombarding the targets with enough force, or if the beam was somehow missing the target material, a simple experiment was performed. The surfaces of the vacuum chamber and target were covered with ordinary aluminum foil, and then the chamber was sealed and pumped down according to normal procedures. Once at the appropriate pressure, the ion gun was turned on for a period of 5 minutes, enough time for the ion beam to punch a hole in the aluminum foil at its point of contact. Whether the gun and target were misaligned or the ions were simply not energetic enough could be determined depending on the absence or presence and location of a hole in the foil. After bombarding the aluminum foil for 5 minutes, the chamber was allowed to cool before opening. The foil had not been damaged by the plasma beam after 5 minutes of sputtering, so clearly the issue lay not in the alignment of the target and gun, but in the inability of the ion gun to create an energetic enough plasma beam.

After determining that there was a problem with the ion gun itself, it was removed from the system and opened up. Upon examination it was discovered that a significant amount of the argon beam had backscattering and had coated the inside of the plasma tube. It appeared that the accelerator grid was positively charged (instead of negatively charged) during sputtering, which caused the most of the argon beam to be reflected back

into the gun, which sputtered material out of its metallic interior and onto the inner surfaces of the gun.

In order to remove the coating on the inside of the ion gun, its component parts were soaked in a solution of 10% nitric acid, 90% de-ionized water for several days. The difficulty in this process, aside from the obvious danger of handling nitric acid, is that only the glass and ceramic components could be submerged, since the acid would have corroded any metallic portions of the gun. This is because nitric acid is highly reactive with metals but not with glass, so by submerging the glass and ceramic portions of the ion gun the nitric acid was able to remove the undesirable metallic buildup from these portions of the gun. It was considerably simpler to simply replace the tubing and bussing inside the ion gun than to attempt to remove the metal coating from them. Once the metallic coating backscattered in the ion gun had been removed, it was reassembled and began functioning properly once again.

Over the course of this thesis research, the DIBS equipment was moved to a new location, and after moving the DIBS equipment another problem was discovered: reduced water-flow through the target and substrate holder. Although the water flow through the target-holder was fixed by soaking the piping with vinegar and repeatedly blowing the entire cooling water system with compressed air of up to 80 psi, this procedure failed to repair the substrate holder. In fact, employing the same approach for the substrate holder resulted in a water leak in one of the bellow-tubes. In the end, vinegar did not work to dissolve the blockage in the water lines, so a solution of 10% hydrochloric acid and 90% de-ionized water was used to clean the systems water chilling tubes. At the time of this

writing, these issues have been resolved, but new issues with the high vacuum valve have arisen.

PART II:

SAMPLE CHARACTERIZATION

CHAPTER V: APPLICATION OF STRESS

The ability to reliably and reproducibly strain our samples is of the utmost importance for this research project. The ultimate goal is to discover a trend that relates the amount of strain (and in turn, the amount of deformation) in the film to its magnetic moment so that a model can be developed that predicts how the magnetic moment changes after plastic deformation is introduced. This section explains the basic concepts related to material deformation, how the amount of strain in the film was determined, and the method by which each sample was strained.

Stress and Strain

Despite the casual usage of the terms "stress" and "strain" outside of the laboratory, they have specific meaning in a scientific context. "Stress" refers to the amount of force applied to a cross-sectional area, and is illustrated in Figure 5.1a. "Strain" quantifies the change in length of a sample, and is often expressed in percent change of length, or as a unit less measure of mm/mm. In other words, strain is calculated by taking the ratio of length change to initial length, and is illustrated in Figure 5.1b. Stress and strain information is expressed as a graph with stress along the y-axis and strain along the x-axis. When plotted with appropriate units, Young's modulus may be estimated from the slope of this graph.

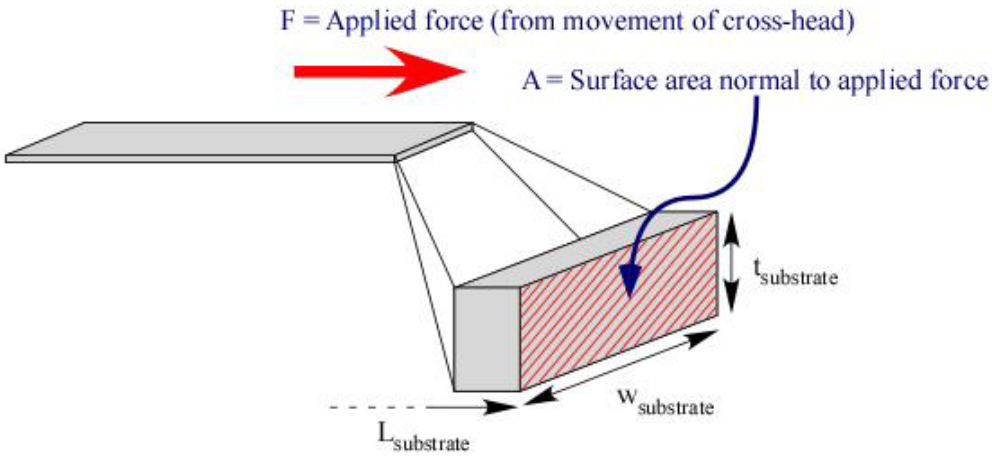

(a.) Stress

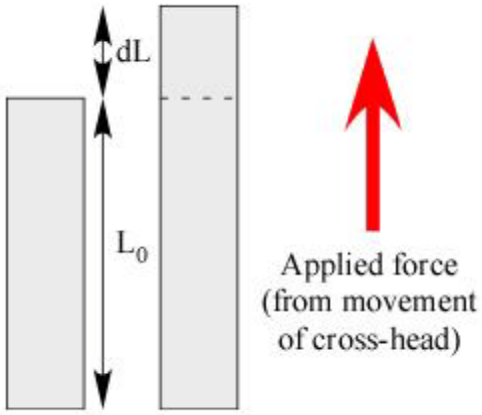

(b.) Strain

Figure 5.1: Stress and Strain

In the substrate section, Nitinol sheet metal was discussed at length. To briefly review, Nitinol undergoes a solid-state phase transformation that propagates through the material when it is placed under stress. [6, 27] These phase transition fronts nucleate at locations of high stress (for instance, where the substrate is gripped in the apparatus), and

then widen or move throu.gh the sample. Because these transformations fronts nucleate and then propagate, the amount of strain may not be homogeneous throughout the film on the Nitinol's surface. Inhomogeneous strain has been observed in super-elastic Nitinol wires and sheet metal. [28] The strain distribution upon bending of sheet metal is not yet fully understood. Additionally, no research has been done to investigate the strain distribution in coated super-elastic Nitinol sheet metal. The work of Kyrakides and others suggests that care must be taken when measuring strain in these experiments, since strain that is experienced by the film – and not the net strain throughout the entire sample – influences the evolution of the magnetic characteristics that are being measured.

From observation of the material as it is strained, it is clear that the nucleation density of transformation sites in the Nitinol sheet metal depends on the strain-rate.[15] When the strain-rate is high, there are a large number of transformation sites crisscrossing the surface of the material that appear to widen as the net strain of the sample increases. During slow straining, a transformation front forms at one or both grips, then appears to move across the surface of the material, then retrace its path upon unloading.

According to the work of Shaw et al., the phase transformation is controlled by thermal effects. The Austenite to Martensite (A→M) transformation is exothermic, so heat is released locally and increases the temperature of the Nitinol. As the temperature of the Nitinol increases, the stress required for the A→M transformation also increases. At room temperature, and high strain rates, large variations in the temperature of the Nitinol sample are expected. As the temperature around each nucleated transformation front increases, the stress required to transform the material to Martensite increases. Figure 5.2 plots the required stress for the A→M and M→A (clearly, Martensite to

Austenite) transformation as a function of the temperature. For each transformation, two different critical stresses are plotted: the nucleation critical stress (σ_N), which denotes the amount of stress required to *nucleate* a new phase front, and the propagation critical stress (σ_p) which denotes the critical stress to *move* an existing phase front. After the A→M transformation, the local temperature of the Nitinol has risen, causing its critical transformation temperature to be higher than the critical nucleation temperature of the unheated areas in the sample. In this case, the front does not move and instead Martensite is formed at new locations with lower temperatures.

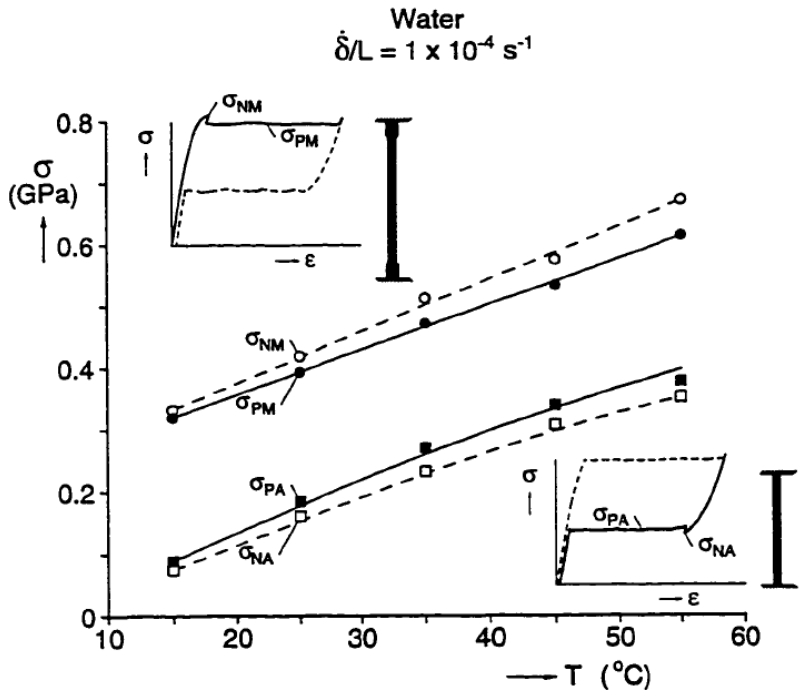

Figure 5.2: Nucleation and Propagation Stress for Nitinol Phase Transformation

Stress required for nucleation (σ_{NM}) and propagation (σ_{PM}) of Austenite to Martensite transformation and nucleation (σ_{NA}) and propagation of (σ_{pA}) Martensite to Austenite transformation as a function of temperature.[27]

In order to prevent the nucleation of additional transformation sites, the heat released by the transformed Nitinol must not dramatically heat the rest of the sample. To reduce the temperature variation in the sample caused by transformation, the Nitinol may be strained under isothermal conditions (i.e. in a water or oil bath), so that after A→M transformation, the temperature at the transformation site is below the propagation temperature. In conditions that are not isothermal, a reduction in the crosshead-rate lowers the number of nucleation sites, which results in an amount of heat generated that can be efficiently dissipated to the surrounding environment. This effect was observed in both the bare and plated Nitinol sheet metal used in these experiments. High strain-rates resulted in the formation of a large number of thin, needle-like fingers that widened as net stress on the sample was increased. [28]

It is possible that at extremely high strain rates the number of nucleation sites may be macroscopically homogeneous over the entire sample, causing the strain at various locations in the sample to be more homogeneous. However, rapid straining of plated Nitinol sheet metal caused portions of the deposited film to come loose from the substrate in prior experiments. Slower strain rates (which result in the formation of only one or two transformation fronts) minimize film detachment. The mechanism behind this effect is unclear, as is the role of temperature variation within the sample. It is possible that the rapid nucleation and propagation of transformation fronts in the Nitinol substrate caused the film detachment observed in previous experiments.

In order to reduce the potential for film loss, the samples were strained very slowly (between 1.6 and 3 mm/min), with the intention of minimizing the number of transformation fronts formed in the material. Only one transformation front was

observed during stress tests performed at these rates, so the stress-induced transformation happened most likely formed at a high stress location and then moved through the sample along the stress axis, primarily by the movement of the transformation front rather than nucleation of new transformation sites.

Straining Apparatus

The Instron 5566 strains samples axially by moving one crosshead upward while the other crosshead remains stationary. The crosshead movement determines the average or tensile strain in the sample. The apparatus strains the material by moving the crosshead, and the strain rate is controlled by specifying the rate of crosshead movement. The net or total strain throughout the entire sample is measured by the movement of the crosshead, but since Nitinol does not strain homogeneously and film is deposited in a certain area, this manner of measuring strain does not necessarily relay information about the amount of strain experienced in the film itself. In fact, measuring the strain via the crosshead movement would either over- or under-estimate the amount of strain in the film, as the strain is highest where the phase transition has occurred, and lower in the areas that have not undergone any transition. [28] It was necessary to come up with another method to measure strain in the film specifically, so a non-contact advanced video extensometer (or AVE) was employed and is described in detail in the following section.

The Advanced Video Extensometer (AVE)

There are many advantages to using an advanced video (non-contact) extensometer over a contact extensometer. The AVE uses a very sensitive video camera

to measure how the distance between marks on a sample change as it is strained. Contact extensometers must be attached to the sample during strain, and can affect the way the sample experiences the applied stress.

The AVE measures an initial gauge length between the dots marked on the sample, which is used to calculate the strain in the sample as stress is applied. For these experiments, the dots are placed on the *back* of the sample (so as not to mar the film itself) in the center and directly behind the film. The marks were placed on the back of the samples, opposite the film, as measuring the strain in that localized area of the substrate should give an accurate estimation of the strain in the film itself. Because of the placement of the marks, the AVE measures the strain in the middle of the sample where the film is located, and does so without contacting the sample and adding undesirable torque or stress. An additional benefit of the particular AVE apparatus used for these experiments is that it is equipped with a high intensity pulsed low voltage LED lighting and filter system that maintains optimal lighting conditions during measurement and reduces reflection on shiny samples (such as ours), improves the overall accuracy of measurements.

Methods and Parameters of Straining

There are, in fact, a couple of different methods by which samples can be strained in the Instron 5566. As both the loading and the unloading strain rate are important factors in regard to the nucleation and propagation of transformation sites in the Nitinol substrate, it was necessary to develop a method for straining that kept the net strain-rate both slow and constant. Because of this requirement, the methods most applicable for

these experiments were the “tension profiler” method and a combination of “tension” and “compression” methods.

The “tension profiler” method strains the material at a specified rate of crosshead movement, reaches the desired percentage of strain, then unloads the sample at the same specified rate. However, in this method of straining, the “desired percentage of strain” is determined by the tensile or net strain over the entire sample and is calculated using the crosshead displacement. Although AVE measurements can be taken using the “tension profiler” method, these values cannot be used to control the stopping points of the experiment. Since these samples do not strain homogeneously, the net or tensile strain as measured from the crosshead displacement is not necessarily equivalent to the strain in the film at the middle of the sample. The “tension profiler” method could not be configured to control the maximum strain via AVE measurements, and could only be controlled by the crosshead movement.

In order to determine if controlling the apparatus via tensile strain would allow the film to be strained the desired amount the “tension profiler” method (which both loads and unloads the test sample) was used to strain a bare, un-sputtered piece of Nitinol sheet metal. The AVE strain was plotted against the crosshead (or tensile) strain, or in other words, the tensile strain as calculated from the crosshead movement was plotted on the vertical axis and its corresponding AVE strain was plotted along the horizontal axis. This information was used to estimate the percent crosshead strain that approximately corresponded to percent AVE strain, and is illustrated in Figure 5.3. It is clear from the figure that the relationship is far from linear, and in fact, the AVE strain – tensile strain

relationship for substrates plated with a thin film varied from this initial test and among different samples.

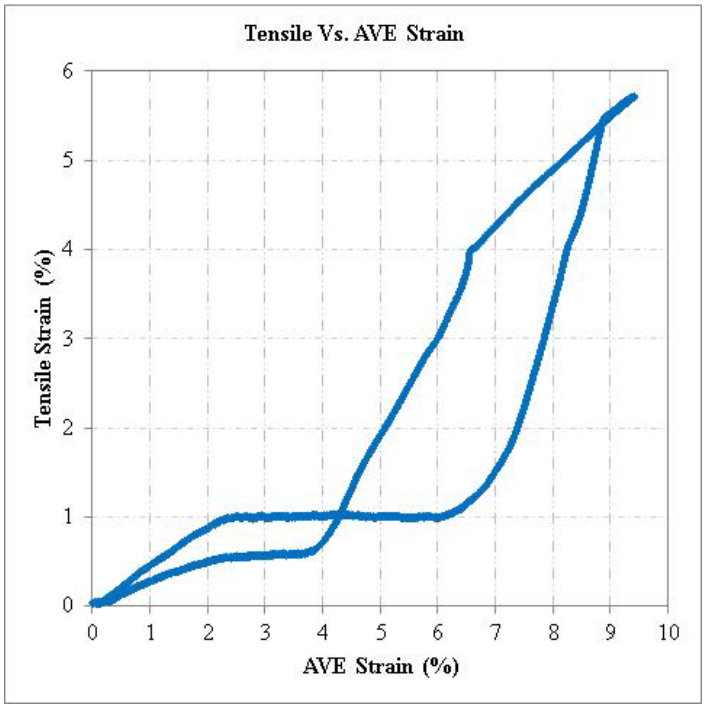

Figure 5.3: Tensile Versus AVE Percent Strain

The benefit of the "Tension Profiler" method is that the strain rate can be predetermined and will load and unload the sample at this constant rate. The major drawback of the Tension Profiler method is that the AVE strain information cannot be used to control the end of test, making it impossible to strain the *film* on each sample to the same amount.

Upon testing a sample sputtered with a thin metallic film, it was discovered that the presence of the film changed the relationship between AVE and tensile strain. Because the amount of strain experienced by the film using the Tension Profiler method

could not be reliably reproduced, this method was abandoned in favor of a combination of tension and compression test methods. Additionally, with the Tension Profiler method, the strain test could only be ended by reaching a set *net* strain as calculated from the movement of the crosshead. With a combination of Tension-Compression tests (two-part tests) the test could be ended using the strain calculated by the AVE, which more accurately strained the film area to the desired degree.

The tension method *only* increases the applied stress on the sample, and the compression method *only* decreases the applied stress on the sample, so a combination of tention and compression methods were used in order to load and unload the sample using AVE measurement controls. Using this combination of methods, identical experiments could be performed on each sample, and the film could be strained to specified values without ambiguity. The apparatus used for these experiments could not be configured to control the rate of strain using AVE measurements, so the strain rate for these tests were determined by the rate of crosshead movement just as in the tension profiler tests.

During the tension-compression tests, the samples were strained at a rate of 0.3 mm/minute; during the tension profiler tests the strain rate was 0.03%/second, which translates to a rate of approximately 0.72 mm/min. The 121809 sample was strained using the tension profiler method, and the tensile strain value was used as a means of ending the test. For this reason the strain in the film as determined by AVE measurements does not vary in predictable steps. However, since the percent strain for all our samples is in the same general range, comparison of the results of measurements made both by tension profiler and tension-compression methods is possible. Chapter VII details the results of these various experiments.

Bending Over Cylinders

In addition to stretching experiments in the Instron, sputtered Nitinol samples were stretched by bending over rigid cylinders with well-defined radii. Appendix B details the process by which bending strain was calculated using the radius of the cylinder. What is unique about these bending experiments is that the samples were measured in mutually perpendicular orientations. That is, after the sample was strained, it was measured in the VSM oriented such that the field lines moved through the film perpendicular and parallel to the straining cylinder's axis as illustrated in Figure 5.4 below. The results of these bending experiments are included with the lateral straining results in Chapter VII.

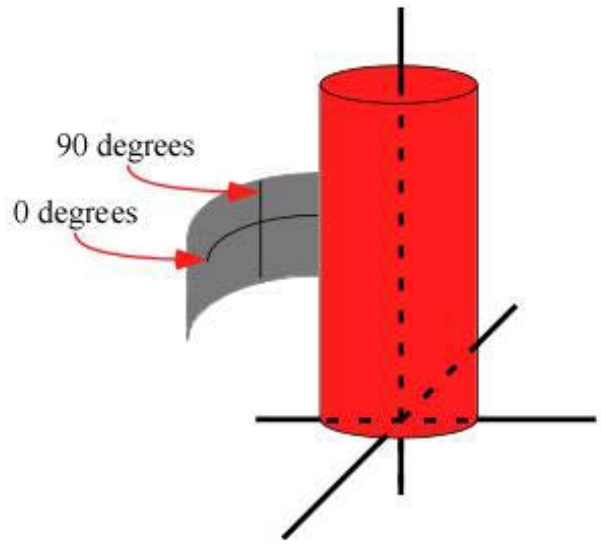

Figure 5.4: VSM Orientation for Bending Strain

CHAPTER VI: OPTICAL MICROSCOPY

In order to keep a record of the visual appearance of deformations in samples that had been strained, numerous optical microscope photographs were taken. The procedure for taking these pictures developed over the course of these experiments, and is detailed in the pages of this chapter.

Optical Microscope and Camera

Figure 6.1: Nikon Coupler, Optical Microscope and Pixelfly Camera

A Pixelfly QE camera from PCO was used to record the images taken with a Nikon optical microscope. The Pixelfly is a monochrome camera equipped with a CCD chip that has a 12 bit dynamic range (1392x1024 pixels). The camera was attached to the microscope using a 0.65x Nikon coupler. The Nikon coupler and microscope apparatus used for taking microscope photographs in these experiments is pictured in Figure 6.2. All the photographs presented in Chapter VII were taken in bright field reflected-light illumination mode.

Figure 6.2: Nikon Coupler and Pixelfly Camera

Camera Software

CamWare and Paint Shop Pro 7 were used to process the optical microscope photographs taken during these experiments. CamWare is a camera control program, and saves images in .tif format which are of high-quality but are large files. Paint Shop Pro 7 is a common graphics editing program, and was used to convert images from .tif format

to .jpg format, which is a compressed format that is much smaller but retains a high quality image.

Photography Procedure

A series of optical microscope photographs was taken in order to document the evolution of deformation effects in the film. To compare these photographs, it was necessary to examine the same general areas of the film after each successive strain test. Over the course of these experiments a procedure was developed for taking photographs of the same area of the film with the same orientation to allow for clearer comparison.

To ensure that the samples were oriented the same way during each series of photographs, a frame was fitted to the microscope stage. The corner of each sample was aligned with the corner formed by a halved glass microscope slide attached to the stage. Figure 6.3 below illustrates the manner in which the microscope slide was cut and how it was oriented on the microscope stage, as well as how the sample was mounted into this frame. Additionally, the film was marked with a fine point permanent marker in 9 places on the film itself as illustrated in Figure 6.3. The marks were placed on the film to allow photographs of the same areas of the film to be taken after each straining session, so that comparisons of the number of deformations in the film could be made.

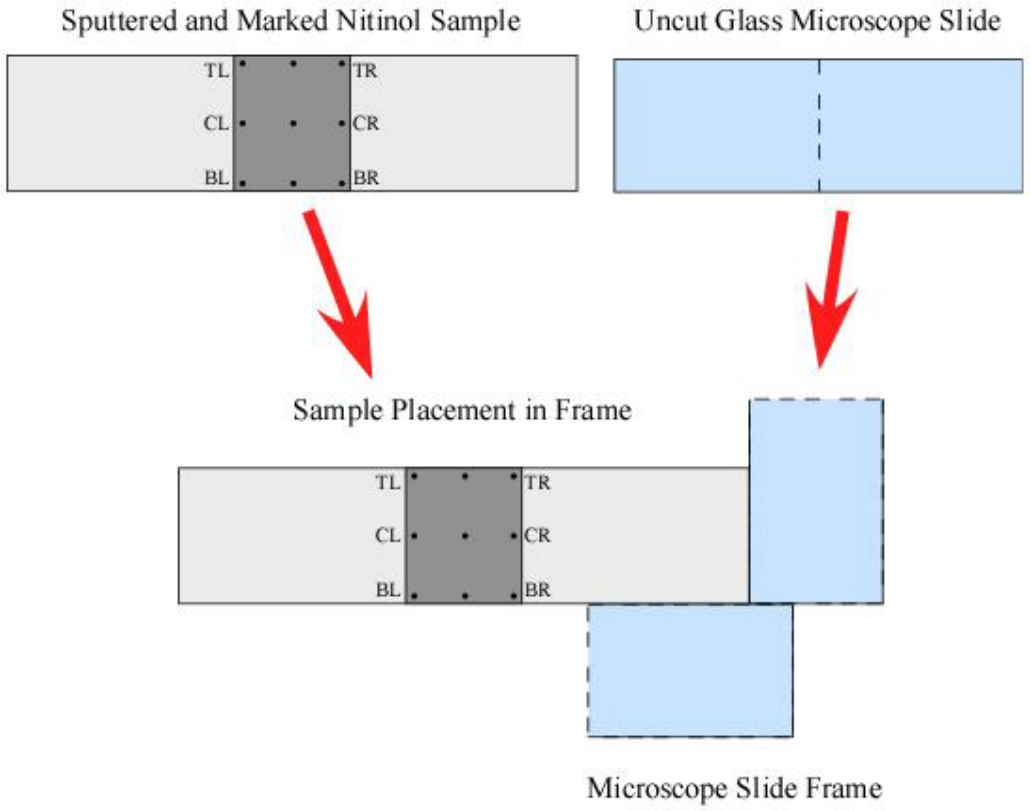

Figure 6.3: Optical Microscope Marking and Orientation Frame

Although photographs of the first sample (121809) were only taken after it had undergone the maximum amount of strain, the remaining samples (062410 and 070810) were photographed extensively after each straining session. The difficulty encountered when attempting to find common locations on the 062410 sample led to the development of the marking method previously described. Comparison of the 062410 sample was possible, however, because the edges of the sample and the film were included in the photographs, which allowed for the orientation to be corrected. Common locations on

the film’s surface were found using defects inherent in the film before any strain was introduced.

CHAPTER VII: VIBRATING SAMPLE MAGNETOMETER (VSM)

The pages of this chapter will discuss the principles of measurement via the Vibrating Sample Magnetometer or VSM, as well as the production of a sample holder fitting to our samples and the details of our measurement techniques.

Principles of VSM Measurement Technique

When a magnetic material is placed in a constant magnetic field, a dipole moment will be induced in the material, aligned with the applied magnetic field. As the applied field increases, the respective domains within the material begin to align with it eventually reaching a point when all the magnetic domains are aligned in the same direction (called the "saturation magnetization").

The magnetic dipole moment induced in the sample will create a magnetic field in and around the sample itself. When the magnetized sample is mechanically vibrated this magnetic stray-field induces an electric field of the same frequency in a set of pick-up coils. Because the electric field induced and measured by the pick-up coils is created by the net magnetic moment of the sample material, the sinusoidal electric current measured in the pick-up coils is proportional to the magnetic moment induced in the material by the applied magnetic field. [29, 30, 31]

The VSM measures the magnetic moment of a sample as a function of the applied magnetic field, which is supplied by a water-cooled electromagnet. At the start of the

measurement, the magnetic field is increased to the maximum value, which is set by the experimenter. Depending on the strength of this maximum field and the properties of the ferromagnetic material, most or all of the magnetic domains of the sample will be aligned parallel to the magnetic field, which results in a net magnetic moment over the entire sample and creates a magnetic stray field due to the net magnetic moment in the sample.

Between the pole pieces of the large electromagnet, four small pick-up coils (one on either side of the sample) are positioned. During measurement, the sample is vibrated up and down at a given frequency, and the magnetic stray field that has been induced in the sample will create a time varying magnetic flux through the pick-up coils. According to Faraday's law, this time-varying flux will create an induction current in the pick-up coils, which is measured after passing through a lock-in amplifier. The VSM measures and averages this fluctuating current (which is proportional to the magnetic moment of the sample) for a specified time period, called the "time constant." The first measurement is taken at a large maximal magnetic field, when the sample has (ideally) reached its saturation magnetization.

After a measurement has been made at the maximum field value, the VSM stops measuring the current in the pickup coils and lowers the applied field. Once the applied magnetic field has reached the next field value, the magnetic moment (or, the induced current) is measured again for the specified time period. Once the applied field has been reduced to zero, many of the formerly aligned magnetic domains have relaxed into random orientations. However, some of the magnetic domains will remain aligned with the initial maximum field direction, and this value is referred to as the "remanent magnetic moment" of the material.

As the applied field is further reduced, the magnetic domains become even less aligned, until there is no net magnetic moment in the sample. This magnetic field value is referred to as the coercivity of the material. The field continues to be reduced until the sample reaches its saturation value once again, before being reversed back to zero and continuing to increase to the initial maximum field value. These data points collectively form what is referred to as a (magnetic) "hysteresis loop." Saturation magnetic moment, remanent magnetic moment and coercivity are illustrated in the basic hysteresis loop pictured in Figure 7.1. A "dual remanence" and "dual coercivity," are mentioned in relation to some of our samples, which refer to the apparent lumps in the hysteresis loops and the estimated corresponding coercivities and remanent magnetic moments. This hysteresis lump is also sometimes referred to as "the two-step" effect, as the magnetic moments of the molecules in the material seem to be aligning in a step-like manner.

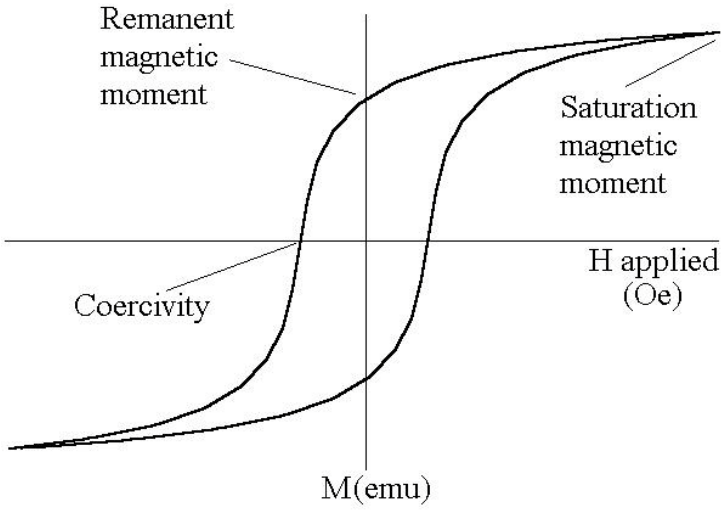

Figure 7.1: Hysteresis Loop

Before starting a measurement, it is necessary to perform an optimization procedure, in which the sample is centered between the pick-up coils. To do this, the field is set to a constant value, and the sample begins to vibrate. As the sample vibrates in the constant field, it generates a constant signal. As the sample is displaced from the center of the coils in the vertical direction the signal decreases. As the sample is displaced forward and backward of the center of the coils the amount of sample material vibrating in the constant field decreases, so the signal generated decreases. Unlike the other two axial directions, moving the sample to the right and left of the center point will cause the measured signal to increase. This is because the constant field is only constant to a certain degree, and between the coils the field diverges very slightly. The amount of magnetic flux directly against the plates containing the coils is slightly higher than between the coils, and is minimal at the center point between coils.

Measurement Parameters

Table 7.1: VSM Settings

	High Field	Low Field
Time Constant (s)	0.3	0.3
Measurement Points	1,024	1,024
Peak Field (Oe)	7,000	200
Induction Range (emu)	0.1 to 1	0.1 to 1
Field Range (Oe)	10,000	1,000

The experimenter sets a number of important variables before starting a measurement on the VSM, such as the “time constant” mentioned previously. These settings must be adjusted in order to obtain meaningful and useful measurements of the

material's magnetic properties. Table 7.1 lists these variables, as well as the values we used for the different VSM measurements we made. The function of each of these settings is discussed in the following pages, as well as the reasons why we chose the particular values used for our measurements.

A longer the time constant results in more accurate the measurement of the sample's magnetization. Longer time constants result in longer overall measurements, so accuracy and efficiency must be carefully balanced in order to obtain useable results for all of our samples. For our experiments, we set the time constant to 0.3 seconds, which allowed a good amount of accuracy while expediting the measurement process considerably.

The induction range is measured in emu, and determines the y-axis range on the hysteresis curve. This setting is usually either 0.1 emu or 1 emu, depending on the magnetic moment of the material. During optimization, it is immediately apparent whether the induction range is correct or not, as too small an induction range will return output values outside of the range VSM is able to measure.

The total number of measurements taken by the VSM is referred to as the "total points," and is set to a maximum value of 1,024. Fewer measurement points will result is a blockier, more discretized hysteresis curve, so we used the maximum number of measurement points for all of our measurements.

The test speed determines how long the VSM waits before resuming measurement of the induced current in the coils. Quick tests mean that after the applied field value has been changed, the VSM begins taking measurements of the magnetic moment

immediately, so there is a chance that the domains have not finished aligning when it begins this measurement. Accurate tests are at the other extreme, leaving ample time for the magnetic domains to align after the applied field value has been changed. The benefit of quick measurements is that they are, indeed, quite quick, while the disadvantage of accurate measurements is that they are lengthy. For the purposes of our experiments, we elected to use the "normal," test speed setting, so that we could balance accuracy and time consistently for all of our measurements. Figure 7.2 below shows a comparison of the quick, normal and accurate test speeds for the same sample.

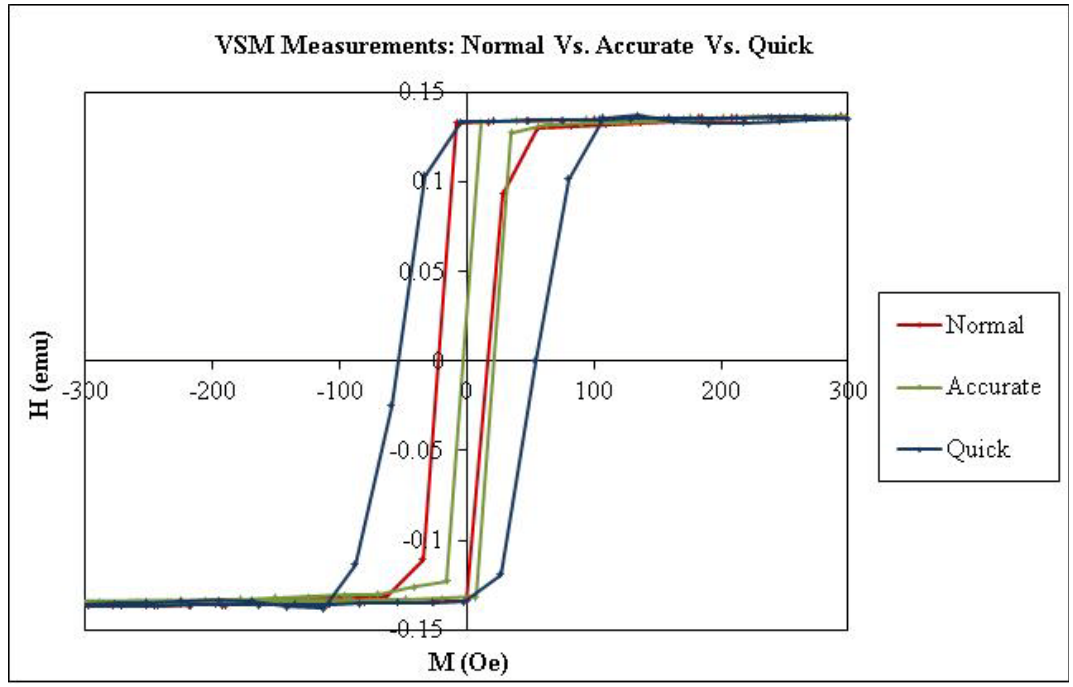

Figure 7.2: Quick versus Normal versus Accurate VSM Measurements

In order to obtain a measurement of the saturation magnetization of a sample, we set the maximum field to the apparatus's maximum available value of 7,000 Oersteds. Using a lower field may or may not fully align the magnetic domains within a material,

so by choosing the maximum field to be the largest available we can insure that the domains in the sample are all aligned. The number of measurement points is split evenly between these maximum field values. However, in regions near the origin of the hysteresis curve, we would like to have a clearer, more detailed idea of how the sample is behaving, so we measured our samples using a lower maximum field value of 200 Oe. It is from these measurements that the remanent magnetic moment and coercivity has been measured for each sample after each straining session.

Sample Holder Design

Our Nitinol samples had dimensions of approximately 90 mm x 21 mm x0.225 mm. However, when testing samples in the VSM, they are most often cut to a smaller size that fits between the inductions coils of the VSM apparatus (typically not larger than a square centimeter). However, a sample this small cannot be strained using the Instron 5566 materials tester. For this reason the straining of the 121007 sample (and the other samples in that particular set of experiments) was done by the bending method described above. However, it is difficult to provide the same strain across the whole sample area with the bending method, so we decided to develop a method of measuring our samples in the VSM that would preserve their dimensions, so the straining could be carefully controlled using the Instron 5566 materials tester. To do this, we had to develop a sample holder that would allow our complete Nitinol samples to be measured in the VSM.

The sample holders for the VSM connect to the apparatus by means of a long plastic rod that the sample holder screws on to. Although our Nitinol samples will fit between the induction coils of the VSM, screwing the sample holder to the apparatus was

impossible. However, one of the sample holders included with the VSM apparatus was designed for measuring samples of magnetic powders, and was equipped with a cavity (for the powdered sample) and a cap. We modified this sample holder by super-gluing the cap to a cut glass microscope slide. The Nitinol sample was mounted to the glass of this modified sample holder using rubber cement. After the sample holder rod was attached to the VSM apparatus, the cap (with attached glass and mounted sample) could be pressed into place. After the sample and modified sample holder were mounted in the VSM system, the location of the film was optimized in the same fashion as detailed above. Although the Nitinol sample was considerably larger than the recommended size (0.5 cm^2), the magnetic films were only deposited at the center of the substrate, confining the magnetizable region to an area of 2.1 cm x 1.6 cm or 3.36 cm^2.

Initially, two different sample holders of glass microscope slides were cut. One was roughly the same size as the area expected covered by the film, and the other was very nearly the length of the Nitinol sample. Both sample holders are pictured in Figure 7.3. Each sample holder was tested with nothing attached, with a bare strip of Nitinol of the same dimension as our samples, and with an unstrained sample (121809). The best linear fit to the data was found using Microsoft Excel, which we used to subtract from the data for sputtered Nitinol samples. Figure 7.4 shows the data for (a) the long glass sample holder and (b) the short glass sample holder as measured with a bare (unsputtered) Nitinol sample. The linear regression line and its mathematical expression are also shown on these graphs. It is obvious that the slope of the best-fit line for the short sample holder data is negative, while the slope for the best-fit line for the long sample holder is positive.

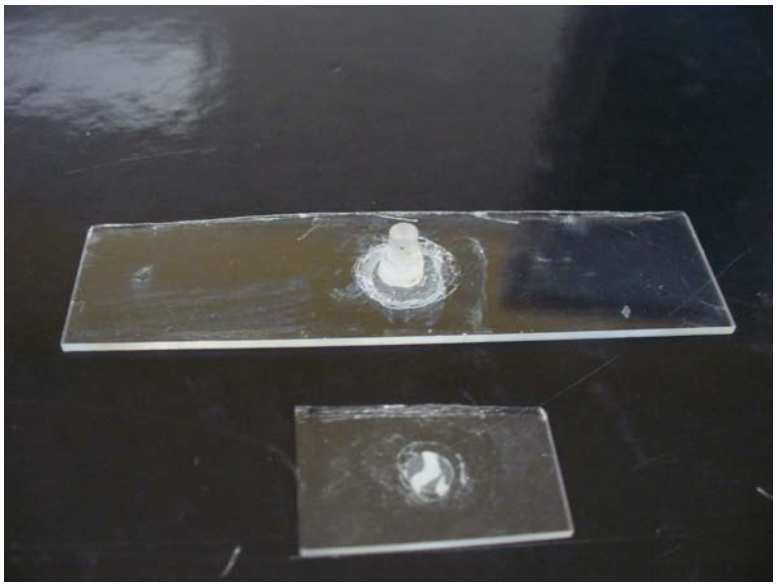

Figure 7.3: Glass Sample Holders

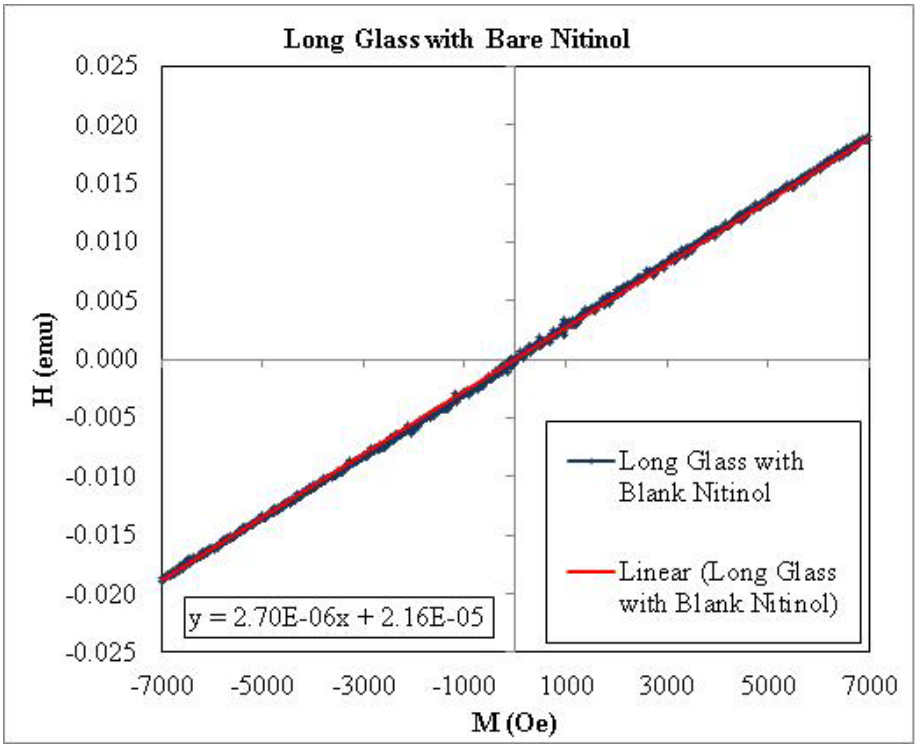

Figure 7.4a: Long Glass Sample Holder and Bare Nitinol Sheet Metal

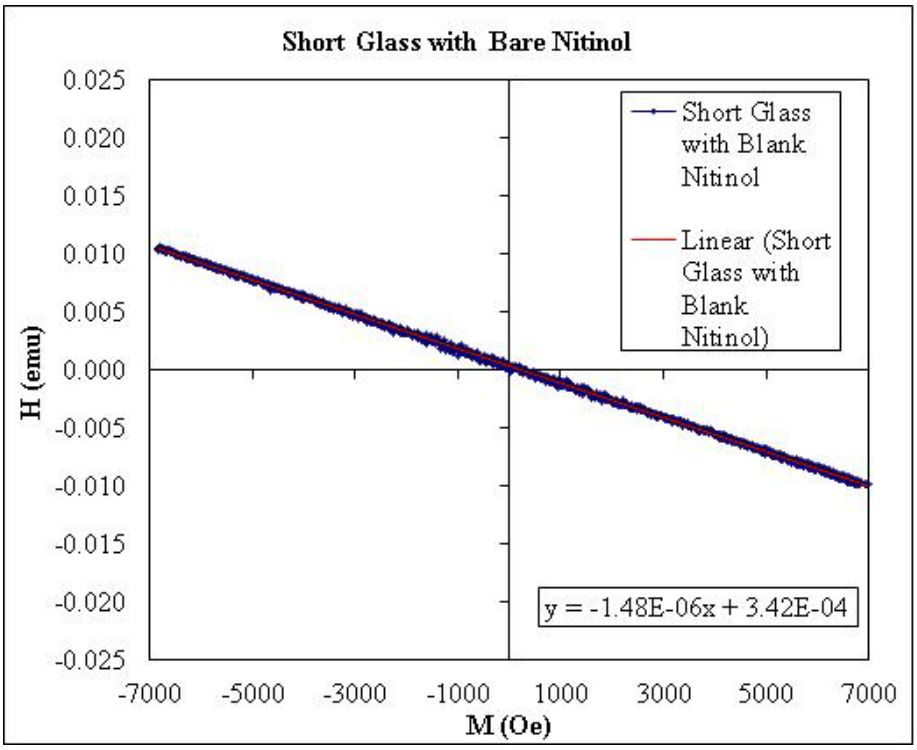

Figure 7.4b: Short Glass Sample Holder and Bare Nitinol Sheet Metal

After determining a baseline measurement for each sample holder and bare Nitinol, we measured one of our samples to see how the subtraction of this baseline affected our results. We measured the 121809 sample first with the short sample holder, and then with the long sample holder. In Figure 6.6a below, the results of subtracting the long sample holder from our data are shown - clearly the subtraction of the short sample holder information does not level the data entirely. Figure 6.6b shows the data obtained for the 121809 sample as measured with the long sample holder, as well as the adjusted data. It is clear that the information provided by the measurement of the long sample holder is more readily and accurately adjusted than that of the short sample holder.

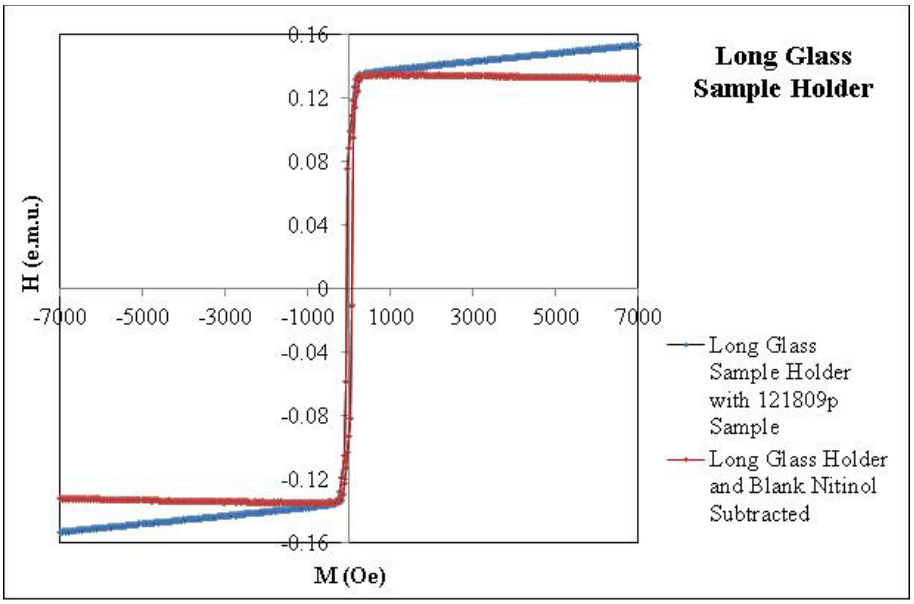

Figure 7.5a: Coated Nitinol Sample on Long Glass Sample Holder

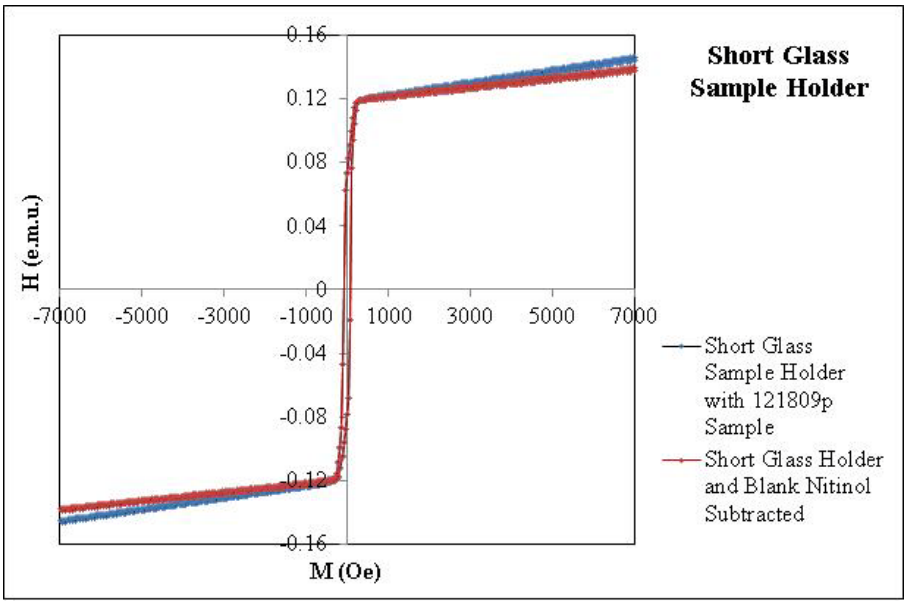

Figure 7.5b: Coated Nitinol Sample on Short Glass Sample Holder

As the sample is being vibrated continuously while being measured in the VSM, the unsupported ends are free to move more dramatically. Given the analysis of the short and long sample holders, it is apparent that the movement of the ends of the sample cannot be accounted for with the short sample holder. It is for this reason that the long sample holder was chosen for these experiments.

Finally, the variation from the center of the sample holder could possibly affect the measurement of the films, especially as the deposition of "extra" film at the ends of the Nitinol substrates was possible. To understand how the measurement of the film's magnetic properties is related to its position in regard to the VSM's pickup coils, two small pieces of sputtered Nitinol with roughly the same surface area were measured in various positions on the long sample holder. The two pieces were placed at evenly spaced intervals from the center of the sample holder and measurements from the center to the ends were made as illustrated in Figure 7.6. The figures that follow show how the coercivity (Figure 7.7), and the remanent magnetic moment (Figure 7.8), and the saturation magnetic moment (Figure 7.9) change as a function of distance from the center of the sample holder.

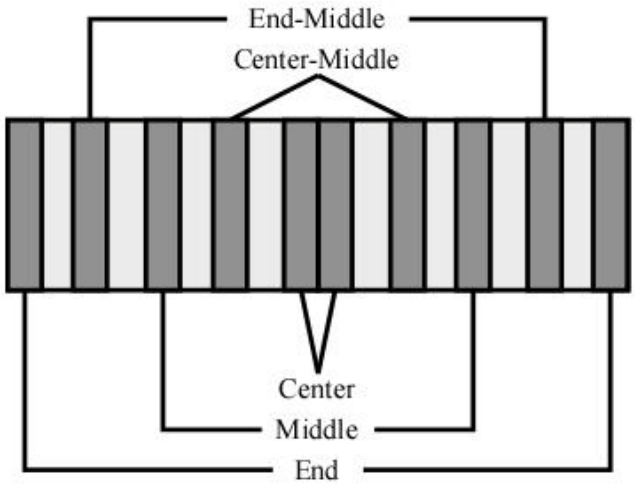

Figure 7.6: Locations of Sample Material for Sensitivity Testing

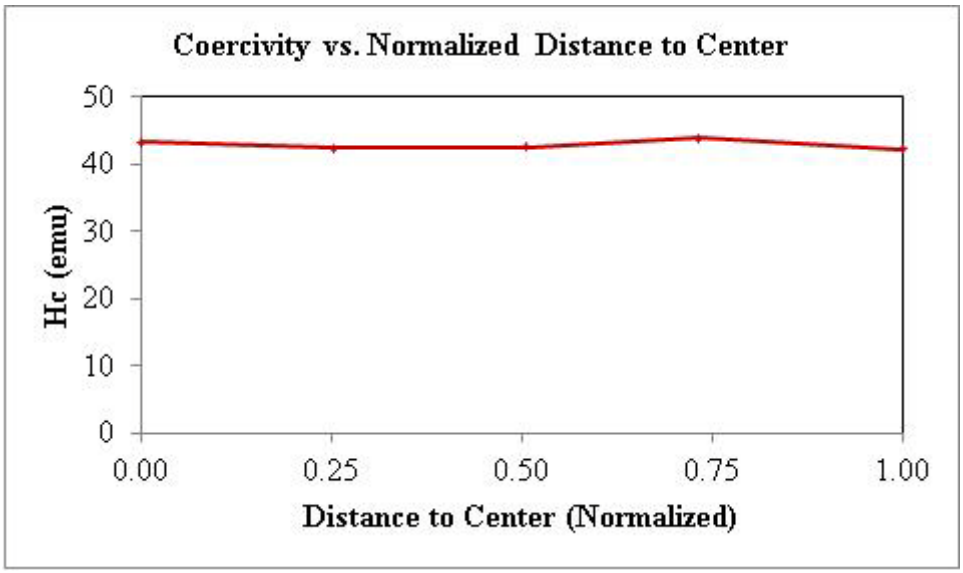

Figure 7.7: Coercivity as a Function of Distance from Center of Sample

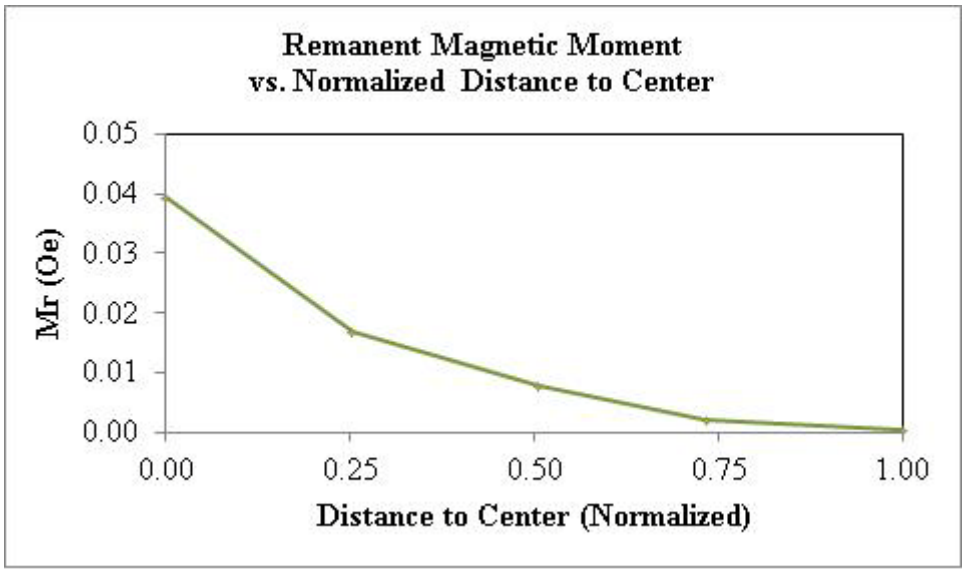

Figure 7.8: Remanent Magnetic Moment as a Function of Distance from Center of Sample

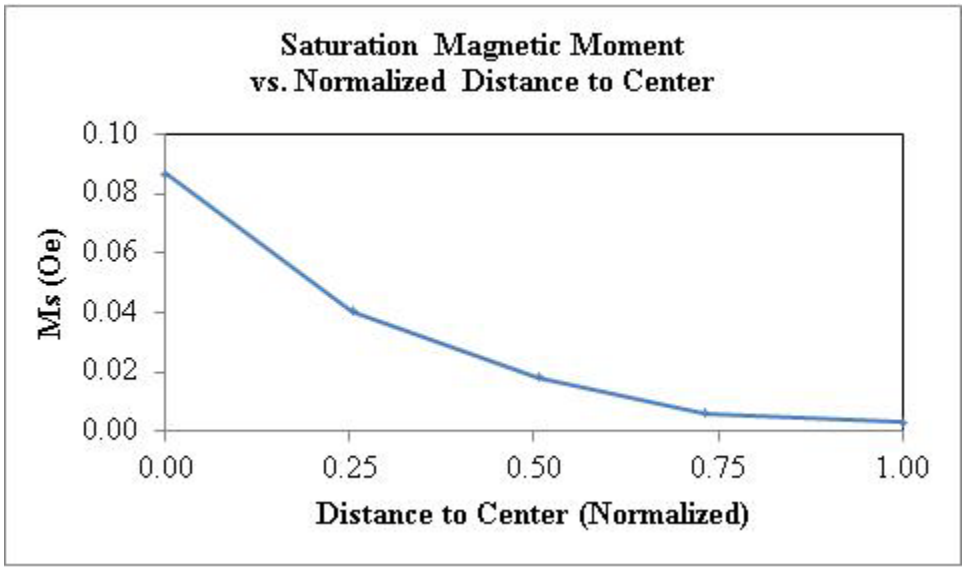

Figure 7.9: Saturation Magnetic Moment as a Function of Distance from Center of Sample

The measurement in this series of experiments is most accurate at the center (or zero) location. The coercivity appears to hardly be affected by the location of the sample on the holder. However, the saturation and the remanent magnetic moment both drop off in a strikingly similar manner as the sample pieces are positioned further from the center of the sample holder.

This data shows that the measured magnetic moments of a given sample are largest at the center of the sample holder and smallest at the edges of the sample holder. In order to understand how the sample location affects the measurement of the material's magnetic moment, a "sensitivity curve" was developed. Since the VSM is expected to take the most accurate measurements at the most centered position between the four pick-up coils, as the sample moves further from the center of the coils the accuracy of this measurement will drop off in a bell shape.

In order to examine the way position influences measurement in the VSM, we performed mathematical calculations and used MathCad to further verify these calculations. Figure 7.10 shows a simplified diagram of the sample holder in the VSM, and indicates the movement axes. The magnetic field is applied along the z-axis, and the sample is vibrated along the y-axis. The x-axis is directed across the sample surface, perpendicular to the applied magnetic field.

If the magnetic sample material is assumed to have only a net magnetic moment, *u* in the z-direction, then it can be modeled as a magnetic point dipole situated at the origin. This magnetic dipole creates a magnetic stray field around the sample, and the value of this magnetic stray field is:[31]

$$B_z(x, y, z) = \frac{\mu_0}{4\pi} 3\mu \left[\frac{z^2 - \frac{1}{3}\left(x^2 + y^2 + z^2\right)}{\left(x^2 + y^2 + z^2\right)^{5/2}} \right]$$

Where *x*, *y*, and *z* are the coordinates denoting the position around the sample (see Figure 7.10) and the sample is considered to be centered at the origin.

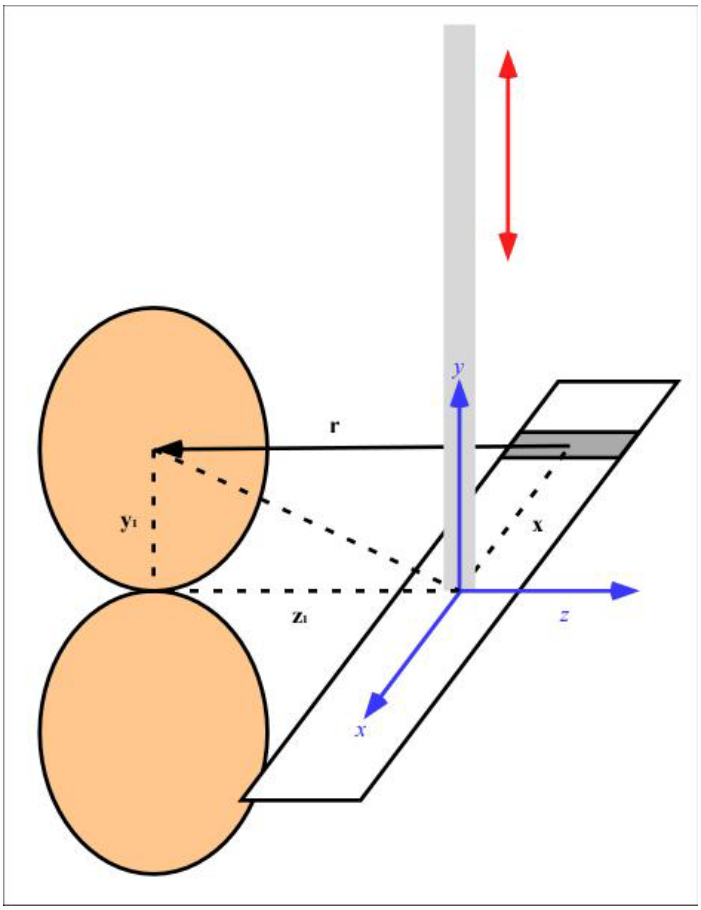

Figure 7.10: VSM Sensitivity Diagram

This diagram is not to scale.
Measurements of y_1 and z_1 were 0.013m and 0.019m respectively.

The stray field around the sample is not constant, as the sample vibrates up and down at a specified frequency. This vibration causes a variation in the flux through four pick-up coils situated in the pole pieces of the electromagnet.

The varying flux induces a current through the pick-up coils, which is proportional to the sample's magnetic moment. Because the sample is vibrating at a set frequency, this induced current varies at the same frequency. The lock-in amplifier ignores current signals that are not of the specified frequency, and acts as an amplifier with a very narrow bandwidth. In order to describe the magnetic stray field around a vibrating sample, the equation above must be modified. The location of the magnetic material is given by:

$$(x'', y'', z'') = (0, \alpha\sin\omega t, 0)$$

Where α is the vibration amplitude and ω is the vibration frequency. Including this information in the initial equation, the expression for the stray field becomes:

$$B_z(x,y,z) = \frac{\mu_0}{4\pi} 3\mu \left[\frac{z^2 - \frac{1}{3}\left(x^2 + (y - \alpha\sin\omega t)^2 + z^2\right)}{\left(x^2 + (y - \alpha\sin\omega t)^2 + z^2\right)^{5/2}} \right]$$

The flux is simply the magnetic field passing through a certain cross-sectional area, and in this case the cross-sectional area in question is that of the coils. However, the area of the coil loop varies, as the coils themselves are wound in a fashion that varies from a tiny diameter for the inner-most coils to a larger diameter for the outer coils. Additionally, the pick-up coils have some thickness that we are unable to measure as they are set into the frame of the VSM. These calculations are somewhat approximated

because of the geometry of the pick-up coils. Since we are simply showing that the sensitivity of the equipment is highest at the center-point between the pick-up coils and drops off rapidly as the sample becomes less centered, these approximations do not affect our goals. To this end, we estimated the cross-sectional area of the coil from the largest winding. The magnetic flux can be approximated by the surface area times the field at the center of the pick-up coil. So if we assume the sample to be at (x, 0, 0) and the coil to be at (0, y_1, z_1), the flux through one pick-up coil will be:

$$\Phi = \left(\pi \cdot {r_{coil}}^2\right)\frac{\mu_0}{4\pi}3\mu\left[\frac{{z_1}^2 - \frac{1}{3}\left(x^2 + (y_1 - \alpha\sin\omega t)^2 + {z_1}^2\right)}{\left(x^2 + (y_1 - \alpha\sin\omega t)^2 + {z_1}^2\right)^{5/2}}\right]$$

The values for y_1 and z_1 for the VSM apparatus used in these experiments are approximately 0.013m and 0.019m respectively. Realistically, the r_{coil} value should be determined by integrating from the smallest coil's radius to the largest coil's radius, and multiplied by the depth of the coils. However, counting the number of coils or measuring their width was out of the question due to the geometry of the VSM, so this bit of information was left out of the equation. For the purposes of this approximation it is sufficient to calculate the magnetic flux through only the largest diameter pick-up coils. The induced current is proportional to the change in magnetic flux with respect to time, or:

$$i \propto \frac{d}{dt}\Phi \propto$$

$$\left(\pi \cdot {r_{coil}}^2\right)\frac{\mu_0}{4\pi}3\mu\left[\frac{\alpha\omega\cos\omega t\left(y_1 - \alpha\sin\omega t\right)}{\left(x^2 + (y_1 - \alpha\sin\omega t)^2 + {z_1}^2\right)^{5/2}}\right]\left[\frac{5{z_1}^2 - (x^2 + (y_1 - \alpha\sin\omega t)^2 + {z_1}^2)}{(x^2 + (y_1 - \alpha\sin\omega t)^2 + {z_1}^2)}\right]$$

Since α is very small compared to y_1, the ($y_1 - \alpha \sin \omega t$) terms are approximately equivalent to y_1, so:

$$i \propto \frac{d}{dt}\Phi \propto \left(\pi \cdot r_{coil}{}^2\right)\frac{\mu_0}{4\pi}3\mu\left[\frac{y_1 \cdot \alpha\omega\cos\omega t}{(x^2 + y_1{}^2 + z_1{}^2)^{5/2}}\right]\left[\frac{5z_1{}^2 - (x^2 + y_1{}^2 + z_1{}^2)}{(x^2 + y_1{}^2 + z_1{}^2)}\right]$$

The lock-in amplifier measures the amplitude of the signal, so the equation becomes:

$$i \propto \frac{d}{dt}\Phi \propto \left\{\left(\pi \cdot r_{coil}{}^2\right)\frac{\mu_0}{4\pi}3\mu \cdot \alpha\omega\right\}\left[\frac{y_1 \cdot \left[5z_1{}^2 - (x^2 + y_1{}^2 + z_1{}^2)\right]}{\left(x^2 + y_1{}^2 + z_1{}^2\right)^{7/2}}\right]$$

The portion of the equation enclosed in the curly brackets is a constant, and it is clear that the behavior of this equation is dependent only on the portion that is enclosed by the square brackets. We may express $\left\{\left(\pi \cdot r_{coil}{}^2\right)\frac{\mu_0}{4\pi}3\mu \cdot \alpha\omega\right\}$ as a constant C, as shown in the expression below.

$$i \propto \frac{d}{dt}\Phi \propto C\left[\frac{y_1 \cdot \left[5z^2 - (x^2 + y_1{}^2 + z_1{}^2)\right]}{\left(x^2 + y_1{}^2 + z_1{}^2\right)^{7/2}}\right]$$

It is clear that this expression is dependent only upon the x-position of the sample material. When this expression is plotted as a function of the x-position, a very clear bell-shaped curve is produced, which is precisely what we expected to see. As the x-position gets larger – or as the sample material moves away from the center-point between the pick-up coils – the amount of current induced gets smaller, which causes the measured magnetic moment to be significantly reduced from its actual value.

The bell shaped curve of the measured magnetic moment, or the "sensitivity curve," shows that the parts of the film in the center on the sample contribute to the measurement signal the most.

Background Measurements

Once the sample holder had been selected, it was measured with a piece of bare Nitinol of the same dimensions as the sputtered samples. The slope through the hysteresis curve was determined by the curve fitting routine of Microsoft Excel and this offset was subtracted from all raw measurement data.

Determining Film Thickness

Although Appendix A details the generalized procedure for calculating the thickness of a thin film sample with four sides using the measurement of its magnetic moment, the particular details of how the film thickness is calculated works on any arbitrary sample. In addition to accurately determining the area of the film, it is also important to determine a value for the saturation magnetization of the material itself. For the different iron-silicon concentrations used in these samples, as well as the nickel iron permalloy, the saturation magnetization information was taken from Ferromagnetism by Richard M. Bozorth, a standard text on the magnetic properties of various materials. [ ]

To calculate the film's surface area in these experiments, a technical graphics program called Canvas was used. After uploading a photograph of the sample and a reference object of known area, the image of the reference object was selected and its surface area calculated by Canvas. By comparing this calculated area to the known value, a conversion factor may be determined. Canvas's selection tool to could then be

used to highlight the area covered by the film, its virtual area calculated, then converted into the actual film area, which could be used to determine the film thickness, as detailed in Appendix A.

Thickness Variation

The substrate materials are attached to a circular substrate holder, which rotates during deposition. In order to create reproducible results, it is important to deposit a film of uniform thickness on the surface of our substrates. In order to determine whether there is a variation in film thickness in the DIBS system, a two-inch silicon wafer was placed on the DIBS sample holder so that it covered the center of the substrate holder and extended to the edge, as illustrated in Figure 7.11. After deposition, the wafer was cut as marked with dotted lines in the illustration, so that measurements could be taken from a portion of the wafer that extended radially from the center of the substrate holder to its edge.

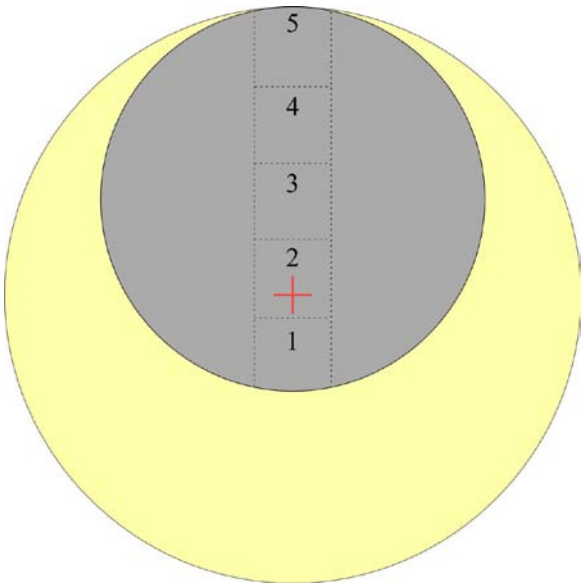

Figure 7.11: Silicon Wafer Orientation for Thickness Variation - DIBS

Each of the small silicon pieces (numbered 1 through 5), were measured in the Vibrating Sample Magnetometer (VSM) to determine their saturation magnetic moment. Each piece was subjected to thickness measurements as mentioned in the previous section, and the results of these thickness calculations are related in Table 7.2.

In order to sputter films of uniform thickness, the sample holders in both the DIBS and the magnetron sputtering systems rotate while sputtering takes place. We can see clearly from the data above that the thicknesses resulting from the DIBS are all approximately equal. In fact, the film thicknesses vary on average by approximately ±3%.

Table 7.2: Thickness Variation - DIBS

Location	1	2	3	4	5 – Edge
Thickness (nm)	36.76	39.59	41.20	39.63	39.32

The magnetron sputtering system's substrate holder also rotates during deposition, but no experimental data was taken for this project to determine a base-line thickness distribution in this system. However, the system specifications suggest that film thickness over a 3" wafer are expected to be less than 2%. The magnetron sputtering system improves on the thickness variation by using a confocal arrangement of sputtering sources which focus the incident beam of film material more precisely onto the surface of the substrates. [24, 25]

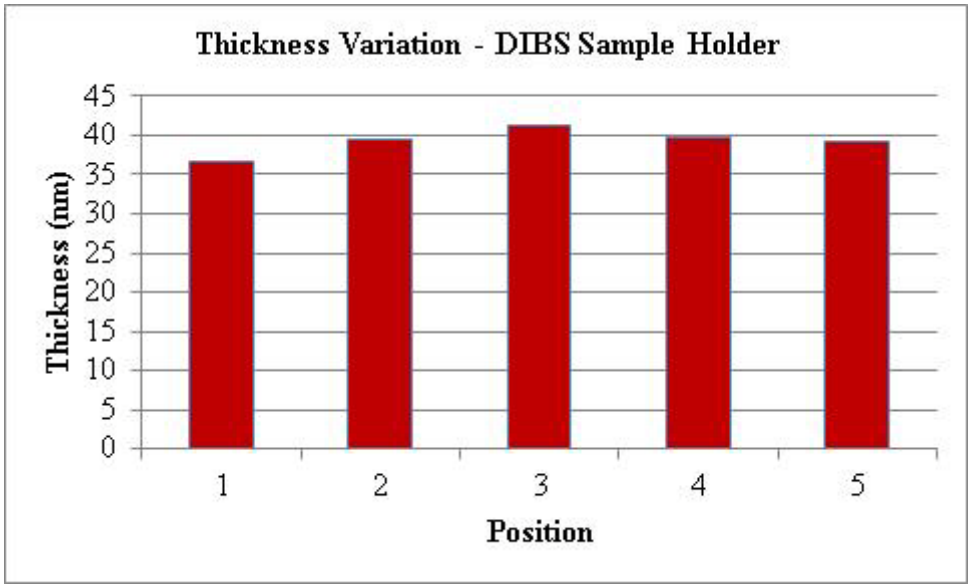

Figure 7.12: Thickness Variation - DIBS

PART III:

MEASUREMENT RESULTS AND CONCLUSIONS

CHAPTER VIII: RESULTS

In this chapter I shall present the results of my measurements. Data from straining, optical microscope photographs, as well as VSM measurements will be reviewed for each individual sample. Comparisons between this data will be made in the Interpretations chapter. Table 8.1 lists the samples whose data is detailed in the following pages.

Table 8.1: Sample Overview

Name	121007	121809	062410	070810
Composition	FeSi at. 0.5%	FeSi at. 0.5%	NiFe at. 20%	FeSi at. 3%
Estimated Thickness (nm)	320	120	960	110
Deposition Method	DIBS	DIBS	Magnetron	Magnetron
Strain Method	Bending	Lateral	Lateral	Lateral

Although only four samples are related in this particular discussion, over the course of this research numerous experiments were performed and a very large quantity of data was collected. Organizing this data in a meaningful way is challenging, so by presenting each sample individually and each set of data in the order that it was collected one can become familiar with each sample in the same way as the experimenter.

Sample 121007

This sample was grown in DIBS system, using a FeSi target with 0.5% at. Si. This sample was strained via bending over a cylinder (as detailed in Appendix B). The data regarding this sample is presented in order to compare bending to lateral straining, but is only a review. Although optical photographs of this sample were not taken over the course of the straining experiments, a microscopy study of the bent samples did not show any induced defects in the film. Additionally, since the sample was bent over rigid cylinders of known radii by hand, no stress-strain plots were generated. After each bending strain the magnetic properties were measured, and are summarized in Table 8.2.

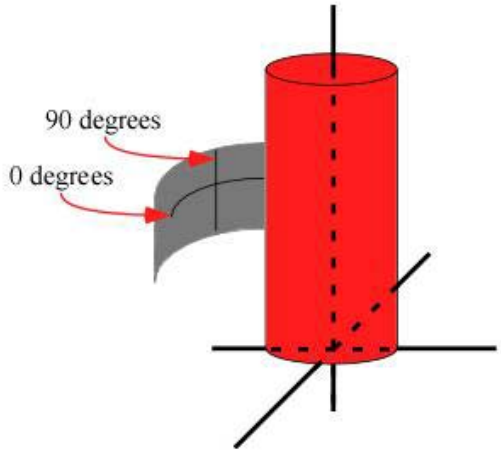

Figure 8.1: VSM Orientation for Bending Strain

Table 8.2: VSM Measurements – 121007 Sample

0 degree Orientation				
Strain	**Hc (Oe)**	**Mr (emu)**	**Ms (emu)**	**Mr/Ms**
0%	17.849	0.0063	0.00792	0.79485
0.5%	14.904	0.00596	0.00779	0.76574
1%	14.804	0.00592	0.00783	0.75552
1.5%	16.175	0.00615	0.00786	0.78187
2%	20.783	0.00681	0.0079	0.86133
3%	22.35	0.007	0.00798	0.87669
4%	28.838	0.00683	0.00772	0.8842
"Two Step" Effect				
3%	48.7	0.00412	-	-
4%	59.21	0.004415	-	-

(a.) 0 degree Orientation

90 degree Orientation				
Strain	**Hc (Oe)**	**Mr (emu)**	**Ms (emu)**	**Mr/Ms**
0%	13.646	0.00542	0.00848	0.63909
0.5%	10.96	0.00502	0.00834	0.60132
1%	11.035	0.00456	0.0084	0.54366
1.5%	10.608	0.00479	0.00843	0.56762
2%	12.047	0.00388	0.00832	0.46645
3%	11.834	0.00362	0.00806	0.44991
4%	13.277	0.00296	0.00783	0.37764

(b.) 90 degree Orientation

Each measured magnetic characteristic was plotted against the amount of bending strain applied and is discussed below. Additionally, each of these bent samples was

measured both perpendicular to the straining axis (0 degrees) and parallel to the straining axis (90 degrees) after each straining session.

The “two step” dual coercivity and dual remanence effects are pronounced in the 0 degree oriented sample. The 90 degree sample fails to demonstrate any “two step” behavior, and instead the hysteresis curve shears in the horizontal direction.

The coercivity decreases between 0% and 1% strain, then begins increasing dramatically after 1.5% strain is applied in the 0 degree orientation. In the 90 degree orientation the coercivity remains approximately the same regardless of the strain applied.

The remanent magnetic moment of the 0 degree Oriented sample behaves similarly to the coercivity in this direction, in that that it decreases between 0% and 1% strain, then increases at strains greater than 1.5%. In the 90 degree orientation, the remanent magnetic moment does not mimic the coercivity, and instead decreases approximately steadily as more strain is applied.

The saturation magnetic moment for both the 0 degree and the 90 degree samples stays approximately the same regardless of the bending strain applied. This makes sense, as there were no transformation fronts or film loss was observed during these experiments. None of the thin film detached from the Nitinol substrate during these bending experiments, even when a maximum calculated strain greater than 4% was applied. These results suggests that (1) there was strong adhesion between the thin film and the Nitinol substrate; or (2) bending the Nitinol sheet metal over a cylinder created a homogeneous strain in the thin film on surface of the Nitinol. An extensive literature

search did not provide insight in what happens when Nitinol sheet metal is bent over a cylinder. Strain-stress relations of bent Nitinol sheet metal is a current subject of study by others. [28]

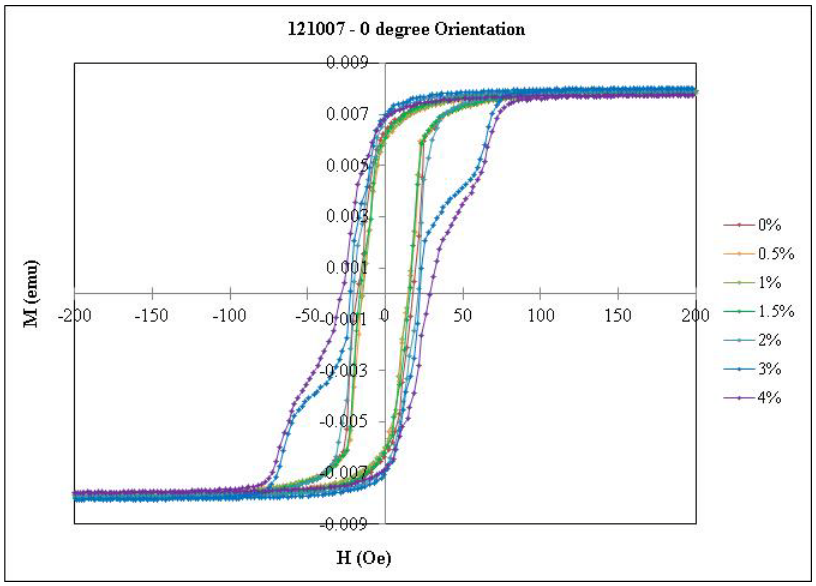

(a.) 0 degree Orientation

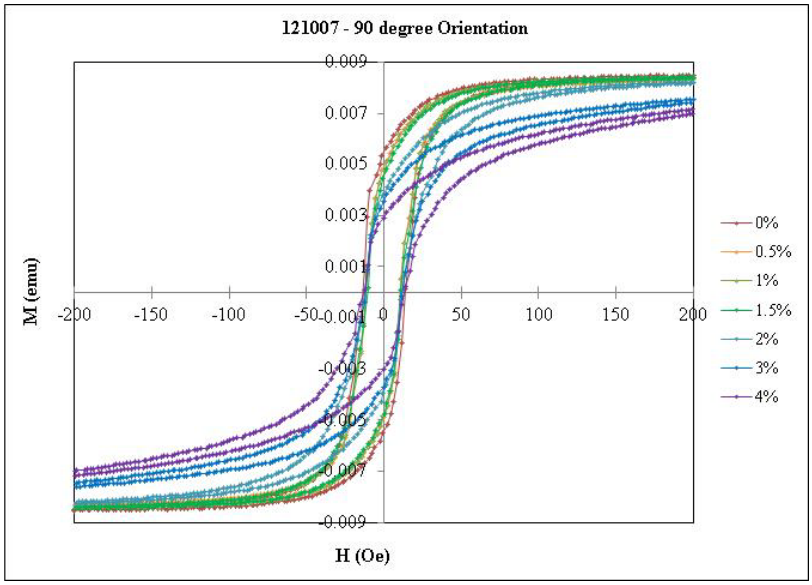

(b.) 90 degree Orientation

Figure 8.2: VSM Hysteresis Curves – 121007 Sample

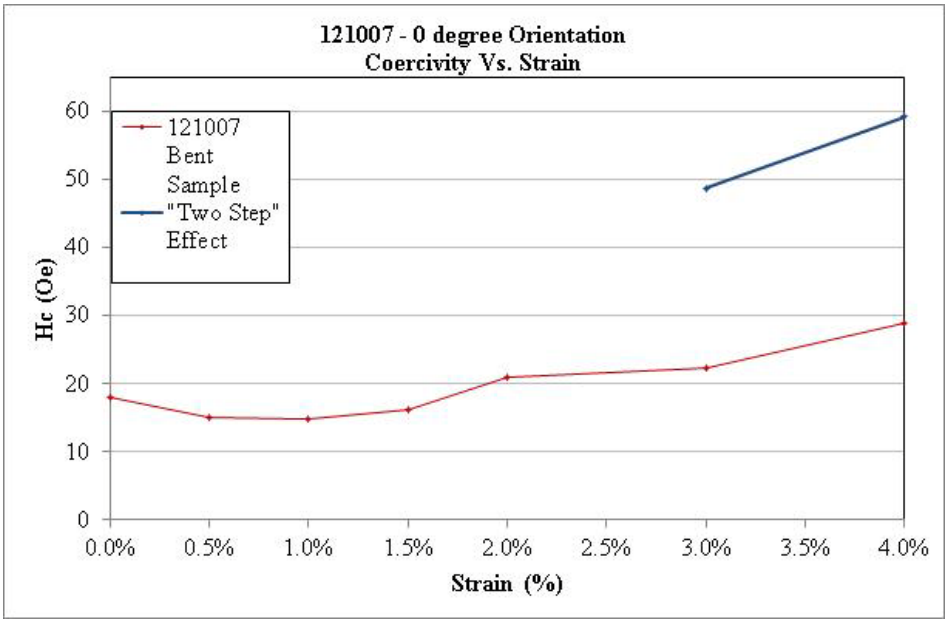

(a.)

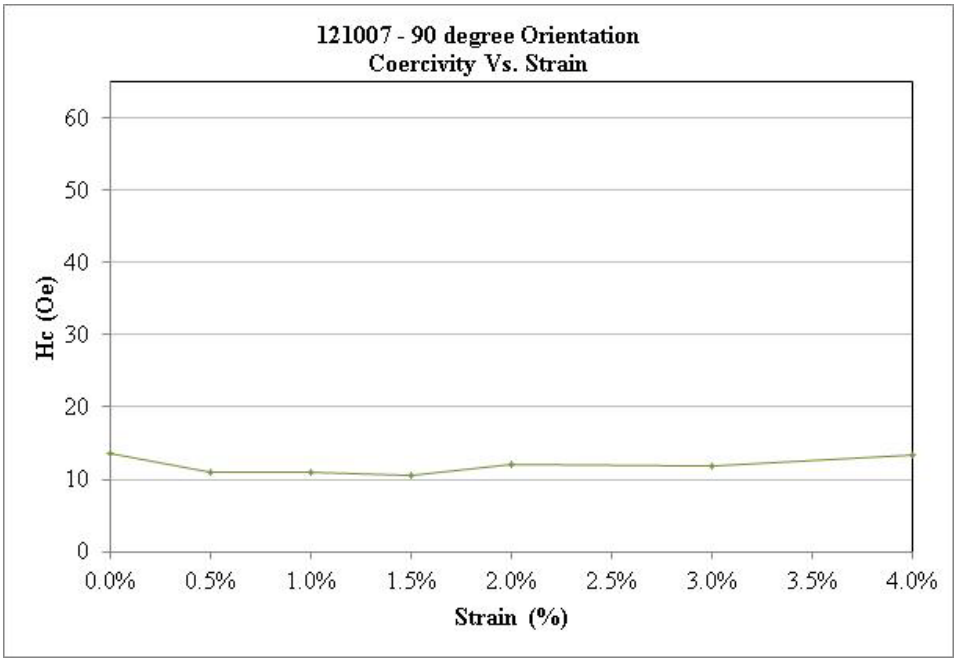

(b.)

Figure 8.3: Coercivity Vs. Strain – 121007 Sample

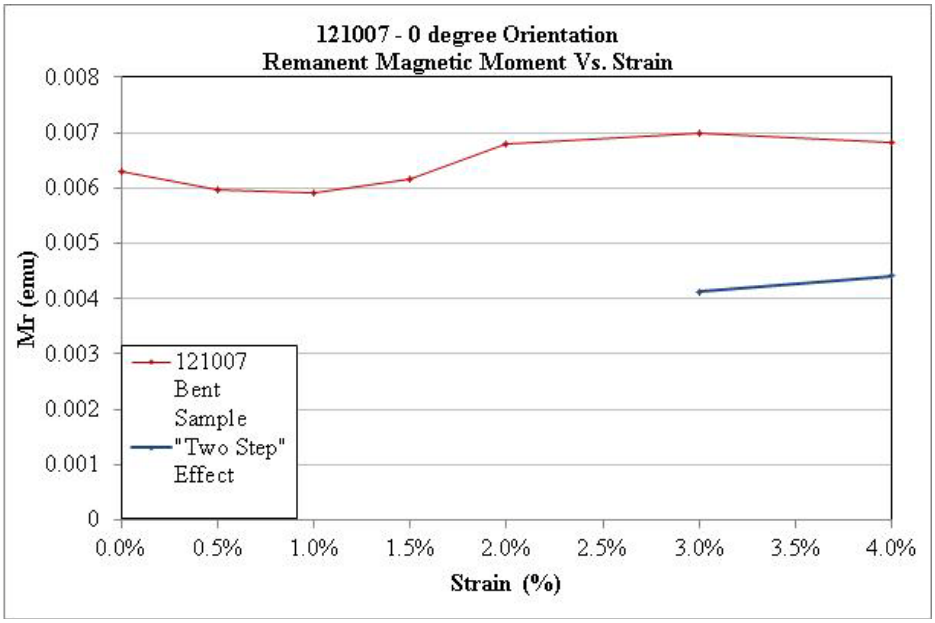

(a.)

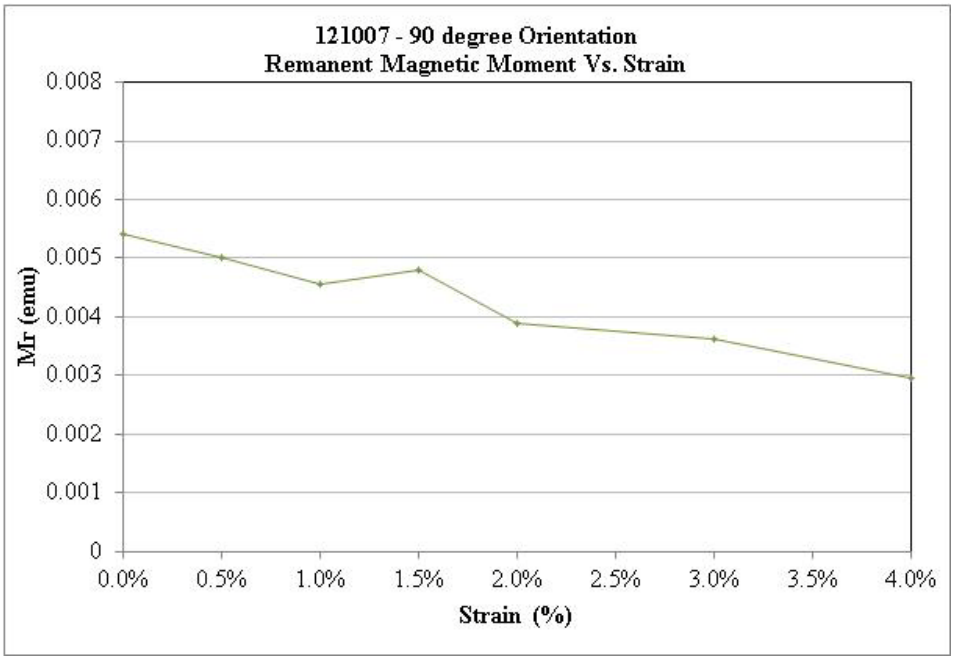

(b.)

Figure 8.4: Remanent Magnetic Moment Vs. Strain – 121007 Sample

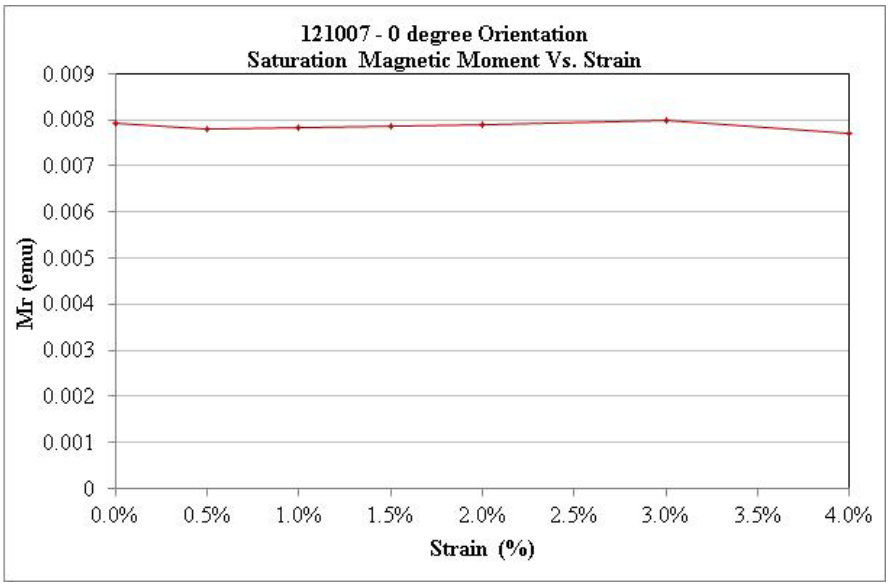

(a.)

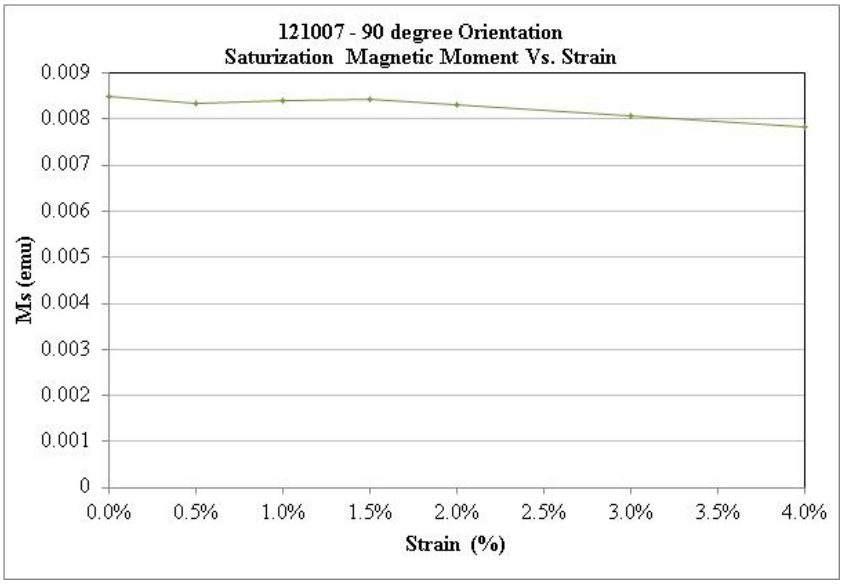

(b.)

Figure 8.5: Saturization Magnetic Moment Vs. Strain – 121007 Sample

Sample 121809

This sample was made using the DIBS system, and the film on the Nitinol substrate is curved due to the glass and silicon wafer "mask" covering a portion of it during deposition. This film is formed of FeSi at. 0.5%, meaning there is 0.5% atomic percentage silicon for every 99.5% atomic percentage of iron.

Preliminary experiments suggested that the AVE strain could be estimated from the net tensile strain, these experiments were performed on bare Nitinol without film. However, the crosshead-AVE strain relationship does not hold when there is a film present on the Nitinol. For this reason, we strained this sample according to our observations during the preliminary experiments, then began increasing the tensile strain in steps of 0.5% until the sample had experienced at least 5% strain. In the end, because of the unpredictability of the AVE strain, this sample was subjected to a maximum of 6.25% AVE strain. The Tension and Compression combination of methods was also tested on this sample, after it had undergone up to 6.25% straining using the Tension Profiler method.

The figure below (Figure 8.6) shows the strain-stress curves for a strain rate of less than 2mm/min. This rate believed to be low enough to keep the temperature increases near the transformation fronts low enough so that the propagation stress is less than the nucleation stress, $\sigma_{pm}<\sigma_{nm}$ as expressed in Figure 5.2. Because the propagation stress is lower than the nucleation stress, the transformation site moves through the Nitinol material, and additional transformation sites are not formed. Up to approximately 1% strain the stress-strain relation does not show a lot of hysteresis. For higher strain

values hysteresis is observed with a loading plateau at 400 MPascal and an unloading plateau between 150 and 200 MPascal. The lump in the stress-strain curve immediately before the loading plateau corresponds to the nucleation of a Austenite to Martensite phase transformation. The stress-strain relation is non-linear even below 1% AVE strain. The average observed Young's modulus for AVE strains smaller than 1% is approximately 44 GPascal. The Young's modulus at zero AVE strain determined from the tangent at the origin is approximately 77 GPascal. This stress-strain data shows that once the film reaches approximately 1%, the amount of force being applied to the sample does not increase much as the strain continues to increase.

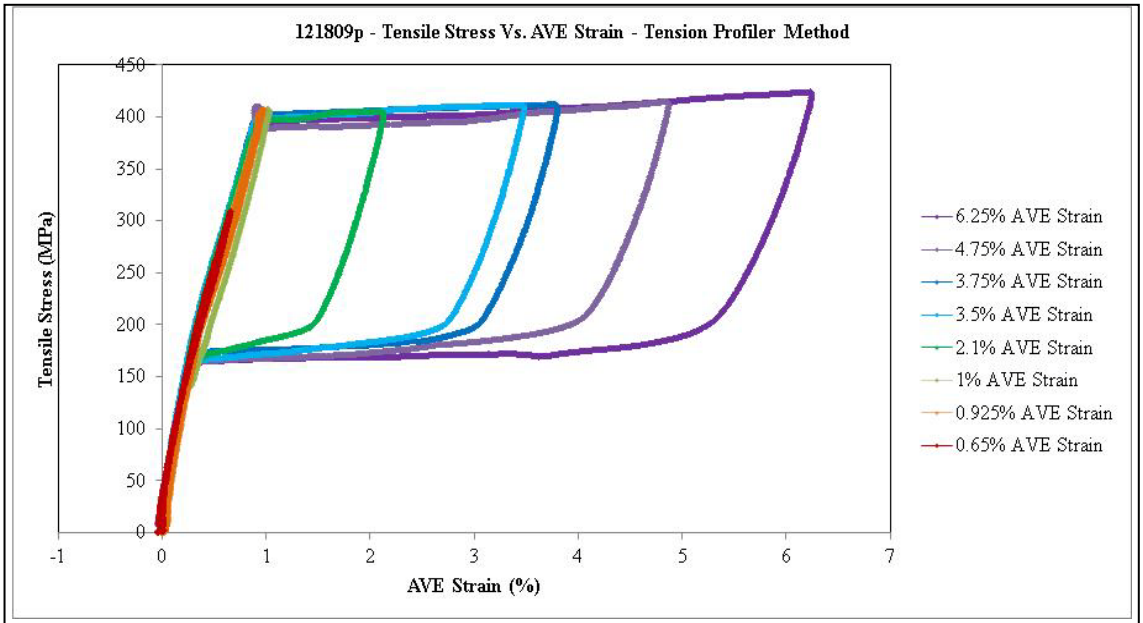

Figure 8.6: Tensile Stress Vs. AVE Strain – 121809 Sample

Additionally, optical microscopy was not done on this sample after each straining session, and was instead performed after all strain tests has been completed. Because of

this, the selection of optical microscope photos is limited to the most interesting features observed in the strained film. These photographs are listed in order of increasing magnification, from 5x (Figure 8.7) to 20x (Figure 8.8). After straining up to 6.25% AVE strain the sample contained small blisters that were visible by optical microscopy. The thin film detached from the substrate at the location of some of these blisters.

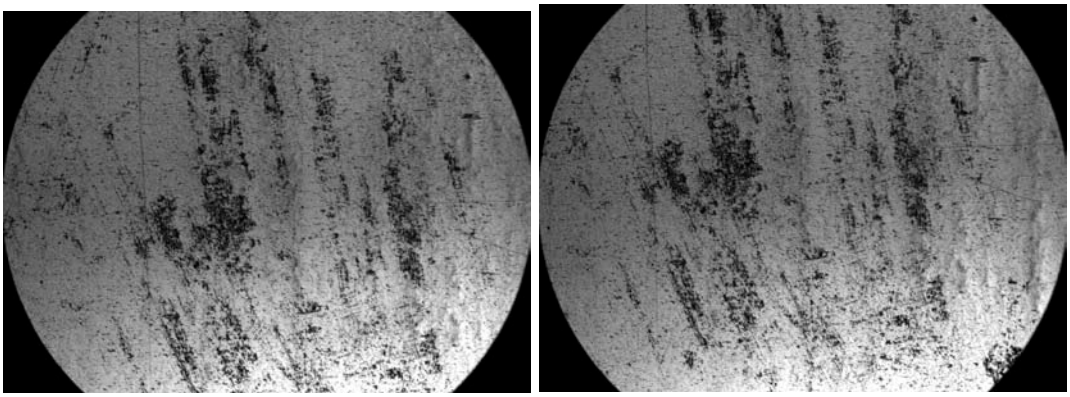

(a.) Blisters on film surface at 5x magnification

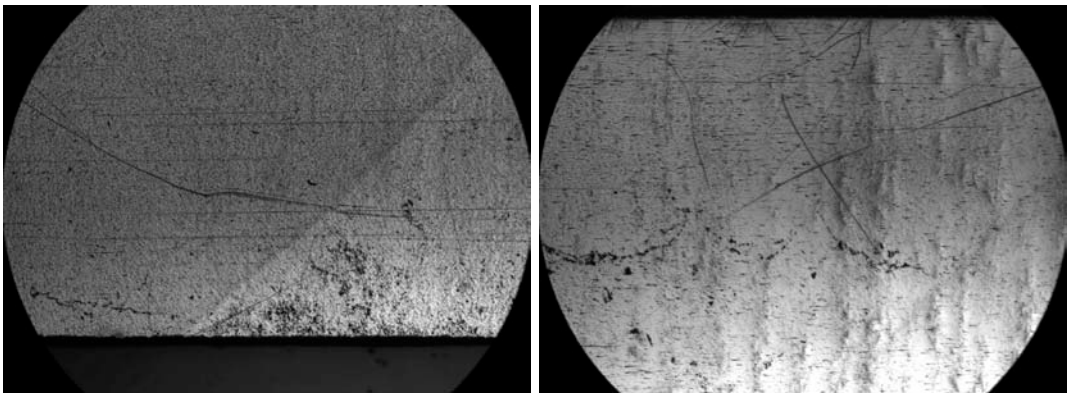

(b.) Film edge at 5x magnification

Figure 8.7: Optical Microscopy Photographs - 121809 Sample

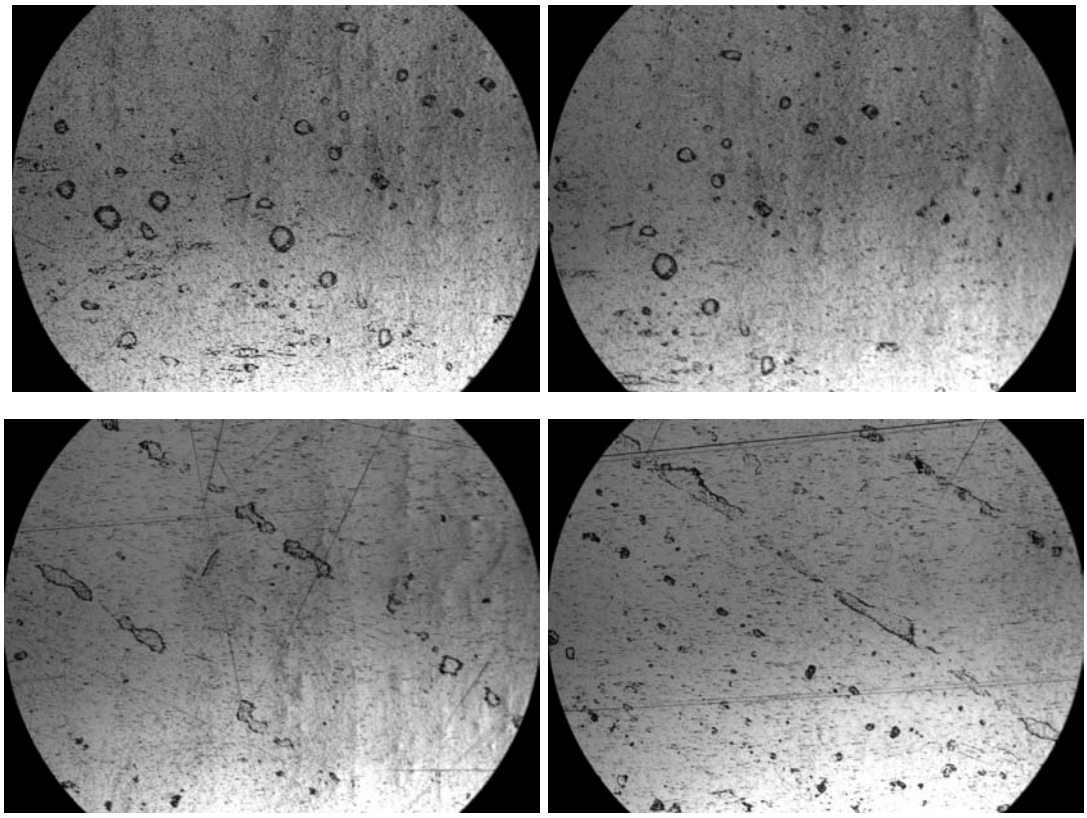

Figure 8.8: Optical Microscopy Photographs – 121809 – Blisters on Film Surface at 20x Magnification

One of the unique things about this sample is that, like with the bent 121007 sample, a dual coercivity is observed after straining the sample beyond 3.75% AVE strain. The straining seems to cause plastic deformation in the film and change the coercivity of the sample drastically. The VSM hysteresis curves are measured perpendicular to the strain direction after various strain cycles are shown in Figure 8.9 below. The measurement data suggests that once the thin film is exposed to the large strain associated with the production of the Martensite phase in the Nitinol substrate,

plastic deformation is introduced into the film and its coercivity begins to rapidly decrease.

This “Two-Step” effect is observed starting at 3.75% AVE strain and becomes more pronounced as the amount of strain on the sample increases. This is consistent with the 121007 samples, as they exhibited dual remanent magnetic moments and coercivities in the 3% and 4% strain range. The secondary step-coercivity and step-remanent magnetic moment are included in the magnetic characteristics table for this sample (Table 8.3), and have been plotted versus the strain as well.

Table 8.3: VSM Measurements – 121809 Sample

AVE Strain	Hc (Oe)	Mr (emu)	Ms (emu)	Mr/Ms
0%	50.72	0.0857	0.1341	0.6393
0.65%	70.165	0.0866	0.1321	0.6553
0.925%	59.675	0.1010	0.1329	0.7596
1.0%	60.443	0.1056	0.1347	0.7842
2.1%	63.375	0.1086	0.1346	0.8065
3.5%	54.353	0.1160	0.1365	0.8494
3.75%	57.275	0.0571	0.1353	0.423
4.75%	57.865	0.0778	0.1356	0.5739
6.25%	55.025	0.1260	0.1369	0.9205
“Two Step” Effect				
3.75%	14.685	0.1160	-	-
4.75%	14.360	0.1214	-	-
6.25%	13.060	0.1328	-	-

The coercivity, remanent magnetic moment and the saturation magnetic moment, and the remanent to saturation magnetic moment ratio have each been plotted in the

figures below. It is clear that as the amount of strain increases the coercivity increases initially (between 0 and 0.65% strain) and then begins decreasing. In the "two step" range (between 3.75% and 6.25% strain), the second coercivity value is also decreasing. However, if these two values were combined, the overall coercivity would be roughly as large as the greatest coercivity value for the original curve (a value of 70.165 emu at 0.65% strain). The VSM curve suggests that part of the magnetic film has lowered its coercivity significantly after each successive strain cycle, or in other words, the quantity of high coercivity material decreases while the amount of low coercivity material increases after each straining cycle. This is consistent with an inhomogeneous strain in the Nitinol substrate, assuming that the high coercivity material is the non-deformed film, and the low-coercivity material is the deformed thin film material on top of the portion of Nitinol that transformed to the Martensite phase during the strain cycle. The 6.25% VSM curve suggests that 95% of the substrate transformed to the Martensite phase, and thus 95% of the thin film was plastically deformed.

The remanent magnetic moment varies only slightly until it reaches 3.75% strain, when the dual remanent magnetic moments are observed. The main remanent magnetic moment value drops off at this point, then begins to increase as additional strain is applied. Likewise, the two-step remanent magnetic moment value increases steadily as more strain is applied to the sample. Once again, the combination of these two remanent magnetic moments is greater than the largest remanent magnetic moment measured before the "two step" effect is observed.

The hysteresis loop clearly maintains roughly the same shape up until 3.75% strain, when the loop is dramatically changed and the "two step" or dual coercivity/remanence is observed. As the strain increases further, the step moves upward (increased remanent magnetic moment) and narrows (decreased coercivity).

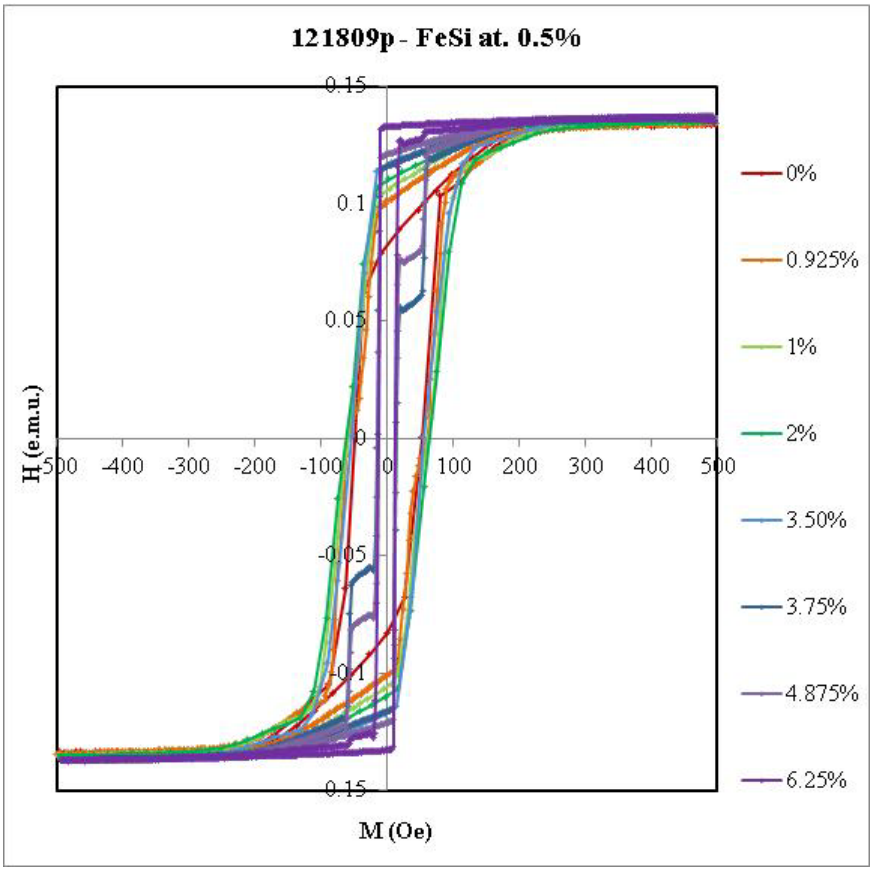

Figure 8.9: VSM Hysteresis Curves – 121809 Sample

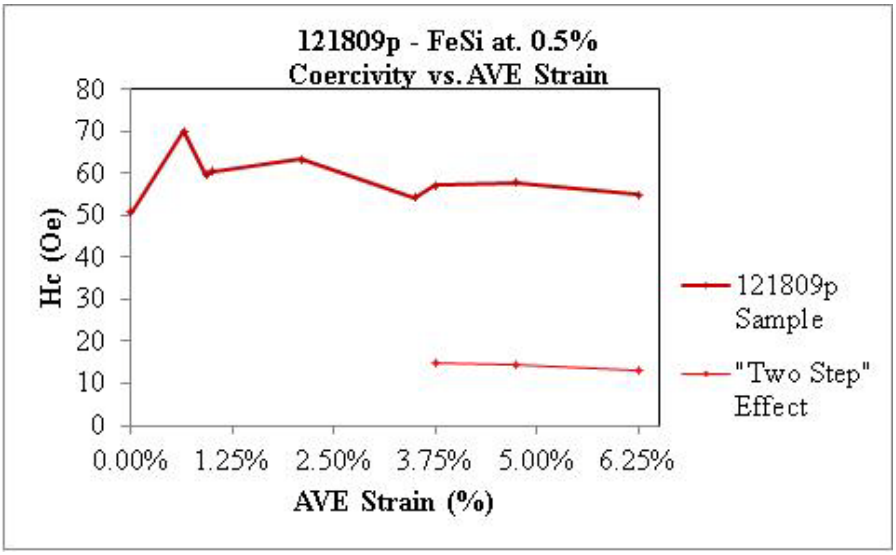

Figure 8.10: Coercivity Vs. AVE Strain – 121809 Sample

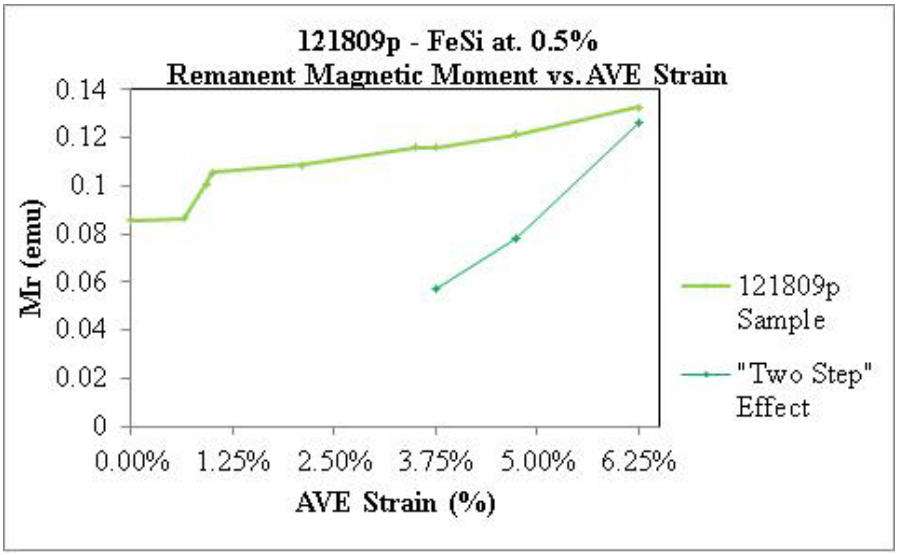

Figure 8.11: Remanent Magnetic Moment Vs. AVE Strain – 121809 Sample

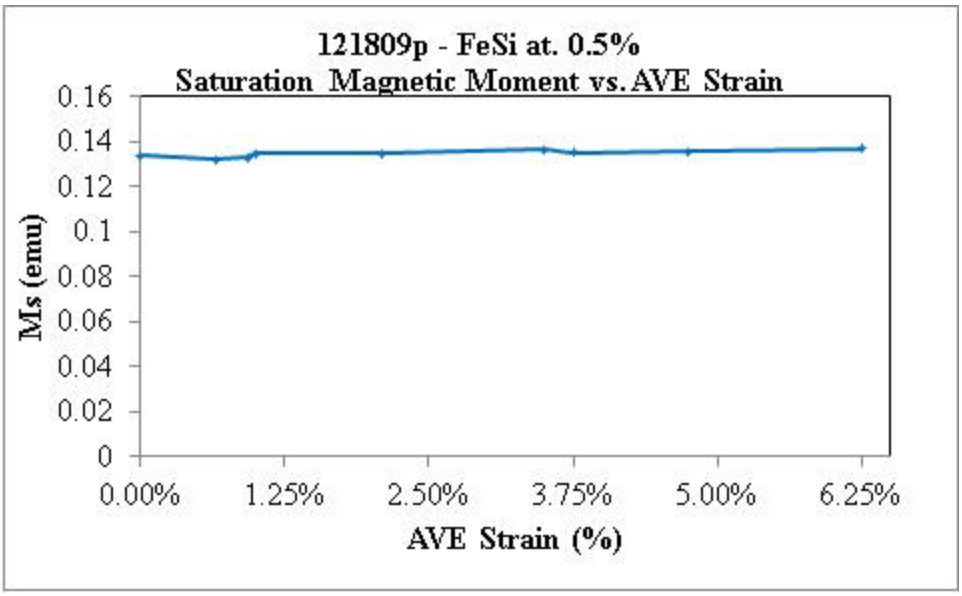

Figure 8.12: Saturization Magnetic Moment Vs. AVE Strain – 121809 Sample

Sample 062410

This sample was made using magnetron sputtering, and is composed of nickel iron permalloy. This sample was also sputtered with the thickest film of all our samples, at 962 nm. Additionally, this was the first of our samples to be tested with a combination of "tension" and "compression" tests in the Instron materials tester, so the stress-strain plots are grouped in pairs.

Although an extensive amount of optical microscope photographs were taken, identifying common locations between these photographs proved to be quite difficult. This factor led to the development of the marking/framing procedure detailed in the optical microscopy section (Chapter 6). For this reason, the number of optical

microscope photographs presented for this sample is limited to those few in which common locations could be identified, as well as the most interesting or dramatic samples of the deformations introduced by the applied stress.

The unloading data for the 1.5% strain session was corrupted, so that strain test has been excluded from the data presented here. Additionally, the 2% test was slightly different from other tests, because the sample was quite slack then the test began. For this reason, the stress-strain graph for the 2% strain trial is in parts – the light blue line indicates the strain the sample was submitted to before the test was stopped and re-started. Note that no lump is observed in the unloading curves, which suggests that at the maximum strain the Nitinol substrate was not completely transformed to the Martensitic state.

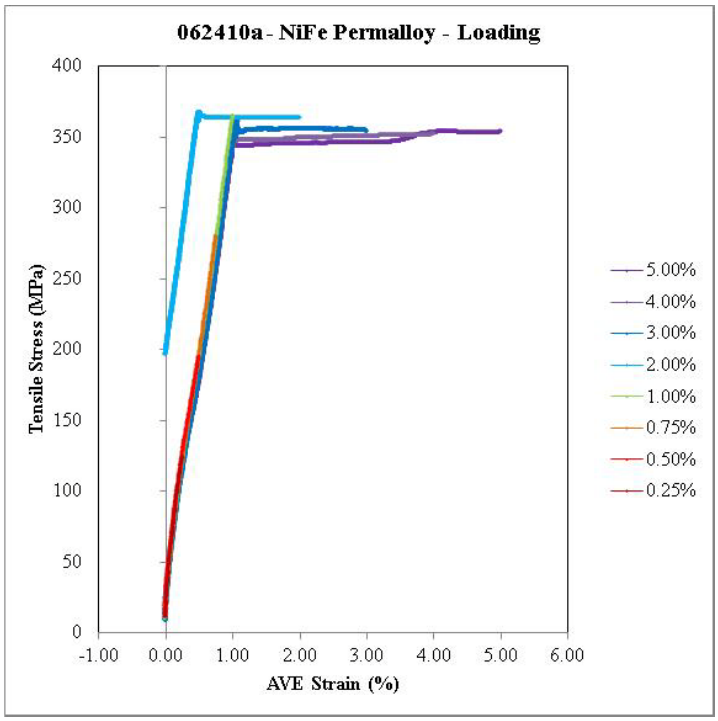

(a.) Loading

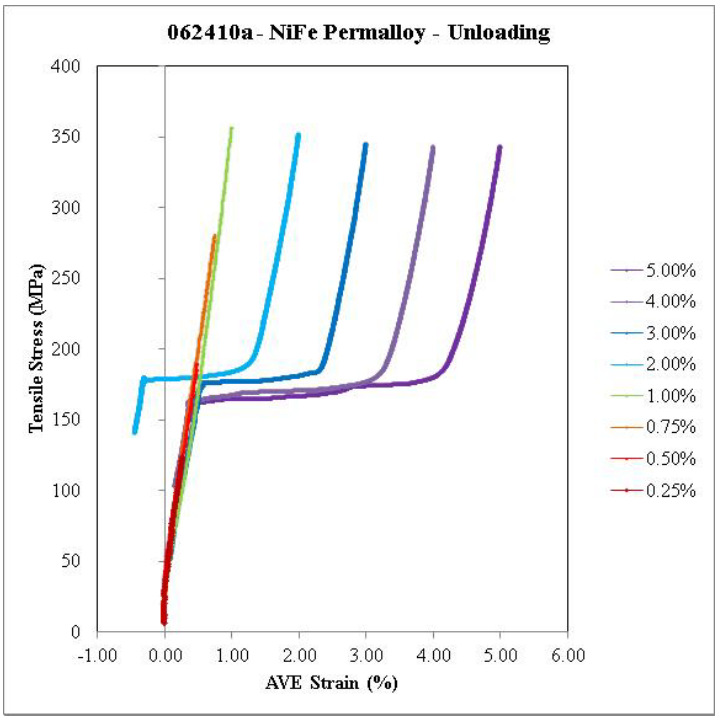

(b.) Unloading

Figure 8.13: Tensile Stress Vs. AVE Strain - 062410 Sample

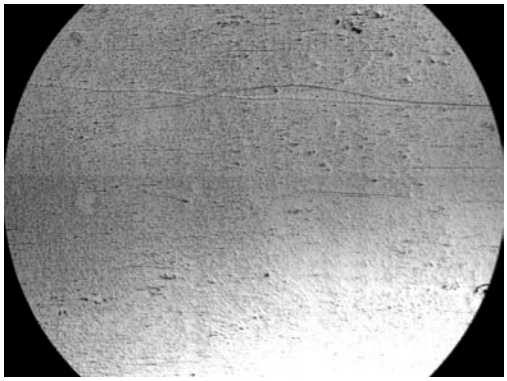

(a.) 0% strain

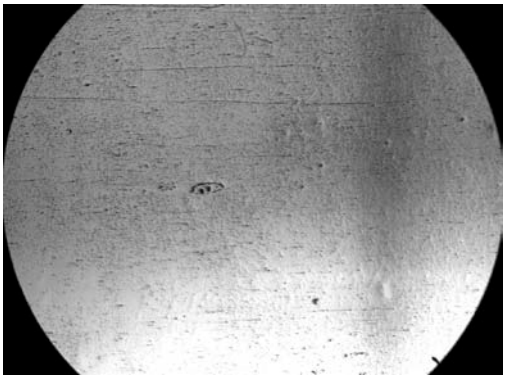

(b.) 0.5% strain

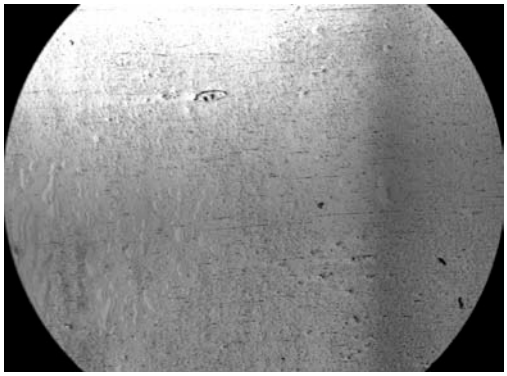

(c.) 0.75% strain

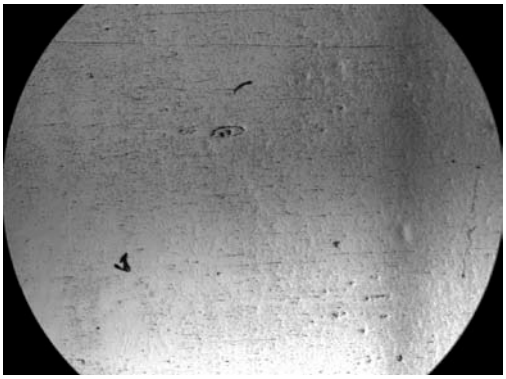

(d.) 1% strain

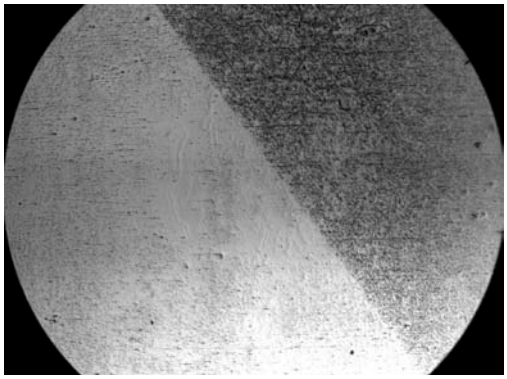

(e.) 1.5% strain

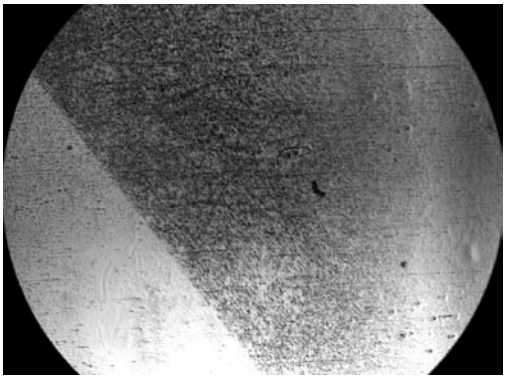

(f.) 2% Strain

Figure 8.14: Optical Microscope Photographs – 062410 Sample – 0% to 2% AVE Strain

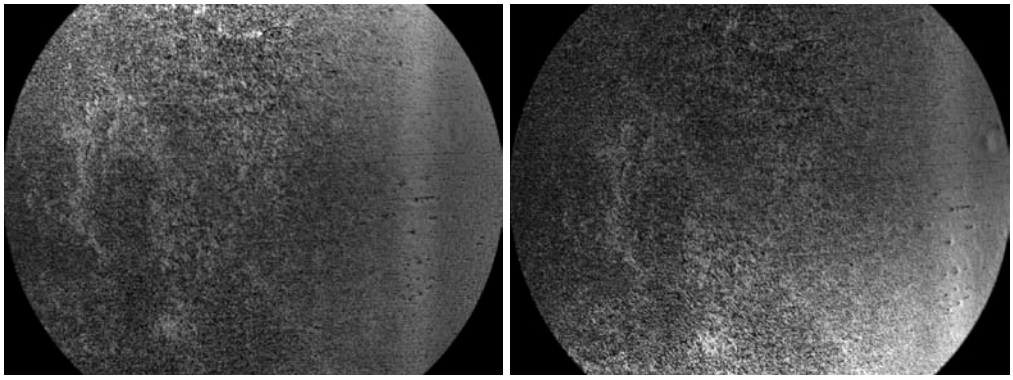

(a.) 4% strain (b.) 5% strain

Figure 8.15: Optical Microscope Photographs – 062410a Sample 4% to 5% AVE Strain

The locations where deformation has been introduced into the film are quite obvious, as is the orientation of the transformation front. The thin film on the surface of the Nitinol that had transformed to its Martensitic phase would crack and result in a visual color change of the film and allowed the deformation fronts to be tracked during deformation much more easily than would be possible on un-sputtered Nitinol. Upon careful examination, one can see that the edge of the deformation front is not entirely straight, a phenomenon that is investigated more thoroughly in the conclusions section.

The magnetic hysteresis curves were measured perpendicular to the strain axis, and are shown in figure 8.16. Table 8.4 expresses the magnetic properties measured on this sample after each successive straining test. This sample is different from the other samples we've tested because it is the thickest film, and the only sample made with permalloy. Unlike all of the other samples, this sample a significant amount of film was

easily detached from the 062410 sample using a small piece of ordinary Scotch Tape. The following series of figures expresses the coercivity, remanence, saturation magnetization and the remanence-saturation ratio as a function of strain.

Table 8.4: VSM Measurements – 062410 Sample

AVE Strain	Hc (Oe)	Mr (emu)	Ms (emu)	Mr/Ms
0%	19.5798	0.01623	0.02413	0.67249
0.25%	21.530	0.0156	0.02404	0.64891
0.5%	23.4955	0.01535	0.02333	0.65777
0.75%	22.482	0.01502	0.02311	0.64981
1.0%	19.2285	0.01429	0.02311	0.61844
1.5%	17.3765	0.01318	0.02289	0.57566
2.0%	15.4938	0.01234	0.02224	0.55470
3.0%	14.7745	0.01146	0.02130	0.53797
4.0%	14.8748	0.01119	0.02090	0.53565
5.0%	14.8893	0.01070	0.02043	0.5236

Although the coercivity initially rises as the strain increases, around 0.75% AVE strain the coercivity reaches a peak and begins declining for all successive strain applications. Both the remanent and the saturation magnetic moments decrease as strain increases.

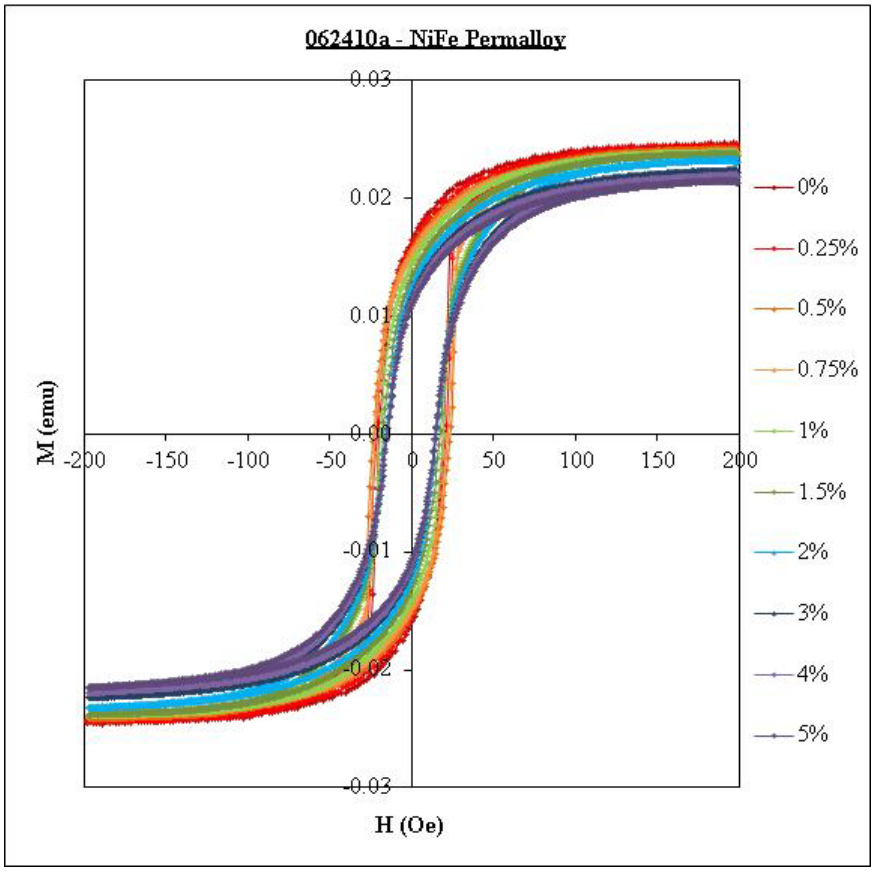

Figure 8.16: VSM Hysteresis Curves – 062410 Sample

The hysteresis loop shears as the amount of strain applied to the sample increases. Additionally, both the coercivity and the remanent magnetic moment decrease with increasing strain. Coercivity, remanent magnetic moment, and saturation magnetic moment are plotted in Figures 8.17 through 8.19 below.

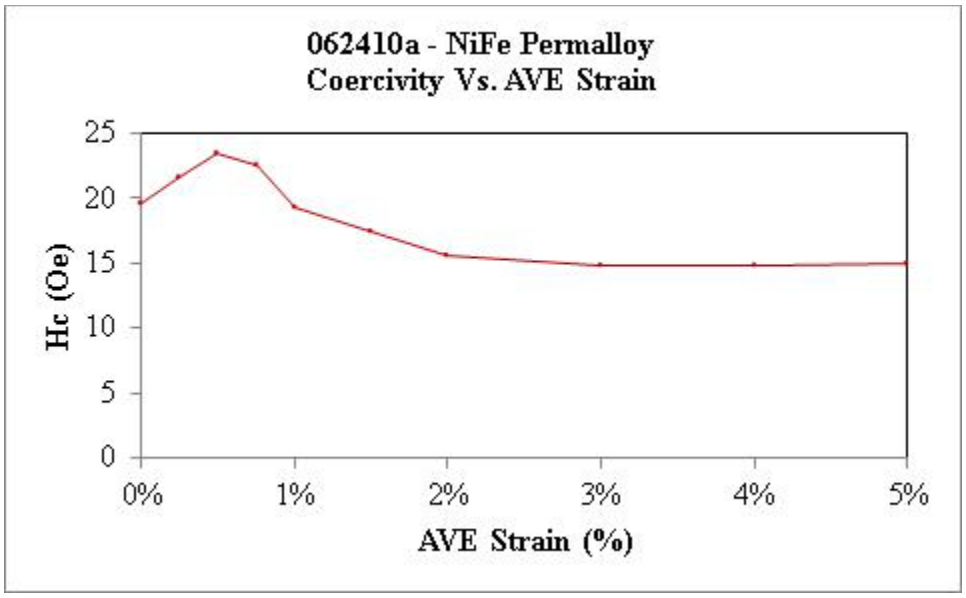

Figure 8.17: Coercivity vs. AVE Strain – 062410 Sample

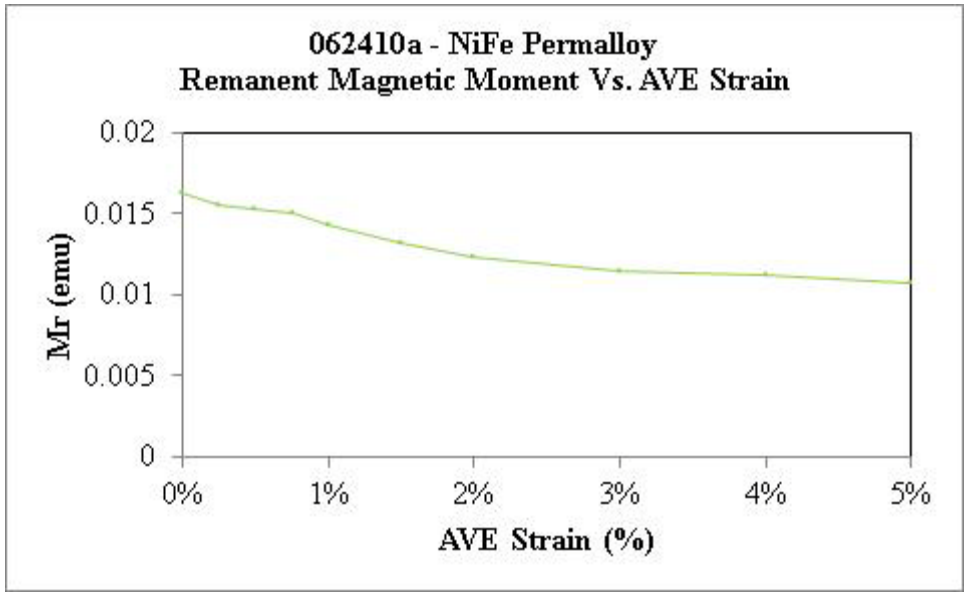

Figure 8.18: Remanent Magnetic Moment vs. AVE Strain – 062410 Sample

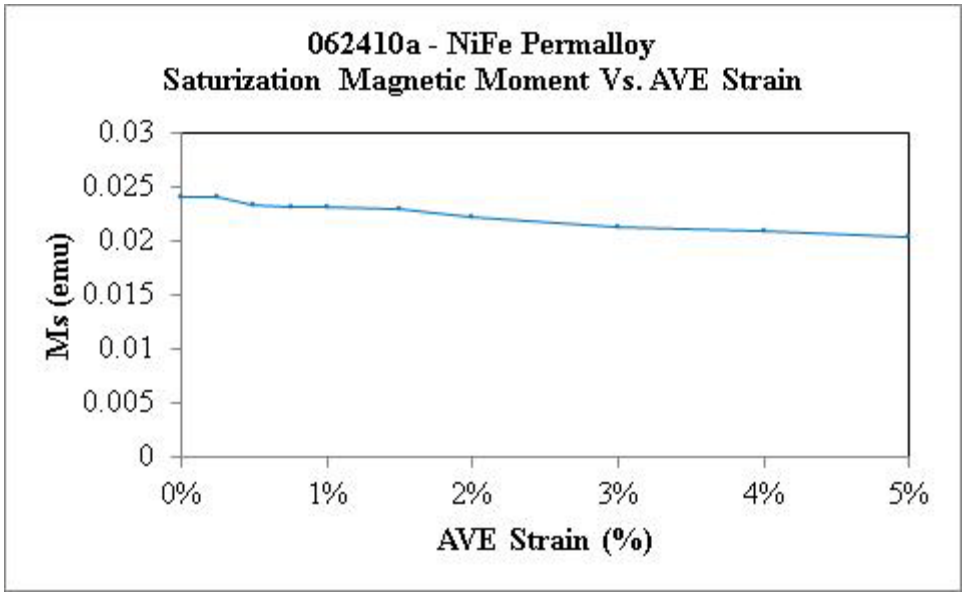

Figure 8.19: Saturization Magnetic Moment vs. AVE Strain – 062410 Sample

Sample 070810

This sample was made using magnetron sputtering, and is composed of FeSi at. 3%. Like the other samples, this sample was subjected to increasingly large amount of strains, and photographed and magnetically characterized between each successive strain.

This sample was strained using the combination of Tension and Compression methods in the Instron 5566 materials tester, and so their stress-strain plots are shown in two parts for each test (Figure 8.20). Furthermore, the optical microscope photographing procedure (which includes marking and framing the sample when taking photographs) was used with this sample. For space, only the most striking photographs that demonstrate the evolution of deformations within the film were selected to share (Figures 8.21 through 8.23).

Finally, the VSM data (again, measured perpendicular to the strain axis) is presented below as with the other samples, in Table 8.5 and Figures 8.24 through 8.27. The coercivity and saturation magnetic moment clearly decrease as the sample undergoes increasing amounts of strain, while the remanent magnetic moment stays roughly the same and only decreases slightly.

Table 8.5: VSM Measurement - 070810 Sample

AVE Strain	Hc (Oe)	Mr (emu)	Ms (emu)	Mr/Ms
0%	63.5465	0.0348	0.0707	0.4922
0.25%	63.9243	0.0356	0.0704	0.5061
0.5%	66.3060	0.0354	0.0708	0.4977
0.75%	62.9960	0.0361	0.0707	0.5105
1.0%	63.9750	0.0347	0.0695	0.4984
1.5%	63.1360	0.0348	0.0682	0.47711
2.0%	63.0700	0.0356	0.0661	0.4710
3.0%	62.2765	0.0354	0.0646	0.4957
4.0%	60.4188	0.0361	0.0617	0.4200
5.0%	59.5390	0.0347	0.0576	0.3938

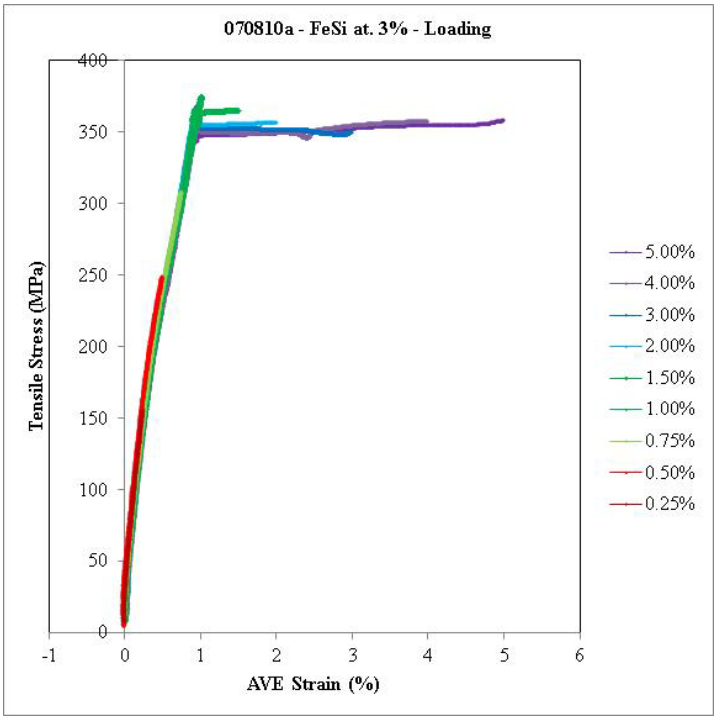

(a.) Loading

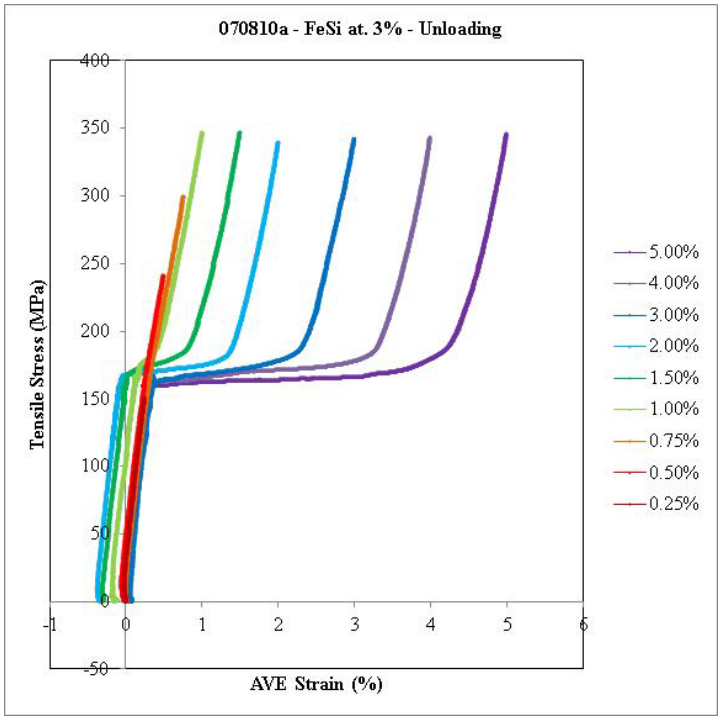

(b.) Unloading

Figure 8.20: Tensile Stress Vs. AVE Strain - 070810 Sample

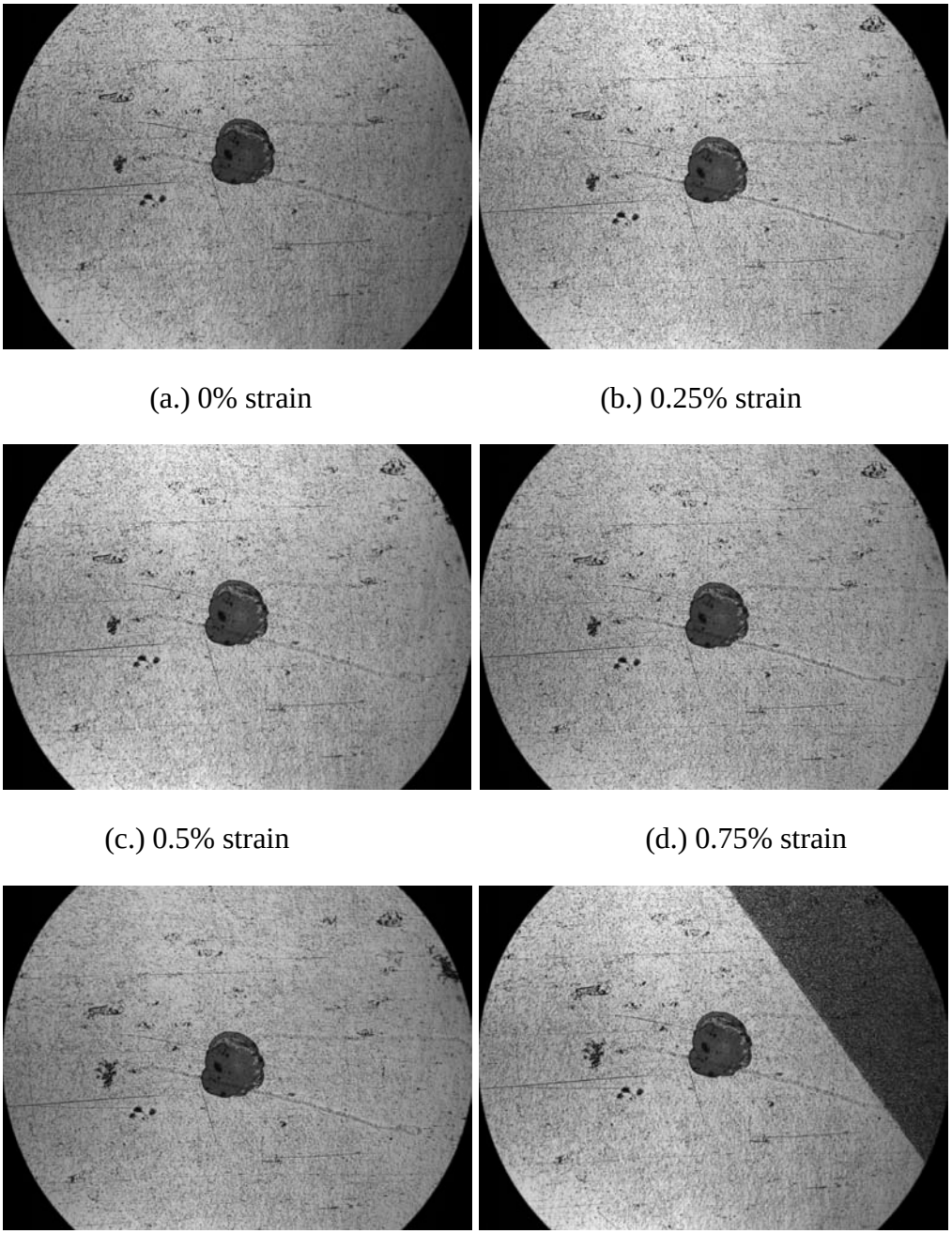

(a.) 0% strain (b.) 0.25% strain

(c.) 0.5% strain (d.) 0.75% strain

(e.) 1% strain (f.) 1.5% Strain

Figure 8.21: Optical Microscope Photographs – 070810a Sample – 0% to 1.5% AVE Strain

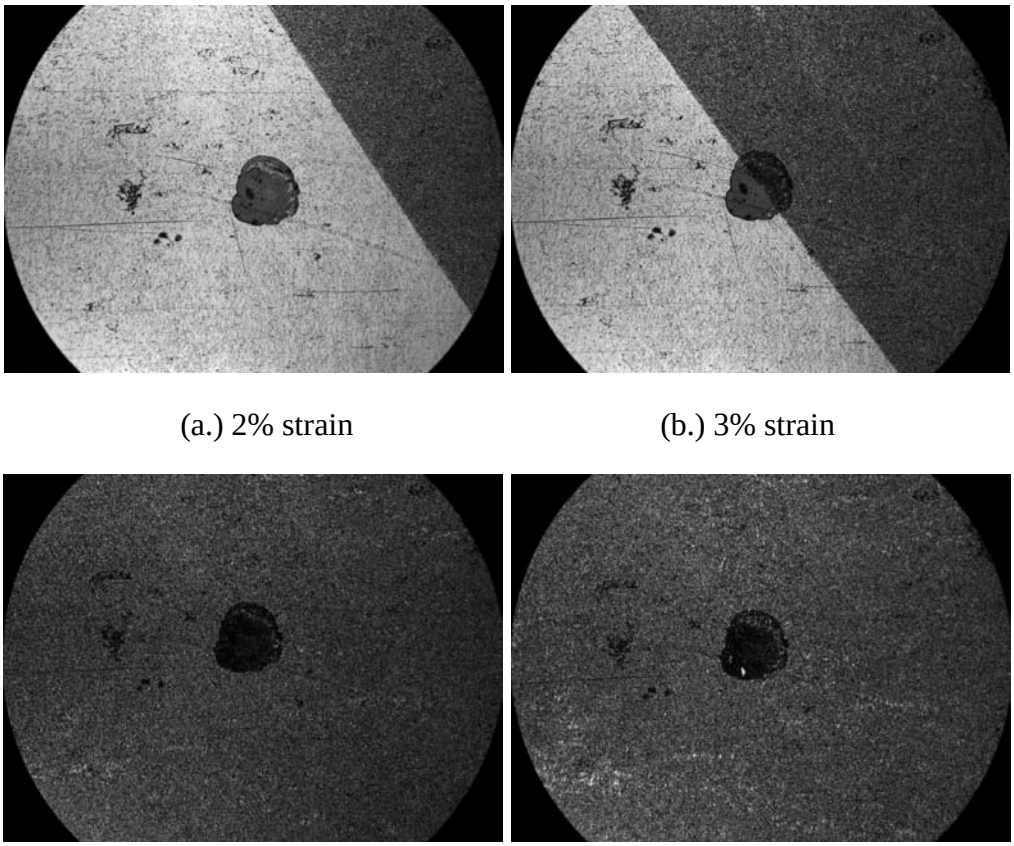

(a.) 2% strain (b.) 3% strain

(c.) 4% strain (d.) 5% strain

Figure 8.22: Optical Microscope Photographs – 070810 Sample – 2% to 5% AVE Strain

Deformation is first observed in the film after it had undergone 1% strain, although the selected photographs do not show that. These photographs were taken at the center of the film, and were chosen because they were the series that most exemplified the presence of the deformation front. After 4% and 5% strain, optical photographs at

40x were taken to illustrate the extreme deterioration of the film after being subjected to these amounts of strain.

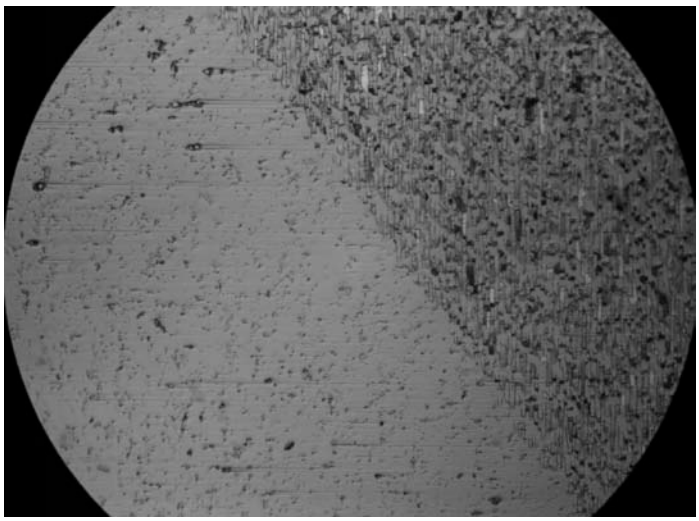

(a.) 4% AVE Strain

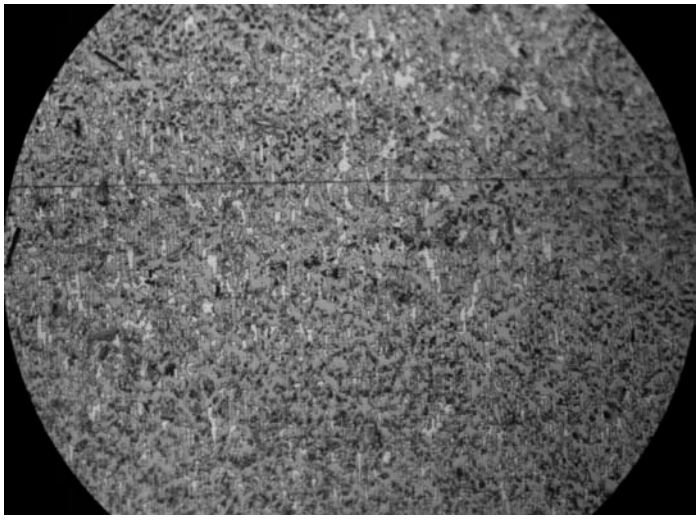

(b.) 5% AVE Strain

Figure 8.23: 20x Optical Microscope Photographs – 070810 Sample

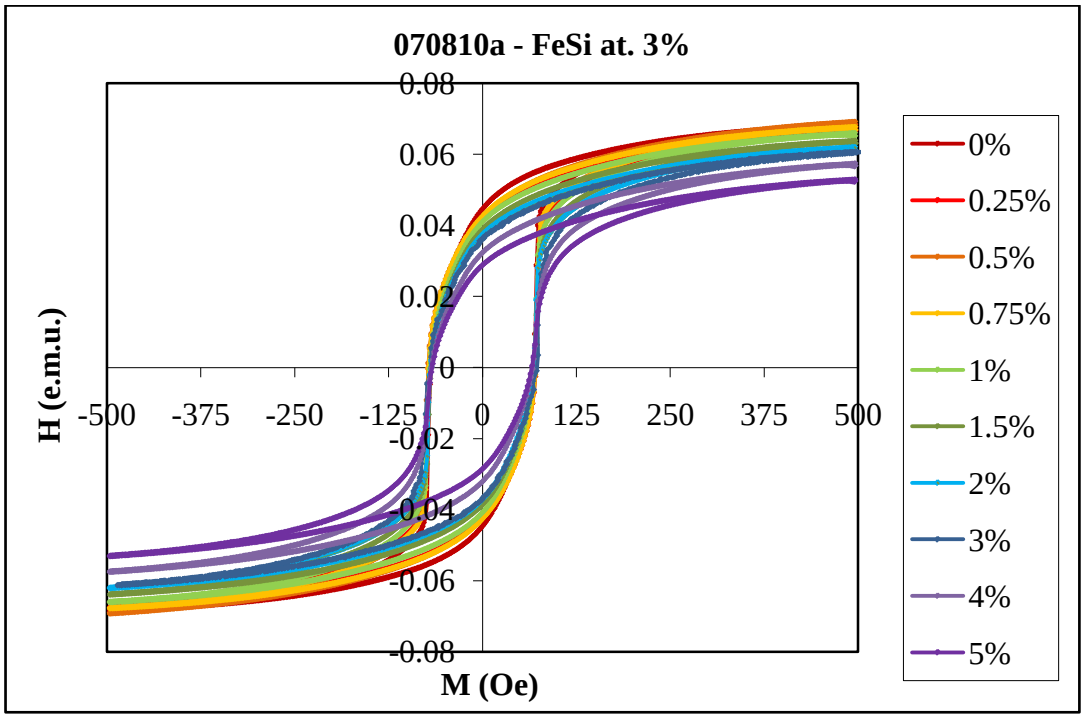

Figure 8.24: VSM Hysteresis Curves – 070819 Sample

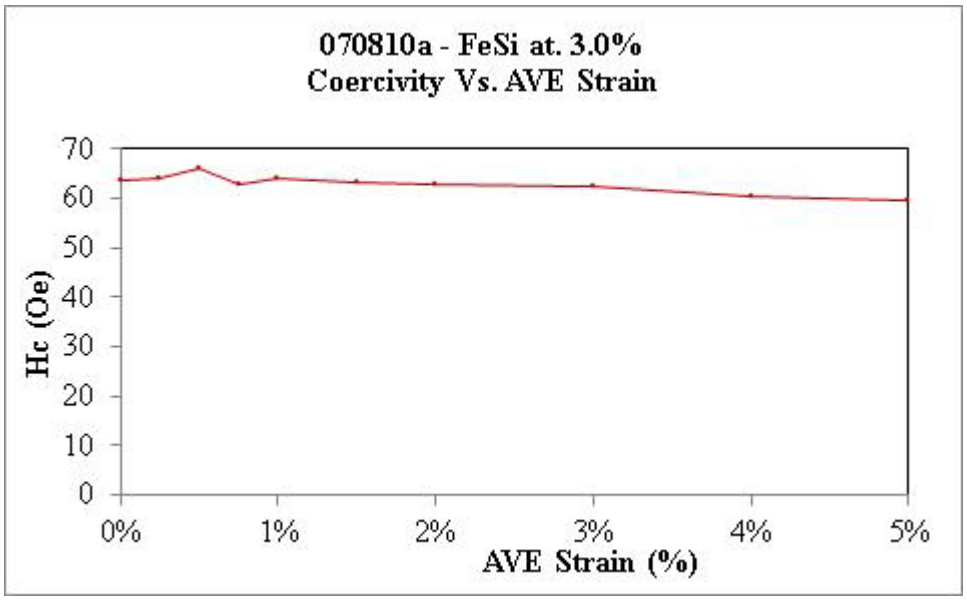

Figure 8.25: Coercivity Vs. AVE Strain – 070810 Sample

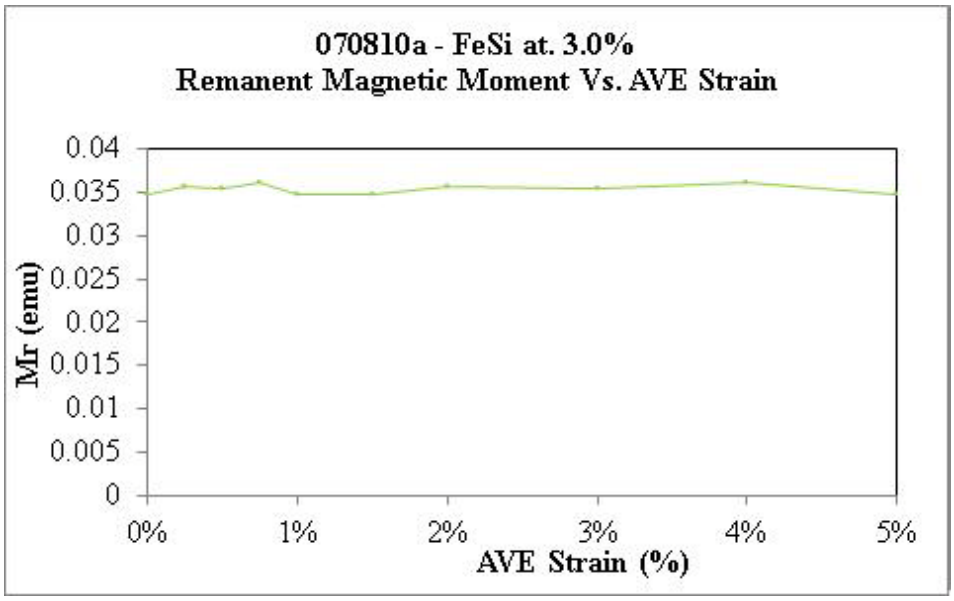

Figure 8.26: Remanent Magnetic Moment Vs. AVE Strain – 070810 Sample

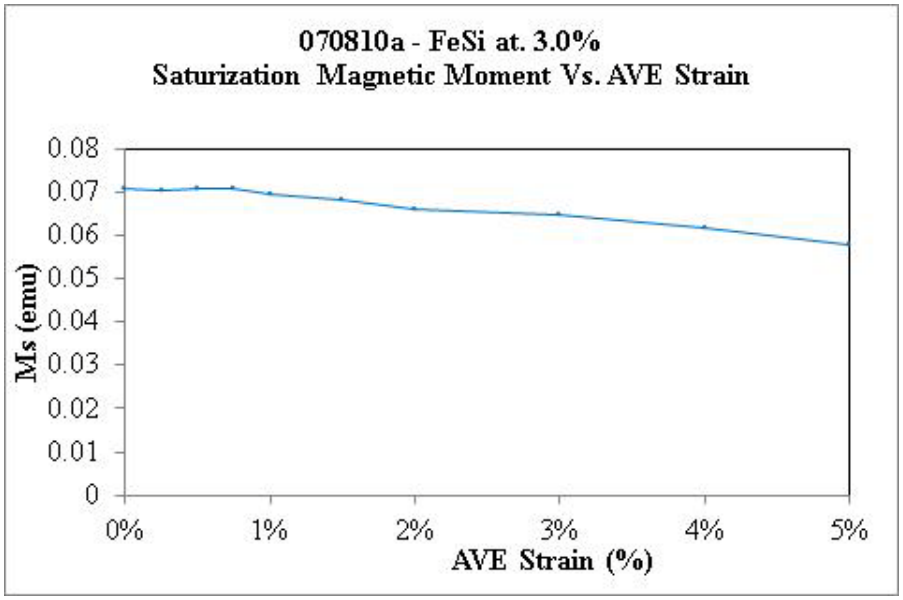

Figure 8.27: Saturation Magnetic Moment Vs. AVE Strain – 070810 Sample

Detached Material

After submitting the samples to lateral strain, an attempt was made to determine how much material had come detached from the surface of the Nitinol substrates. To do this, a piece of ordinary scotch tape was placed over the film surface and gentle pressure was applied, then the tape was peeled from the sample and attached to a blank glass disk for measurement in the VSM. The magnetic characteristics of the material remaining on the Nitinol substrate after the loose film had been removed was also measured via VSM.

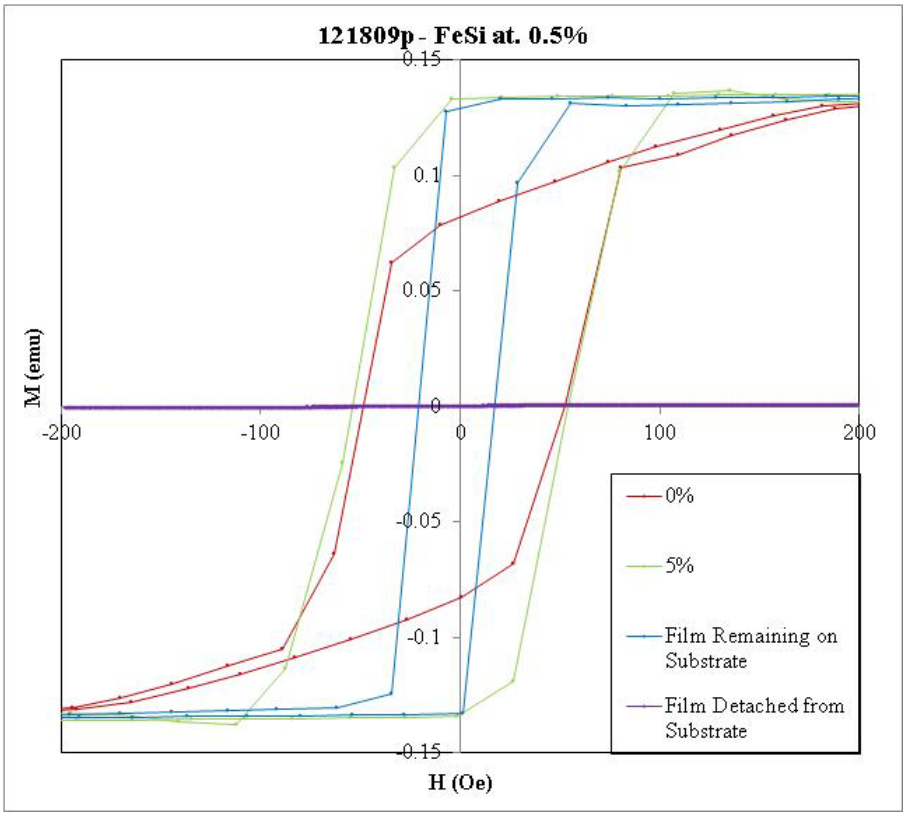

Figure 8.28: Detached Film – 121809p Sample

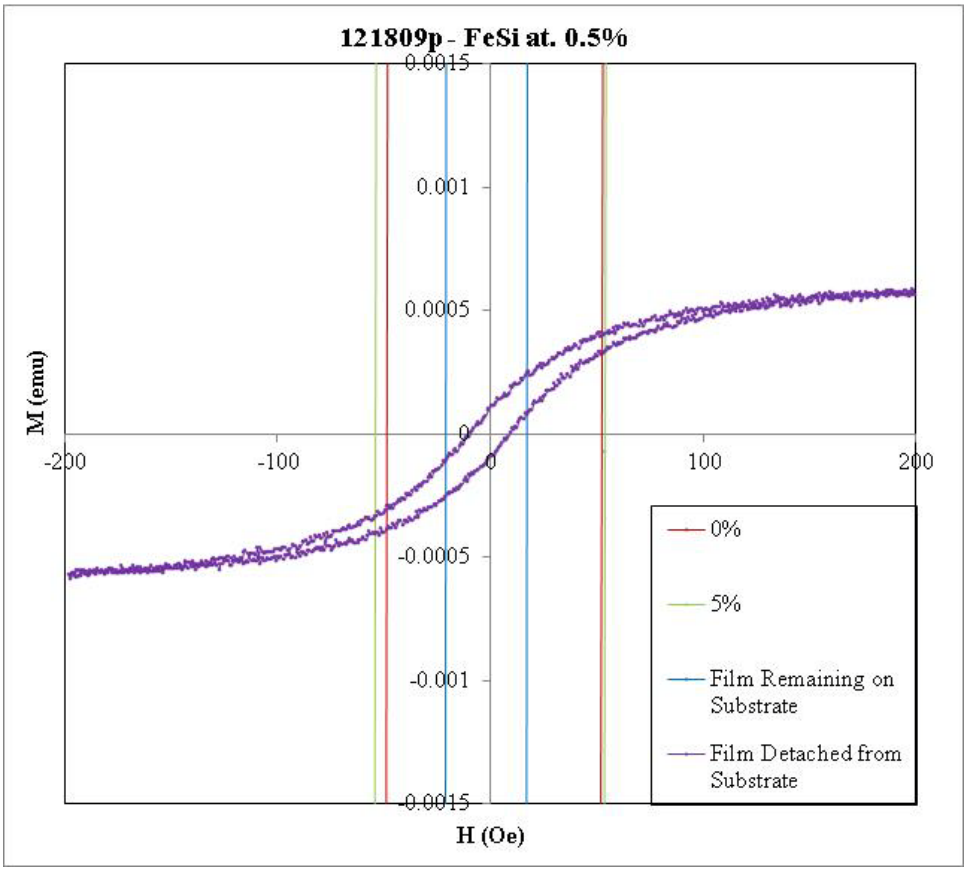

Figure 8.29: Detached Film – 121809 Sample – Zoomed

Almost no material came off the Nitinol substrate, which explains why the size of the hysteresis curve and the saturation magnetic moment is so much smaller than the values for the 0%, the 5% and the film remaining on the substrate.

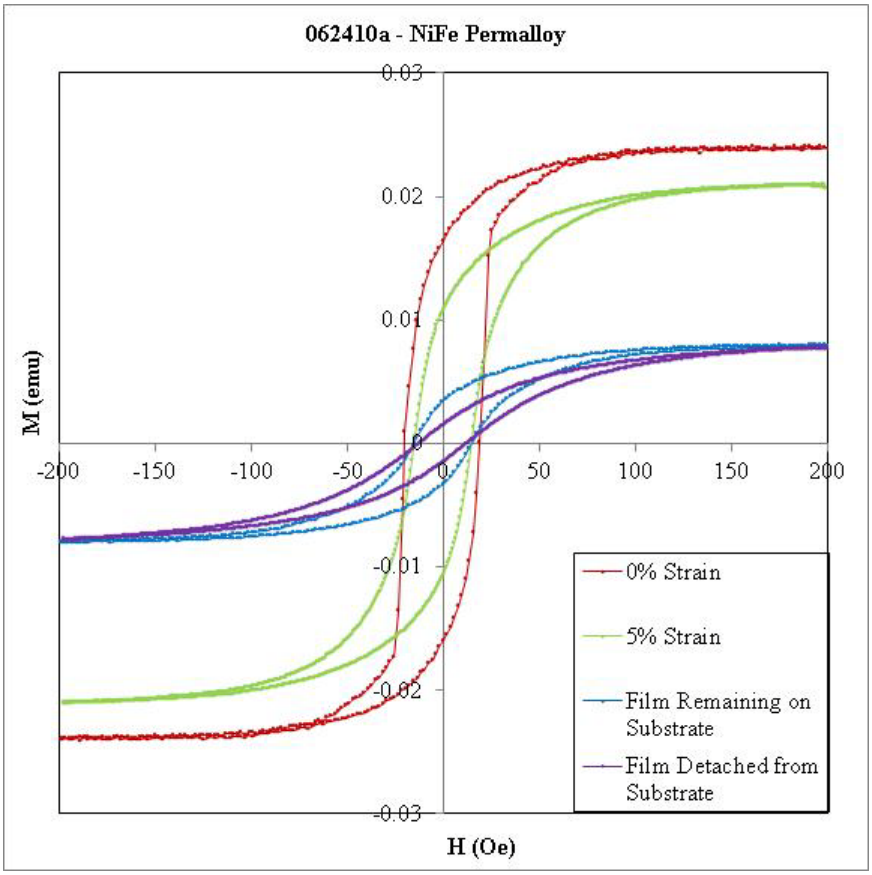

Figure 8.30: Detached Film – 062410 Sample

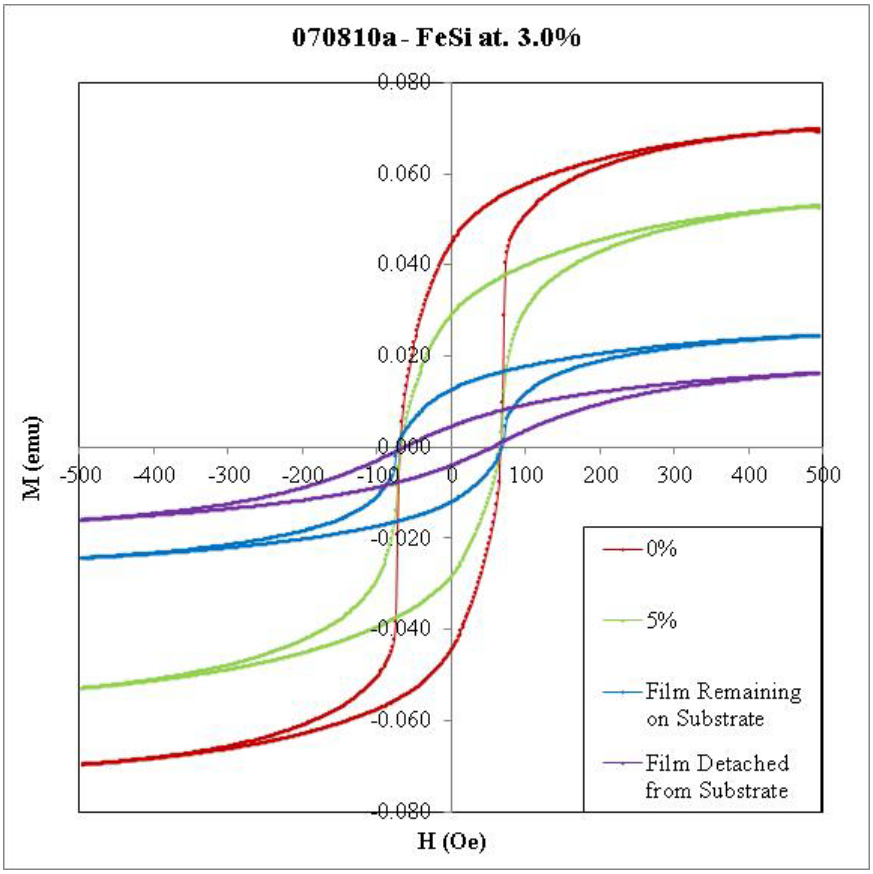

Figure 8.31: Detached Material – 070810 Sample

CHAPTER IX: CONCLUSIONS

Dual Ion Beam Sputtered films of FeSi-0.5% strongly adhere to Nitinol sheet metal. Upon excessive straining of the Nitinol, the thin magnetic film on its surface does not detach from the substrate. This is believed to be the first experiment observing films strained on Nitinol. Since the amount of film that detached from the surfaces of the magnetron sputtered 062410 and 070810 samples was much greater than the amount of film that detached from the surface of the DIBS samples (both the bent 121007 sample and the laterally strained 121809 sample), it seems fairly obvious that the adhesion of films grown via magnetron sputtering onto Nitinol substrates is much weaker than that of DIBS films. Because Nitinol is a temperature sensitive material, it is possible that the higher temperatures in the vacuum chamber during magnetron sputtering and exposure of the substrate to the plasma caused the Nitinol substrate to take on slightly different atomic spacing within its lattice. It is very possible that upon cooling the Nitinol contracted at a different rate and a different amount than the film on its surface, which introduced a small amount of compressive stress into the film before any measurements were made.

The 121809 sample exhibited only blisters in the film with almost no film loss, and the bent sample from 2007 did not lose any film after stressing. It is well known that the DIBS deposition technique usually results in strong adhesion of thin films. In addition to the influence of the deposition method however, it is possible that the FeSi-

0.5% simply adheres better to Nitinol sheet metal than permalloy or FeSi films of higher silicon content. Some may posit that higher silicon content creates a more brittle film, which is supported by the face that, in these experiments, the bent sample from 2007 (with no film loss) has lower silicon content than the 070810 magnetron sputtered sample. Although the brittleness of the film may indeed play a part in its ability to adhere to the surface of the substrates, the deposition technique appears to play a more dominant role.

Applying up to 4% strain to the thin films by bending the Nitinol substrates over a cylinder does not result in the detachment of the thin ferromagnetic films from the substrate. No evidence of inhomogeneous straining of those samples was observed. This effect is currently not understood but is significant. Some research suggests that even when bending Nitinol, the strain will not be homogeneous in the sheet metal. The transformation to the martensitic phase will start initially near the surface of the sheet metal while the middle of the sheet metal remains in the Austenitic phase [27]. The results of bending experiments suggest that, when bent, the strain in Nitnol sheet metal may be much more homogeneous than that of axially strained Nitinol. The stress-strain relation of Nitinol sheet metal during bending is currently not well understood.

Finally, magneto-plastic deformation can be studied using ferromagnetic thin film plated nitinol sheet metal. The bent sample from 2007 was measured both parallel and perpendicular to the stressing axis, and exhibited shearing in its magnetic hysteresis curve in one direction, and dual coercivity (“two-step”) in the perpendicular direction. The 121809 DIB-Sputtered sample exhibited the two-step phenomena, and the 062410 and 070810 samples both exhibited shearing in their magnetic hysteresis curves. Currently

the observed magneto-plastic effects are not completely understood. Although for some materials a combination of higher defect density and magnetostriction/residual strain can explain the observed magneto-plastic effects, [6] induced crystal anisotropy originating from plastic deformation may also contribute to the observed effect. A systematic investigation of different films with different film thickness and silicon concentration is desirable. Because of the dimensional requirements of the Instron 5566 and VSM equipment, these laterally strained samples could only be measured in one direction.

Further research should include a method of measuring the magnetic characteristics of laterally strained samples in directions both parallel and perpendicular to the strain direction. This will likely involve developing a modified sample holder (much as I did during this project) that allows the sample to be measured in different orientations. This kind of measurement (both parallel and perpendicular to the strain axis) may be possible in the new Quantum Design VSM apparatus, as this system has a superconducting magnet that is capable of accepting long samples. In addition, Kerr microscopy studies of strained samples could provide better insight in the distribution of the magneto-plastic deformation across the film's surface.

APPENDIX A: CALCULATING FILM THICKNESS

By: Kyle Smith, Texas State University, 2007

Determining Surface Area of a Sample

In taking measurements, your samples will not be perfectly square. Since we cannot assume any side to be parallel with such small samples, we must use the general quadrilateral formula to find the area.

Using the General Equation for a Quadrilateral:

$$\text{Area} = \frac{1}{2} pq \sin\theta = \frac{1}{4}\sqrt{4p^2q^2 - (b^2 + d^2 - a^2 - c^2)^2}$$

Where a, b, c, and d are all different side lengths and p and q are each the diagonals on the quadrilateral (The measure of these variables can all be taken by micrometer). The angle θ is the angle at the intersect of p and q. See Diagram below.

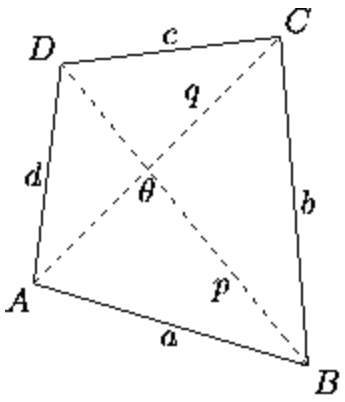

Thickness of a Sample:

In the need to find the thickness of your given sample, utilize the newly found surface area in the calculations. Also consider the Magnetization Saturation denoted as M_s:

$$M_s = \frac{m}{V}$$

Where m is the magnetic moment of the sample and V is the volume of the sample. The magnetic moment can be determined by saturation on the VSM. The M_s is a constant dependent upon the material being measured (in the case of iron, the M_s is 1751 emu/cm^3). The Volume is the product of the length, width, and thickness, which we will denote as thickness t:

$$M_s = \frac{m}{A \cdot t}$$

Where A is the Surface Area of the Sample, we solve for thickness t:

$$t = \frac{m}{A \cdot M_s}$$

APPENDIX B: CYLINDRICAL STRAINING

By: Kyle Smith, Texas State University, 2007

Method to Straining Over a Cylinder

To induce tensile strain to a given rectangular sample, we must first understand the definition of tensile strain. For general axial strain, we can say:

$$\varepsilon = \frac{\Delta \ell}{\ell_o} = \frac{\ell_f - \ell_o}{\ell_o}$$

Where ε is the strain, ℓ_o is the initial length of the sample and $\Delta\ell$ is the difference in final length ℓ_f and initial length ℓ_o. This method of strain can be translated to that of bending over a cylinder. Given a cylinder with radius R and a sample of thickness t, we can make a relation that a certain value for strain is related to the radius. Using a micrometer, we can determine the thickness of our sample and the radius of the cylinder. The strain on the material is induced when the sample is flush against the curvature of the cylinder. In order to use the axial strain equation for this setup, we must first make a few assumptions:

-Firstly, there is no stress in the middle of the sample (Denoted with hash marks). We therefore claim that there is no change in length at this point.

-Secondly, tensile strain occurs on the outer portion of the sample (the inside being compressive).

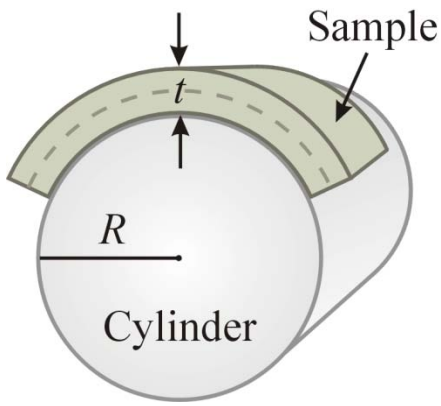

With the use of our assumptions, we can say the following expressions:

$$\ell_o = c(R + \frac{t}{2}) \qquad \ell_f = c(R + t)$$

Where c is the ratio of the sample length and full circumference. Using these expressions, we can say:

$$\varepsilon = \frac{\Delta\ell}{\ell_o} = \frac{\ell_f - \ell_o}{\ell_o} = \frac{c(R+t) - c(R+\frac{t}{2})}{c(R+\frac{t}{2})} = \frac{(R+t) - (R+\frac{t}{2})}{(R+\frac{t}{2})}$$

When we insert our expressions, we see that our ratio c cancels out. Then, through a bit of algebra, we can see an expression for strain.

$$\varepsilon = \frac{t - \frac{t}{2}}{(R+\frac{t}{2})} = \frac{\frac{t}{2}}{(R+\frac{t}{2})} = \frac{t}{(2R+t)}$$

Yielding:

$$\varepsilon = \frac{t}{(2R+t)} = \frac{t}{(D+t)}$$

Where D is the diameter of the cylinder

It is important to note that it is possible that the equilibrium point could not be in the middle but rather towards either side. This would affect the equation for its original length to be the sum of the radius and some distance within the thickness of the material:

$$\ell_o = c(R + at)$$

Where a is a constant to denote the location of the equilibrium point within the sample. The more general equation for strain over a cylinder given a certain equilibrium point:

$$\varepsilon = \frac{t(1-a)}{R+at}$$

REFERENCES

[1] Amanda Gregory, Wilhelmus J. Geerts, Anup Bandyopadhyay. "Magneto-Plastic Properties of Ion Beam Sputtered Thin Films on Nitinol Sheet Metal." Oral Presentation at the Texas Section APS Fall meeting, University of Texas-San Antonio. October 2010.

[2] Amanda Gregory, Martin Sablik, Wilhelmus Geerts, Kyle Smith, Anup Bandyopadhyay, Fernando Landgraf, Marcos de Campos. "Magnetoplastic Properties of Thick Films on Nitinol Substrate." Oral Presentation at the Texas Section APS Fall meeting, Texas State University-San Marcos. October 2009.

[3] Amanda Gregory, Kyle Smith, Clayton Moore, Daniel Palmer, Anup Bandyopadhyay, Wilhelmus Geerts, Martin Sablik. "The Effect of Plastic Deformation on the Magnetic Properties of Thin Iron and Permalloy Films." Poster Presentation at the Four Corners and Texas Section APS Fall meeting, University of Texas-El Paso. October 2008.

[4] Amanda Gregory, Kyle Smith, Clayton Moore, Daniel Palmer, Anup Bandyopadhyay, Wilhelmus Geerts, Martin Sablik. "The Effect of Plastic Deformation on the Magnetic Properties of Thin Iron and Permalloy Films." Poster Presentation at the Texas State Undergraduate Research Conference and Honors' Thesis Forum. November 2007.

[5] Anup Bandyopadhyay, Wilhelmus Geerts, Kyle Smith, Amanda Gregory, Clayton Moore, Daniel Palmer, Jitendra Tate, Martin Sablik. "Plastic Deformation of Thin Ferromagnetic Films on Nitinol Sheet Metal." Poster presentation at the International MMM Conference in Austin, TX. November 2008.

[6] Martin J. Sablik, Wilhelmus J. Geerts, Kyle Smith, Amanda Gregory, Clayton Moore, Daniel Palmer, Anup Bandyopadhyay, Fernando J. G. Landgraf, Marcos F. de Campos. "Modeling of Plastic Deformation Effects in Ferromagnetic Thin Films." Publication in IEEE Trans. On Magn. 46 (2010) page 491. 2010.

[7] Luca Callegaro, Ezio Puppin, IEEE Trans. on Magn. 33 (1997) 1007-1011.

[8] Claude Garrett, Patrick Holland, Wilhelmus J. Geerts, Dustin Ragan, Archana Dubey, Steve Rios, Anup K. Bandyopadhyay, J. Appl. Phys 93 (2003) 8624-8627.

[9] O. Kraft, L.B. Freund, R. Phillips, E. Arzt, MRS bulletin 27 (2002) 30-37.

[10] Noboru Ito, J. Appl. Phys. 42 (1972) 3170-3174.

[11] Noboru Ito, Jpn. J. Appl. Phys. 10 (1971) 1483-1484.

[12] M. Lupulescu, B. F. Rothenstein, Thin Solid Films 7 (1971) R27-R29.

[13] O. Shinoura, T. Koyanagi, Electrochimica Acta. 42 (1997) 3361-3366.

[14] Images Scientific Instruments website: http://www.imagesco.com/articles/nitinol/03.html

[15] S. Daly, G. Ravichandran, K. Bhattacharya. Acta Materialia 55 (2007) 3593-3600.

[16] Varian Associates, Inc. Basic Vacuum Practice, 3rd edition. Lexington MA.

[17] Televac. Televac CC-10 Wide Range Vacuum Gage. http://www.televac.com/vac_gauges/PDFs/CC-10.pdf

[18] Sebastian Pchon, David Pearson. "Ion Beam Deposition." Oxford Instruments Plasma Technology Ltd. (2010) 1-9.

[19] B. Buchholtz. "Physics of Ion Beam Sources."

[20] Albert W. Hull and Irving Langmuir, "Control of an Arc Discharge by Means of a Grid." Research Laboratory, General Electric Co. 1928.

[21] J.W. Luginsland, Y.Y. Lau, and R.M. Gilgenbach. "Two Dimensional Child-Langmuir Law." Phys. Rev. Letters 1996, 77, 22, 4668-4670.

[22] A. K. Bandyopadhyay et al. Journal of Alloys and Compunds 2004, 369, 217-221.

[23] "What is Sputtering?" AJA International, Inc. http://www.ajaint/whatis.htm

[24] "Magnetron Sputtering Cathodes." EngineerLive. http://www.engineerlive.com/Design-Engineer/Materials_Processes/Magnetron_sputtering_cathodes/18921/

[25] "Residual Gas Analyzer." SiliconFarEast.com (2005) http://www.siliconfareast.com/rga.htm

[26] John Andrew Shaw. "Material Instabilities in a Nickel-Titanium Shape Memory Alloy." Dissertation. (1997).

[27] Apurva Mehta, Xiao-Yan Gong, Valentina Imbeni, Alan R. Pelton, and Robert O. Ritchie, "Understanding the Deformation and Fracture of Nitinol Endovascular Stents Using In Situ Synchrotron X-Ray Microdiffraction." Adv. Mater. 2007, 19, 1183–1186.

[28] Martin J. Sablik and David C. Jiles. "Coupled Magnetoelastic Theory of Magnetic and Magnetostrictive Hysteresis." IEEE Trans. On Magn., (1993), 29, 2113-2123.

[29] Abdelaziz Ladjimi and Mohammed El Rachid Mekideche. "Modeling of Magnetic Hysteresis and Calculation of Field in Magnetic Medium." International Journal of Sciences and Techniques of Automatic Control and Computer Engineering. 580-589.

[30] D.C. Jiles and D.L. Atherton. "Ferromagnetic Hysteresis." IEEE Trans. On Magn. Mag-19, 5 (1983) 2183-2185.

[31] David J. Griffiths. "Introduction to Electrodynamics." 3rd ed. Prentice-Hall, Inc. (1999).

ADDITIONAL READING AND HELPFUL WEBSITES

A selection of useful websites and literature have been included for the interested reader. Although these sources were not specifically cited in this thesis, the author found them useful tools for understanding the wide variety of concepts related to this material.

- "Understanding Virtual Leaks" from A Journal of Practical and Useful Vacuum Technology – Danielson, Phil – www.vacuumlab.com

- "Nitinol: shape-memory and super-elastic materials in surgery" – A. Szold – Surg Endose (2006) 20:1493-1496.

- http://www.nitinol.com/nitinol-university/nitinol-facts/

- http://jmmedical.com/index.php?p=nitinol&id=65

- http://www.lakeshore.com/pdf_files/systems/vsm/mag%20media%20app%20note.pdf

- http://www.darkfieldlightmicroscopes.com/how-does-brightfield-darkfield-light-microscopy-works.html
- http://www.darkfieldlightmicroscopes.com/how-does-brightfield-darkfield-light-microscopy-works.html
- http://www.acasystems.com/en/web-thumb-activex/faq-image-format.htm
- http://www.irm.umn.edu/hg2m/hg2m_a/hg2m_a.html
- http://hyperphysics.phy-astr.gsu.edu/hbase/solids/hyst.html
- http://www.doitpoms.ac.uk/tlplib/superelasticity/superelasticity1.php
- http://www.txstate.edu/physics/research/facilities/magnetic.html
- http://hyperphysics.phy-astr.gsu.edu/hbase/solids/hyst.html
- http://www.imagesco.com/articles/nitinol/03.html
- http://prola.aps.org/abstract/PR/v21/i4/p402_1
- http://www.instron.us/wa/applications/test_types/tension/how_to_test.aspx
- http://www.iso.org/iso/iso_catalogue/catalogue_tc/catalogue_detail.htm?csnumber=4594
- http://www.instron.us/wa/solutions/Tensile_Properties_Films_Sheets.aspx
- http://www.instron.us/wa/acc_catalog/prod_list.aspx?cid=452&cname=Non-contacting%20Video%20Extensometers
- https://www.instron.us/wa/
- http://www.astm.org/Standards/F2516.htm
- http://physics.gac.edu/~huber/misc/aiprefs.htm
- http://www.lib.monash.edu.au/tutorials/citing/aip.html

VITA

Amanda Faith Gregory was born in Weslaco, Texas on June 26, 1981, daughter of Kenneth John Gregory and Brenda Ann Gregory. After completing her work at the Science Academy of South Texas in Mercedes, Texas, and the University Preparatory School in Harlingen, Texas, in December 1997, she entered the University of Texas Pan American in Edinburg, Texas in the spring of 1998. After relocating to Victoria, Texas, she attended Victoria College in 2000. She then relocated to Austin, Texas, and attended Austin Community College from 2001 until 2005. In August 2005, she received an Associate's Degree in Mathematics from Austin Community College. In August 2005, she entered Texas State University-San Marcos, and she received her Bachelor of Science in Physics from Texas State in August 2008. In August 2008, she entered the Graduate College of Texas State.

Permanent email address: Amanda.F.Gregory.0@gmail.com

This thesis was typed by Amanda F. Gregory